

# **Performance scaling of laser amplifiers via coherent combination of ultrashort pulses**

Dissertation  
zur Erlangung des akademischen Grades  
doctor rerum naturalium (Dr. rer. nat.)

vorgelegt dem Rat der Physikalisch-Astronomischen Fakultät  
der Friedrich-Schiller-Universität Jena  
von Dipl.-Phys. Arno Klenke  
geboren am 24.09.1984 in Paderborn, Deutschland

## Gutachter

1. Prof. Dr. Andreas Tünnermann
2. Prof. Dr. Malte Kaluza
3. Prof. Dr. Thomas Südmeyer

Tag der Disputation: 28.1.2016

# Contents

<b>1. Introduction</b>	<b>1</b>
<b>2. Fundamentals</b>	<b>4</b>
2.1. Temporal and spatial definition of ultrashort laser pulses . . . . .	4
2.2. Propagation of ultrashort pulses . . . . .	6
2.2.1. Chromatic dispersion . . . . .	6
2.2.2. Nonlinear effects . . . . .	7
2.2.3. Pulse-propagation equation . . . . .	9
2.2.4. Propagation of strongly stretched pulses . . . . .	10
2.3. Architectures for the amplification of ultrashort pulses to high average powers . . . . .	11
2.3.1. Ytterbium-doped fiber amplifiers . . . . .	12
2.4. Limitations of the peak power and pulse energy . . . . .	15
2.4.1. Extractable energy . . . . .	16
2.4.2. Self-focusing . . . . .	17
2.4.3. B-integral . . . . .	17
2.4.4. Surface damage . . . . .	18
2.4.5. Comparison of the different limitations . . . . .	19
2.5. Limitations of the average power . . . . .	20
2.6. Performance development of femtosecond fiber laser systems . . . . .	21
<b>3. Combination of ultrashort pulses</b>	<b>24</b>
3.1. Basic concept . . . . .	24
3.1.1. Phase-sensitive and non-phase-sensitive combination . . . . .	24
3.1.2. Spectral combination and non-spectral (or coherent) combination . . . . .	26
3.1.3. Spatial and temporal combination . . . . .	29
3.2. Splitting and combination elements . . . . .	31
3.2.1. Tiled-aperture and filled-aperture approaches . . . . .	31
3.2.2. Polarization and non-polarization combination . . . . .	33

3.2.3.	1:2 splitting elements . . . . .	34
3.2.4.	1:N splitting elements . . . . .	36
<b>4.</b>	<b>Efficiency of the coherent combination process</b>	<b>39</b>
4.1.	Definition of the combination efficiency . . . . .	39
4.2.	Impact of temporal mismatches of the pulses . . . . .	41
4.3.	Impact of beam profile mismatches . . . . .	47
4.4.	Impact of the failure of individual channels . . . . .	48
4.5.	Improvements of the pulse and beam quality with coherent combination .	49
4.6.	Coherent combination of spectrally broadened pulses . . . . .	49
<b>5.</b>	<b>Path-length-stabilization techniques for coherent combination</b>	<b>53</b>
5.1.	Introduction . . . . .	53
5.1.1.	Passive and active stabilization techniques . . . . .	53
5.2.	Active stabilization techniques . . . . .	55
5.2.1.	Hänsch-Couillaud stabilization for polarization combination . . .	55
5.2.2.	LOCSET . . . . .	59
<b>6.</b>	<b>Experimental demonstration of coherent combination</b>	<b>61</b>
6.1.	State of the art . . . . .	61
6.2.	Setup of the front-end system . . . . .	62
6.3.	Combination of high-performance fiber amplifiers . . . . .	64
6.3.1.	High-average-power system . . . . .	65
6.3.2.	High-peak-power system . . . . .	68
6.3.3.	Applications . . . . .	72
6.4.	Combination of bulk amplifiers . . . . .	73
6.5.	Combination of solid-core fibers for nonlinear pulse compression . . . . .	76
6.5.1.	Setup and results . . . . .	76
6.6.	System integration of multiple channels . . . . .	78
6.6.1.	1:N segmented-mirror splitter . . . . .	78
6.6.2.	Multicore fiber amplifiers . . . . .	80
6.6.3.	Setup and experimental results . . . . .	82
<b>7.</b>	<b>Conclusion &amp; Outlook</b>	<b>88</b>
	<b>Bibliography</b>	<b>92</b>

<b>A. Calculation of the maximum stretched pulse duration</b>	<b>104</b>
<b>B. Calculation of the combination efficiency for the multicore fiber</b>	<b>106</b>
<b>Zusammenfassung (Summary)</b>	<b>107</b>
<b>Danksagung (Acknowledgement)</b>	<b>108</b>
<b>Ehrenwörtliche Erklärung</b>	<b>109</b>

# 1. Introduction

Laser systems emitting ultrashort pulses have opened up a variety of new applications during the last decades. These range from industrial applications such as material processing [1], medical applications [2] to fundamental research. Over the years, these applications have become more demanding on the performance of the laser systems, requiring better parameters in terms of the energy of the emitted pulses, their peak power and duration. At the same time, high repetition rates in the kHz-level or higher are often desired or even a necessity to make these processes feasible for real-world applications. These high repetition rates result in an increase of the average output power to the Kilo-watt- or even Mega-watt-level. Today, there is not a single laser architecture that can deliver all of these parameters simultaneously. On the one hand, laser systems with peak powers higher than 1 PW [3] are available today. However, they emit pulses with a repetition rate of a few Hz at most, thus resulting in average powers of just a few Watts. Increasing the average power to considerably higher values is challenging due to the onset of thermal effects that detrimentally impact the beam quality. On the other hand, high average power thin-disk, slab and fiber lasers provide Kilo-watt-level average powers [4–6], but the peak powers are many orders of magnitudes lower in the GW-range. Additional effects, e.g. mode-instabilities for fibers [7–9], can also limit the further increase of the average power for these architectures. Even though the development of all these laser architectures still continues and it will certainly improve their performance, it is not expected that a single system will provide all of the desired parameters for demanding applications in the foreseeable future. One example of such an application is the conversion of light from the infrared wavelength region, where most of these laser systems operate, to XUV wavelengths. This process is called high-harmonic generation (HHG) [10,11] and requires a peak intensity higher than  $10^{14} \frac{\text{W}}{\text{cm}^2}$  to generate coherent XUV radiation. Even for small focused beam sizes of 100  $\mu\text{m}$  diameter, this still demands pulses with multiple Gigawatts of peak power and at high repetition rates, this also results in high average powers. Moreover, applications such as laser-particle-acceleration [12] are even more demanding, requiring peak powers of at least several

Terawatts. To replace conventional accelerators with RF-technology in the future [13] multi-kHz repetition rates are desired, resulting in even higher average powers.

Hence, new power scaling concepts have to be developed. The concept investigated in this thesis is to combine multiple ultrashort laser pulses, e.g. pulses emitted from multiple laser amplifiers, for performance improvements. Depending on the combination technique used, improvements of the pulse energy and/or average power are possible and existing physical limitations can be overcome. Apart from amplifiers, pulse combination can also be applied to other systems that show similar limitations such as, for example nonlinear pulse compression stages. Even though all the previously mentioned laser architectures can be in principle used for pulse combination, this thesis will mainly focus on fiber based amplifiers. The reason for this is their simple single-pass setup and reproducible beam profile, which is, besides a reproducible temporal pulse profile, a requirement for an efficient combination. Fiber laser systems emitting ultrashort pulses have seen a rapid development over the the recent decades with an increase of their performance values by many orders of magnitude, but in the last years the progress has leveled off due to a variety of physical effects. At the beginning of these thesis, if systems emitting a peak power of at least 1 GW are considered, the highest achieved average power and peak power were 50 W [14] and 3.8 GW [15], respectively. By employing multiple coherently combined parallel amplifiers, laser systems could be realized that far exceed these performance values.

The thesis is structured in the following way: in chapter 2 the basic mathematical description of ultrashort pulses will be given, which is necessary to understand the pulse combination process later on. Additionally, some high average power laser architectures will be discussed, with a focus on fiber based sources. In the following chapter the wide field of combination mechanisms for ultrashort pulses will be explored and categorized. Different elements for beam and pulse splitting and combination will be presented. This is followed by the theoretical analysis of the combination efficiency when doing coherent combination and the impact of effects such as path-length- and B-integral differences in the channels. Besides the coherent combination of pulses originating from amplifiers, the use of this technique for the nonlinear compression process will also be investigated. The theoretical considerations are finalized in chapter 5 with the discussion of different active path-length-stabilization mechanisms. In chapter 6 the previously described techniques will be put into action in different experiments. This includes a state-of-the-art fiber CPA system with a main amplification stage comprising four parallel amplifiers in two different configurations, providing performance values not achieved so far with single

amplifier fiber based systems. Additionally, the combination of two bulk amplifiers will also be shown, broadening the scope from fiber amplifiers to a different laser architecture. A first proof-of-principle experiment covers the use of coherent combination for nonlinear compression. Finally, the integration of multiple amplifier channels into a single fiber in combination with a compact 1:N splitter design will also be demonstrated, paving the way for laser systems with a large number of parallel channels in the future. In chapter 7, the results of this thesis will be summarized and an outlook on further possibilities for building the laser systems needed to fulfill the requirements of the most demanding applications will be given.



## 2. Fundamentals

In order to understand the combination mechanism of ultrashort pulses from separate laser beams, it is necessary to introduce a mathematical description of these pulses. This includes the temporal dependence of the corresponding electrical fields as well as the spatial profiles of the beams. In this chapter, the mathematical description will be given, followed by a discussion of processes that impact the temporal pulse form during amplification, which can affect the combination process as described in chapter 4. Different amplifier architectures for high-average-power operation will be introduced, with a focus on fiber-based systems. Finally, limitations of fiber amplifiers with regard to pulse energy, peak power and average power will be analyzed to motivate the need for coherent combination of ultrashort pulses to further improve the performance of fiber laser systems.

### 2.1. Temporal and spatial definition of ultrashort laser pulses

The electric field of an ultrashort pulse propagating in the  $z$ -direction can be described by the following formula:

$$\vec{E}(x, y, z, t) = \vec{e}_t(t)T(x, y)E(z, t) \quad (2.1)$$

with the vector  $\vec{e}_t(t)$  being the direction of the polarization of the electric field,  $T(x, y)$  is the spatial beam profile and  $E(z, t)$  is the temporal pulse profile. It should be noted that two assumptions have been made here: at every instant the electric field only has a transversal component and the beam profile does not change over the course of the pulse. Both assumptions are fulfilled by ultrashort pulses in free space (where the combination process will take place) emitted by laser amplifiers. In many cases, it is beneficial to

consider the temporal pulse form in frequency domain because it is more convenient to describe effects such as dispersion in this domain. Then, equation 2.1 can be written as:

$$\vec{E}(x, y, z, t) = \vec{e}_t(t)T(x, y) \int_{-\infty}^{\infty} d\omega \tilde{E}_0(\omega) \exp [i(\omega t - k(\omega)z)] \quad (2.2)$$

with the spectral electric field  $\tilde{E}_0(\omega)$  and the wave-number  $k(\omega) = \omega \frac{n(\omega)}{c}$  [16]. In the next step, the fast oscillation of the carrier frequency  $\omega_0$  is taken out of the integral. It should be noted that, so far, no approximation has been done, so the result is valid even for pulses consisting of just a few optical cycles:

$$\vec{E}(x, y, z, t) = \vec{e}_t(t)T(x, y)e^{i\omega_0 t} \int_{-\infty}^{\infty} d\omega \tilde{E}_0(\omega) \exp [i((\omega - \omega_0)t - k(\omega)z)] \quad (2.3)$$

To simplify the equation even further, a Taylor expansion of the wave-number can be carried out, introducing the expansion coefficients  $\beta_n$  [16]. This is valid as long as the condition  $\Delta\omega \ll \omega_0$  is fulfilled, meaning that the pulse frequency bandwidth  $\Delta\omega$  should be narrow compared to the carrier frequency :

$$\beta_n = \left( \frac{\partial^n k(\omega)}{\partial \omega^n} \right)_{\omega=\omega_0} \quad (2.4)$$

$$k(\omega) = \beta_0 + \beta_1(\omega - \omega_0) + \frac{1}{2}\beta_2(\omega - \omega_0)^2 + \frac{1}{6}\beta_3(\omega - \omega_0)^3 + O(\omega^4) \quad (2.5)$$

Due to the above mentioned condition on the spectral bandwidth, this approximation is limited to pulse durations longer than 100 fs at 1  $\mu\text{m}$  wavelength [16]. This approximation is known as slowly-varying amplitude approximation. Using the coefficients  $\beta_n$ , the phase velocity  $v_{\text{ph}}$  (which describes the propagation speed of the carrier wave) and the group velocity  $v_{\text{g}}$  (which describes the propagation speed of the temporal envelope of the pulse) can be defined as:

$$v_{\text{ph}} = \frac{\omega_0}{\beta_0} = \frac{c}{n(\omega_0)} \quad (2.6)$$

$$v_{\text{g}}(\omega) = \frac{1}{\beta_1} = \frac{c}{n(\omega) + \omega \left( \frac{dn(\omega)}{d\omega} \right)} \quad (2.7)$$

A mismatch between both terms results in a time dependency of the carrier-envelope (CE) phase. The CE-phase is especially relevant for few-cycle pulses and can have a significant impact on certain applications [17].

The definition of the spatial beam profile depends on the environment the light is propagating through. During propagation in waveguide structures, the beam profile can be calculated as a superposition of multiple modes and the structure of these modes is strongly dependent on the waveguide geometry [18, 19]. For free-space propagation, on the other hand, the spatial intensity and phase profile can be arbitrarily chosen. However, for most applications a beam with a flat phase profile and Gaussian intensity profile is preferred. This has the benefit of a constant structure of the beam profile during propagation and that the beam can be focused to a well defined focal spot [20]. Additionally, the fundamental mode of optical fibers can be approximated by a Gaussian beam in most cases [16]. Hence, the term  $T(x, y)$  in equation 2.1 can be approximately written as:

$$T(x, y) = \exp \left[ -2 \ln(2) \left( \frac{x^2 + y^2}{w^2} \right) \right] \quad (2.8)$$

with the half-maximum beam-width being  $w$ , as long as the divergence of the beam can be neglected (which is true for large enough beam diameters and free-space propagation). In most of the calculations in this thesis a flat spatial phase profile will be assumed and deviations from this profile will be treated as detrimental effects for the pulse combination process.

## 2.2. Propagation of ultrashort pulses

### 2.2.1. Chromatic dispersion

During the propagation of a laser pulse through material its temporal and spectral properties may be modified. This is caused by effects that have an impact in the spectral domain such as dispersion and ones that are dependent on the temporal form of the pulse such as nonlinear effects. Differences in the temporal and spectral properties of pulses that are to be combined together can have a major detrimental effect on the efficiency of the combination process (see chapter 4). Hence, it is important to have a theoretical description of these effects. Chromatic dispersion is determined by the frequency dependence of the refractive index  $n(\omega)$ . When using a waveguide, it is important to take into account that the dispersion is not only caused by the material of the amplifier, but by the waveguide as well [18]. As can be derived from the definition of the wave-number  $k(\omega)$ , dispersion leads to a frequency dependence of the higher-order terms in equation 2.5. While a constant spectral phase alters the CE-phase of the pulse

and a linear spectral phase shifts the pulse envelope in time domain, these higher-order terms change the temporal intensity and phase profile of the pulse. For example, if a pulse with a bandwidth of  $\Delta\omega$  is considered, a rough estimation of the pulse duration after a propagation length  $L$  through a dispersive medium can be done by calculating the propagation time difference between the spectral components separated by  $\Delta\omega$ :

$$\Delta\tau = \frac{\partial(\beta_1 L)}{\partial\omega} \Delta\omega = \beta_2 L \Delta\omega \quad (2.9)$$

Strictly speaking, this equation is only valid if the contributions of the third- and higher-order terms of  $\beta$  can be neglected. To perform a calculation of the dispersion during amplification and propagation, the coefficients  $\beta_n$  need to be known. As previously mentioned, they comprise contributions from the material and (if existing) the waveguide. The wavelength dependence of the refractive index is well known for commonly used host materials such as YAG [21] or fused silica [22]. And even though doping the material with rare-earth ions has an impact on the refractive index (and in some cases even makes the guidance in fibers even possible [16]), its absolute impact is low enough to be neglected for the calculation of the pulse propagation. On the other hand, the waveguide dispersion is strongly dependent on the structure of the waveguide. However, for the high-power amplifiers with large core diameters considered in this work, it is in general negligible compared to the material dispersion.

Another way to apply dispersion is to use a setup comprising multiple optical diffraction gratings (or multiple passes of the pulses over one grating) that turns the angular dispersion of one grating into a temporal delay. These systems allow for dispersion coefficients many orders of magnitude above the material dispersion values and are the basis for the chirped-pulse-amplification (CPA) [23] concept, which will be described in section 2.4.

### 2.2.2. Nonlinear effects

The chromatic dispersion is a wavelength dependent linear effect that occurs independently from the temporal pulse profile, there are also nonlinear effects that exhibit such dependence. The reason for this is that the electric field of the laser pulses induces a polarization  $\vec{P}$  in the material, which has a nonlinear response to it [16]:

$$\vec{P} = \epsilon_0 \sum_i \chi^{(i)}(\vec{E})^i \quad (2.10)$$

where  $\epsilon_0$  is the vacuum permittivity and  $\chi^{(i)}$  are the  $i$ -th order susceptibility tensors. The first nonlinear contribution is the second-order term, however, it is only non-zero for media without inversion symmetry. Hence, for materials such as fused silica, the third-order term is the first one leading to non-linear effects. Due to the dependence on the electric field amplitude to the third power, these effects are strongly dependent on its strength and, therefore, on the temporal pulse form of the pulse. This leads to the definition of a second term of the refractive index called the nonlinear coefficient  $n_2$ :

$$n(\omega) = n_0(\omega) + n_2 I \quad (2.11)$$

with the optical intensity  $I$ . The value of  $n_2$  has been measured for different wavelengths in numerous experiments. For a wavelength of 1030 nm, a value of about  $2.7 \cdot 10^{-16} \frac{\text{cm}^2}{\text{W}}$  could be determined [24]. This term leads to a time-dependent phase shift called self-phase modulation (SPM). Depending on the system, SPM can have an unwanted impact on the pulse such as the amplification of temporal side pulses and the degradation of the pulse quality [25], but it can also be exploited for nonlinear pulse compression (see section 4.6). To estimate the strength of SPM during the amplification process the B-integral can be introduced:

$$B = \frac{2\pi}{\lambda_0} \int_0^L n_2 \frac{P_{\max}(z)}{A_{\text{eff}}} dz \quad (2.12)$$

with  $P_{\max}(z)$  being the peak power of the pulse depending on the position  $z$  in the fiber.  $A_{\text{eff}}$  is the effective area of the beam with the following definition using the spatial intensity profile  $T(x, y)$ :

$$A_{\text{eff}} = \frac{\left( \int_{-\infty}^{\infty} \int_{-\infty}^{\infty} dx dy T^2(x, y) \right)^2}{\int_{-\infty}^{\infty} \int_{-\infty}^{\infty} dx dy (T^2(x, y))^2} \quad (2.13)$$

Additionally, it is part of the  $\gamma$ -factor that is often introduced to calculate the B-integral:

$$\gamma = \frac{n_2 \omega_0}{c A_{\text{eff}}} \Rightarrow B = \gamma \int_0^L P_{\max}(z) dz \quad (2.14)$$

### 2.2.3. Pulse-propagation equation

In order to describe the pulse propagation, the occurring effects have to be combined into a single equation. This results in the so-called nonlinear Schrödinger equation [16]:

$$\frac{\partial A}{\partial z} + \underbrace{\beta_1 \frac{\partial A}{\partial t}}_{\text{propagation}} + \underbrace{\sum_{n=2} \frac{i^n}{n!} \beta_n \frac{\partial^n A}{\partial t^n}}_{\text{dispersion}} + \underbrace{\frac{\alpha}{2} A}_{\text{absorption, gain}} = \underbrace{i\gamma |A|^2 A}_{\text{SPM}} \quad (2.15)$$

with the slowly varying field amplitude  $A(t, z)$  normalized to the optical power. Additionally, the absorption coefficient  $\alpha$  has been added to model a simple exponential amplification model with a negative value for  $\alpha$ . Due to the nature of the equation, the use of an analytical solution is restricted to cases where either the dispersion or SPM can be neglected. Otherwise, a numerical model should be employed. The most popular one is the so-called Fourier-split-step approach [16]. In this case, the propagation is split into small steps along the active medium. For every one of those steps, the SPM phase caused by the corresponding term in equation 2.15 is calculated and applied to the amplitude function  $A(t, z)$ . Then, a Fourier transformation is executed that results in the spectral amplitude function  $\tilde{A}(\omega, z)$ . In the spectral domain, the phase caused by dispersion can easily be applied, followed by an inverse Fourier transformation back to the time domain. This Fourier-split-step approach can be implemented in a simulation software and it will be used for some of the simulations in this thesis. It should be noted that the step size for the propagation has to be chosen small enough to reduce numerical errors, but not too small to avoid an unnecessary long simulation time. Even though equation 2.15 is sufficient to describe most propagation effects in fibers, in some cases (e.g. for very short pulses), some higher-order nonlinear effects have to be added [16]:

$$\frac{\partial A}{\partial z} + \underbrace{\beta_1 \frac{\partial A}{\partial t}}_{\text{propagation}} + \underbrace{\sum_{n=2} \frac{i^n}{n!} \beta_n \frac{\partial^n A}{\partial t^n}}_{\text{dispersion}} + \underbrace{\frac{\alpha}{2} A}_{\text{absorption, gain}} = \underbrace{i\gamma |A|^2 A}_{\text{SPM}} - \underbrace{a_1 \frac{\partial}{\partial t} (|A|^2 A)}_{\text{self-steepening}} - \underbrace{a_2 A \frac{\partial |A|^2}{\partial t}}_{\text{Raman}} \quad (2.16)$$

with the parameters  $a_1 = \gamma/\omega_0$  and  $a_2 = i\gamma T_R$ , where  $T_R$  is related to the slope of the Raman gain. Especially the self-steepening term has a non-negligible contribution in nonlinear pulse compression (see section 4.6).

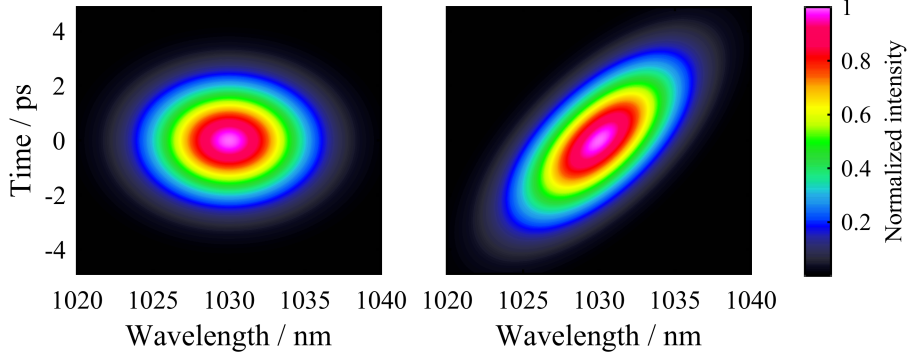


Figure 2.1.: Time frequency mapping of a transform-limited pulse (left) and of a chirped pulse (right).

#### 2.2.4. Propagation of strongly stretched pulses

As described in subsection 2.2.3, calculating the propagation of an ultrashort pulse using the Fourier-split-step approach results in continuous switching between the time and spectral domains. However, if the pulse is already strongly stretched, it is possible to apply both the effect of dispersion and SPM in frequency domain [26]. This requires a pointwise mapping between the pulse in time and spectral domain that does not significantly change during propagation. This can be seen in figure 2.1, where the spectrum of a 200 fs pulse with a central wavelength of 1030 nm is filtered with a Gaussian spectral filter of 0.5 nm bandwidth at different spectral positions. In the transform-limited case, the temporal form of the filtered pulse does not depend on the spectral filter position. Hence, all spectral components exist at all points of the pulse in the time domain. However, in the case of a chirped pulse (the 200 fs pulse being stretched to 3 ps using second-order positive dispersion), the temporal form and position does depend on the filter position. In such a case, the spectral amplitude  $\tilde{A}(\omega, L)$  after a propagation distance  $L$  can be written as [26]:

$$\tilde{A}(\omega, L) = \tilde{A}_0(\omega) \exp \left[ i \left( \phi_0(\omega) + \frac{1}{2} \beta_2 L (\omega - \omega_0)^2 + B s(\omega - \omega_0) \right) \right] \quad (2.17)$$

with  $\phi_0(\omega)$  being the initial spectral phase of the strongly stretched pulse, is  $B$  the B-integral and  $s(\omega)$  represents the normalized spectral intensity profile. It should be noted that the equation only includes the term for second order dispersion, but the other order terms can easily be added.

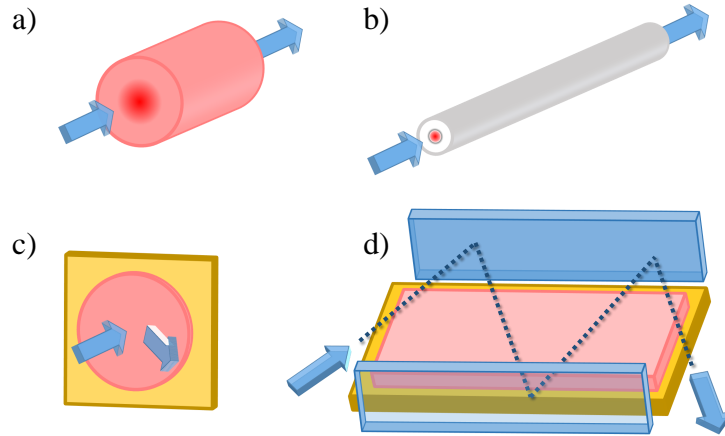


Figure 2.2.: Overview of different amplifier architectures and the signal path the light describes in those architectures: a) rod amplifier b) fiber amplifier c) thin-disk amplifier d) slab laser.

### 2.3. Architectures for the amplification of ultrashort pulses to high average powers

The generation of ultrashort laser pulses started in the 1970s by using dye lasers [27]. With the adoption of the CPA concept and the move to solid-state laser materials [23], their performance could be increased by multiple orders of magnitude. Today, laser systems can emit pulses with peak powers of more than 1 PW [3]. However, the repetition rates of these systems are limited to the Hz-level, resulting in an average power of just a few Watts. This average-power limitation is mostly caused by thermal effects inside the laser material. Due to the quantum defect caused by the energy mismatch between the signal and the pump photons, the quantum efficiency for the laser process, and additional effects such as absorption, heat is generated in the material. In combination with the thermo-optical effect, this heat leads to a change of the transversal refractive index profile [20] and, therefore, to a deformation of the beam profile. To improve the thermal properties of the amplifiers, new geometries of the active medium have been developed over the past decades. The most common are the fiber, the thin disk and the slab. In figure 2.2, they are compared to the standard bulk geometry. What all these advanced laser geometries have in common is that they increase the surface-to-active-volume ratio for a better heat dissipation. Additionally, in the case of a fiber laser (figure 2.2 b)), the signal light is guided by either a difference of the refractive index between the inner part (the core) and the outer part (the cladding) [18] or by other techniques [28, 29].



This guiding mechanism makes the fiber laser very robust against thermal influences, but not completely immune which will be shown in section 2.5. Another possibility is to use a thin disk (figure 2.2 c)) as the laser material and to cool it from the backside, thus reducing the transversal thermal gradient. Finally, the signal can also propagate in a thin slab that is cooled from two sides (figure 2.2 d)). This reduces the thermal gradient in one transversal dimension. In a variant of this design the beam follows an additional zig-zag path in the medium to nearly cancel out thermal effects in the other transversal dimension. With all of these advanced architectures, average powers in the kW-level when amplifying ultrashort pulses have been demonstrated [4–6]. However, the pulse energy and peak power of these systems is still orders of magnitude below state-of-the-art bulk lasers and improving their performance of this aspect is a major point of research. When keeping the repetition rate constant this will also result in even higher average powers. Therefore, for future laser systems, both values have to be improved. In the following, the focus will be set on fiber amplifiers because they are a good basis for the coherent combination concept introduced in this thesis. However, as already mentioned, the considerations can also be applied in a similar way to other laser architectures as well.

### **2.3.1. Ytterbium-doped fiber amplifiers**

Optical fibers have been used for light transportation for a few decades, which has revolutionized the telecom industry. Therefore, it seems natural to employ fibers as a waveguide for the amplification of light, which was first demonstrated in 1964 [30]. Since then the development of the fiber itself, together with semiconductor-based pump sources, has continued relentlessly. Today, ytterbium-doped glass is the material of choice for most high-power fiber amplifiers for short pulses since it provides a broad emission bandwidth of 100 nm around 1030 nm and two strong absorption peaks around 915 nm and 976 nm [31] (which can easily be exploited by pumping ytterbium-doped fibers with commercially available high-power semiconductor pump diodes). Additionally, the quantum defect due to the mismatch of the pump- and signal-wavelength is comparably small. Besides the material, the structure of the fiber also influences the performance of the system. Here, so-called double-clad fiber designs will be considered. These possess a waveguide for the pump light that is larger than the signal core. Hence, low brightness pump diodes with higher average powers can be used and coupled in this pump core. This way the fiber acts as a brightness converter. The guiding mechanism

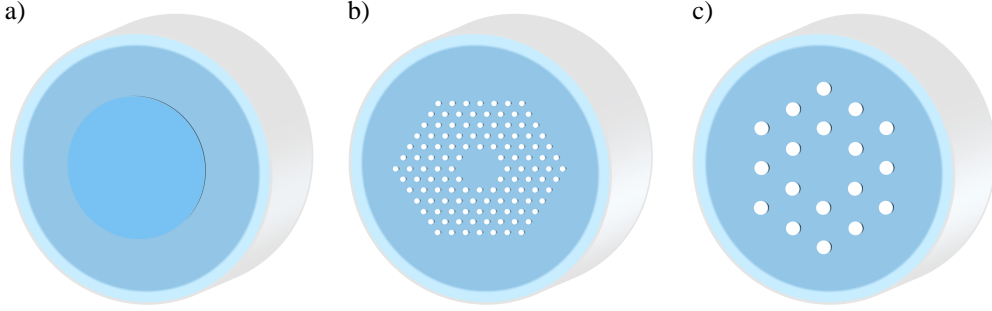


Figure 2.3.: Schematic structure of three different fiber designs: a) step-index fiber b) step-index-like photonic-crystal fiber c) large-pitch fiber

in the signal core and for the pump widely differs between different fiber designs. In figure 2.3, some commonly used designs are shown. The simplest one is the step-index fiber (figure 2.3 a)), which consists of a core with a refractive index  $n_{\text{core}}$  higher than the surrounding refractive index of the cladding  $n_{\text{cladding}}$ . This refractive index difference leads to the existence of one or more optical transverse modes that are guided in the signal core [18]. In this context, the so-called V-parameter plays an important role. It is defined as:

$$V = k_0 a \sqrt{n_{\text{core}}^2 - n_{\text{cladding}}^2} \quad (2.18)$$

with the free-space wave-number  $k_0$  and the radius  $a$  of the core. If the condition  $0 < V < 2.4048$  is fulfilled, the fiber will only guide one nearly-gaussian mode with a specific mode-field diameter ( $\text{MFD} = \sqrt{A_{\text{eff}}/\pi}$  [29]), which is the preferred operation regime for most applications. In order to obtain higher pulse energies and peak powers, larger core sizes are desirable (see subsection 2.4). However, this means that the refractive index difference between core and cladding has to be reduced when the core radius increases. Due to production tolerances, single mode operation for step-index fibers is limited to core diameters of about  $15 \mu\text{m}$  for wavelengths around  $1 \mu\text{m}$  [29]. This can be achieved with photonic-crystal fibers (PCFs) [19] (figure 2.3 b)). In these fibers the signal core is surrounded by multiple rings of microscopic air holes. These holes are small enough to consider the structured material as homogeneous with an effective refractive index that is lower than the bulk material. This way, the guiding mechanism can be considered to be similar to that of a step-index fiber, but with a better controllable refractive index difference. Therefore, larger core sizes can be realized while maintaining single-mode operation. On the other hand, it is possible to increase the core size even further when the guidance of a few higher-order modes is accepted, but only the

fundamental mode is selectively excited and amplified. Alternatively, a photonic band gap structure can be added [32].

Besides the strict definition of single-modedness, meaning that only one mathematical solution for a guided mode exists, the term effective single-mode operation has been established. The definition for effective single-mode operation used here refers to a suppression of the amplification for higher-order modes compared to that experienced by the fundamental mode. For example, if a double-clad fiber is considered, then the modes guided by the second cladding also have to be taken into account. Even though the signal core might only guide one mode in the strict sense, the total fiber can also guide the higher-order modes effectively. However, the overlap with the doped signal core is drastically reduced in this case, resulting in a lower amplification and a suppression of these higher-order modes at the output. The same concept can be applied by having a signal core guiding multiple modes but it is possible to preferably amplify the fundamental mode by introducing a selective doping of certain regions in the signal core [33]. Another design that suppresses the amplification of higher-order modes is the large-pitch fiber (LPF) [29], shown in figure 2.4 c). As the name suggests, in this design the pitch of the air-holes and their diameter are a lot larger than in a standard PCF, and, therefore, an effective refractive index can no longer be assumed. Instead, the fiber works by delocalizing the higher-order modes from the core region [29], resulting in a preferred excitation and amplification of the fundamental mode. The experiments in section 6.3 employ this type of fiber because it provides large core diameters of up to 80  $\mu\text{m}$  while maintaining a nearly constant fundamental mode profile over the whole average-power range. Even though it is theoretically possible to go to larger core diameters, so-called avoided crossings [29] lead to disturbances of the fundamental mode at different average-power levels, therefore, making the handling of such fibers more difficult.

To estimate the beam quality of the output of a fiber, the  $M^2$  value is introduced, which has a minimum value of 1 for a pure Gaussian beam [20] and can easily be experimentally determined [34]. The closer the value is to 1, the better the beam quality is considered to be. Most effectively single mode fibers with large core diameters achieve an  $M^2$  value better than 1.4 [35, 36].

## 2.4. Limitations of the peak power and pulse energy

The peak power  $P_0$  and the pulse energy  $E_{\text{pulse}}$  are two parameters of an ultrashort laser pulse related by the following formula:

$$E_{\text{pulse}} = \int_{-\infty}^{\infty} dt P(t) = P_0 \int_{-\infty}^{\infty} dt \left( \frac{P(t)}{P_0} \right) \quad (2.19)$$

As can be deduced from it, by changing the pulse duration for a fixed pulse form, the factor between both parameters can be altered. Therefore, on the one hand it is beneficial to generate a pulse as short as possible to achieve a high peak power for a given pulse energy. On the other hand, if the pulse duration is prolonged, it also allows for an intentional reduction of the peak power to avoid related detrimental effects. This is utilized in the chirped-pulse amplification (CPA) concept [23]. Hereby, the pulse is first stretched in time using chromatic dispersion, then amplified and finally recompressed. Diffraction gratings are often employed to achieve a large chromatic dispersion. Although in theory this allows for a reduction of the peak-power to a value only limited by the average power, the size of the diffraction gratings employed in the compression stage [37] limit the achievable temporal stretching. The maximum stretched pulse duration  $\tau_{\text{max}}$  using a grating with the grating constant  $d$  and the dimension orthogonal to the grating grooves  $D$  can be estimated as (for the derivation see appendix A):

$$\tau_{\text{max}} \approx \frac{4\pi D}{d\omega_0} \quad (2.20)$$

Hence, for applicable grating sizes of less than 1 m, the stretched pulse duration is limited to a few nanoseconds and both pulse-energy and peak-power limitations have to be considered for fiber amplifiers. The following list shows some aspects to be considered:

- The maximum energy that can be extracted from a fiber
- Damages related to self-focusing of the signal beam
- Limitations due to the B-integral
- Damages at the surface of the fiber

In the following subsections, these aspects will be investigated in detail.

### 2.4.1. Extractable energy

The maximum limit for the extractable energy is determined by the total number of active ions  $N_{\text{ions}}$  in the signal core. However, the maximum fraction that can be inverted is given by:

$$f_{\text{max}} = \frac{\sigma_{12}^{(p)}}{\sigma_{12}^{(p)} + \sigma_{21}^{(p)}} \quad (2.21)$$

with  $\sigma_{12}^{(p)}$  and  $\sigma_{21}^{(p)}$  being the effective cross-sections for absorption and emission of the pump at frequency  $\nu_p$ , respectively. The minimum fraction that has to be inverted (i.e. the transparency-inversion) to avoid absorption of the signal at frequency  $\nu_s$  is given by:

$$f_{\text{min}} = \frac{\sigma_{12}^{(s)}}{\sigma_{12}^{(s)} + \sigma_{21}^{(s)}} \quad (2.22)$$

with  $\sigma_{12}^{(s)}$  and  $\sigma_{21}^{(s)}$  being the respective absorption and emission cross-sections for the signal. Therefore, the maximum energy that can be stored and becomes available in the fiber at the signal wavelength is  $E_{\text{max}} = N_{\text{ions}}(f_{\text{max}} - f_{\text{min}})h\nu_s$ . However, actually extracting all of this energy requires an input signal of infinite energy. This can be seen by investigating the Frantz-Nodvick equation [38, 39]:

$$J_{\text{out}} = J_{\text{sat}} \ln \left( \exp \left[ g_0 \right] \left[ \exp \left[ \frac{J_{\text{in}}}{J_{\text{sat}}} \right] - 1 \right] + 1 \right) \quad (2.23)$$

with  $J_{\text{in}}$ ,  $J_{\text{out}}$  and  $J_{\text{sat}}$  being the input, output and saturation fluences and  $g_0$  is the small-signal gain coefficient. It should be noted that this formula is only valid for a four-level laser system but other systems behave similarly in this regard. Introducing the stored pump fluence  $J_{\text{sto}} = g_0 J_{\text{sat}}$  [40] and the extraction efficiency  $\frac{J_{\text{out}} - J_{\text{in}}}{J_{\text{sto}}}$ , it can be deduced from equation 2.23 that in order to maximize the extraction efficiency,  $J_{\text{in}} \rightarrow \infty$  has to be assumed. However, this would result in a gain  $G = \frac{J_{\text{out}}}{J_{\text{in}}} \rightarrow 1$ . Therefore, for a realistic setup with  $J_{\text{out}} \gg J_{\text{in}}$ , only a fraction of the extractable energy can actually be transferred into the signal pulse. For example, if the stored energy in a fiber is 15 mJ and the saturation energy is 1.3 mJ, only about 12 mJ can be extracted if a gain of 20 dB should be maintained.

### 2.4.2. Self-focusing

The impact of nonlinear effects on the temporal pulse profile were discussed in subsection 2.2.2. However, the intensity-related refractive-index change (equation 2.11) can also be observed in the spatial domain while the pulse propagates through a medium. If a Gaussian-shaped intensity profile of the beam is assumed, this results in a Gaussian-shaped refractive index profile that corresponds to a focusing lens. At a certain point, this self-focusing overcomes the guiding mechanism of the fiber and leads to a collapse of the beam. The resulting extremely high intensity may cause the destruction of the material [41]. The threshold value for this to occur is at a certain critical power  $P_{\text{cr}}$ , which is independent from the beam size and given by:

$$P_{\text{cr}}(\omega) = \alpha \frac{c_0^2 \pi}{\omega n(\omega) n_2} \quad (2.24)$$

where  $\alpha$  is a constant with a value of about 1.83 [42]. This value is valid for propagating in bulk material and in fibers and limits the peak power in fused silica to  $P_{\text{cr}} \sim 4$  MW for linearly polarized light and  $P_{\text{cr}} \sim 6$  MW for circularly polarized light [43].

### 2.4.3. B-integral

The B-integral was introduced as a simple way to estimate the impact of SPM on a laser pulse during propagation in equation 2.12 and on strongly stretched pulses in equation 2.17. If a pulse with a Gaussian spectrum is considered, then the resulting self-imposed phase will also be Gaussian, thus possessing higher-order phase terms. A standard grating compressor does not create a Gaussian-shaped phase and, therefore, it is not possible to completely compensate for this phase, which results in a residual phase profile. In figure 2.4, the impact of different accumulated B-integrals on a pulse starting with a Gaussian spectrum and transform-limited pulse duration of 200 fs is shown. It is assumed that the pulse is strongly stretched (i.e. it is considered to be in the CPA regime) when the nonlinear effects are applied. Additionally, only the second order term of the SPM phase is compensated for. This can be realized in an experiment by slightly changing the distance between the compressor gratings. As can be seen in the figure, the residual phase shifts some amount of the energy of the main pulse into side pulses. Hence, the peak power of the main pulse is reduced. It should be mentioned that the effect is even stronger for pulses with spectra that are not smooth (i.e. show ripples) [25].

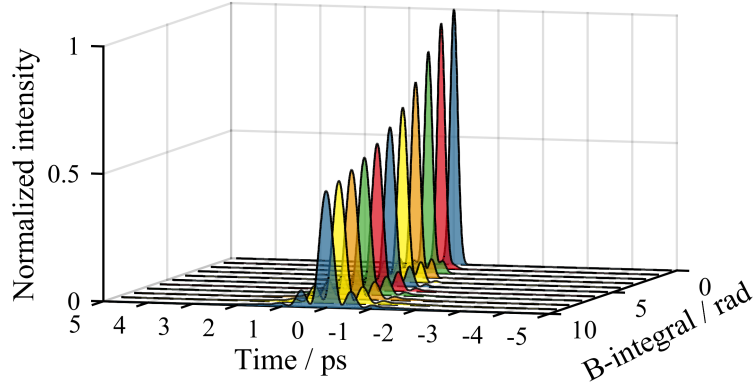


Figure 2.4.: Impact of different accumulated B-integral values on a strongly stretched Gaussian pulse after compression if only second order dispersion is compensated for.

Various mitigation strategies have been developed to counteract this effect. This includes pre-shaping the spectral intensity profile [44] or the spectral phase profile [45]. In the later case, the corresponding compensating phase can be determined with an iterative algorithm [46]. Even though this technique can be successfully applied in fiber CPA systems (see chapter 6), the B-integral still cannot be ignored. The reason is the limited dynamic range and spectral resolution of available shaping elements such as spatial light modulators (SLM). For phase profiles with very large phase amplitudes this leads to phase jumps between adjacent pixels of the SPM, resulting in diffraction of the beam which finally manifests itself as a loss of power at those wavelengths. Additionally, these introduced spectral modulations reduce the quality of the output pulse. Hence, even with phase shaping, the B-integral value still has to be kept below a value of about 10 rad to completely compensate the spectral phase.

#### 2.4.4. Surface damage

Besides the already discussed limitations of the pulse energy and peak power while propagating through a fiber, physical damages can also occur at end facets of the fiber when the laser pulse enters or leaves them. Due to the higher power levels after amplification, the damage will mostly occur at the output side. The value of the damage threshold of a material at a surface is generally lower than that of the bulk material. This is caused by scratches and defects at the surface that lead to an enhancement of the electric field at these points [47]. Since this value depends on a large number of parameters, the measured damage thresholds can vary. However, there is an empirical formula to estimate

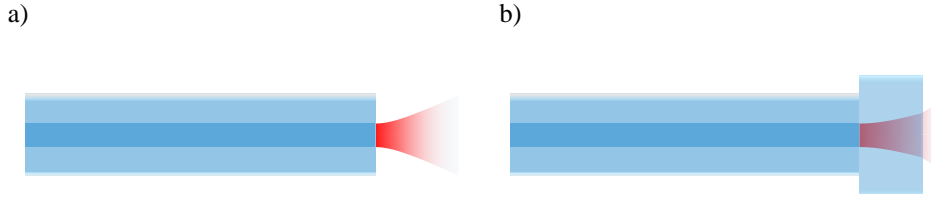


Figure 2.5.: Caustic of the beam at the output of the fiber a) without endcaps and b) with endcaps

the damanger fluence for fused silica at an operation wavelength of 1064 nm and for pulse durations  $\tau$  above 20 ps (which is a valid assumption for high-power fiber-CPA systems) [48]:

$$J_{\text{th}} = (22\dots25) \cdot 10^4 \left( \frac{\tau}{\text{ns}} \right)^{0.4} \frac{\text{J}}{\text{m}^2} \quad (2.25)$$

The pulse duration  $\tau$  is given in ns here. One way to circumvent these issues is to splice fused-silica endcaps at the end of the fiber (see figure 2.5). In this case, the beam expands due to divergence before it reaches the surface, resulting in a lower fluence at the output. It should be noted that the length of the endcap is limited by its radius, i.e. clipping of the output beam at the endcap has to be avoided.

### 2.4.5. Comparison of the different limitations

In figure 2.6, the previously described effects are compared as a function of the MFD in the fiber. A fiber length of 1 m, a dopant concentration of  $3.25 \cdot 10^{25} \frac{\text{ions}}{\text{m}^3}$ , a wavelength of 1030 nm, a gain of 20 dB and a stretched pulse duration of 2 ns have been assumed, making it comparable to the experiments (see section 6.3) and the pulse duration is already in the upper range for typical stretchers used in such systems. Additionally, circular polarization was employed, which increases the thresholds for self focusing and reduces the B-integral by a factor of 1.5 [43] compared to linearly polarized light. As can be seen in figure 2.6, the strongest limitation is caused by surface damage. However, this effect can be strongly mitigated for smaller diameters by splicing endcaps to the fiber (in the calculation a length of 5 mm was assumed). Therefore, for MFDs smaller than  $80 \mu\text{m}$  the allowed B-integral of 10 rad limits the maximum pulse energy. For even larger fibers, the pulse energy has to be kept below 3 mJ to avoid surface damage. In this case,



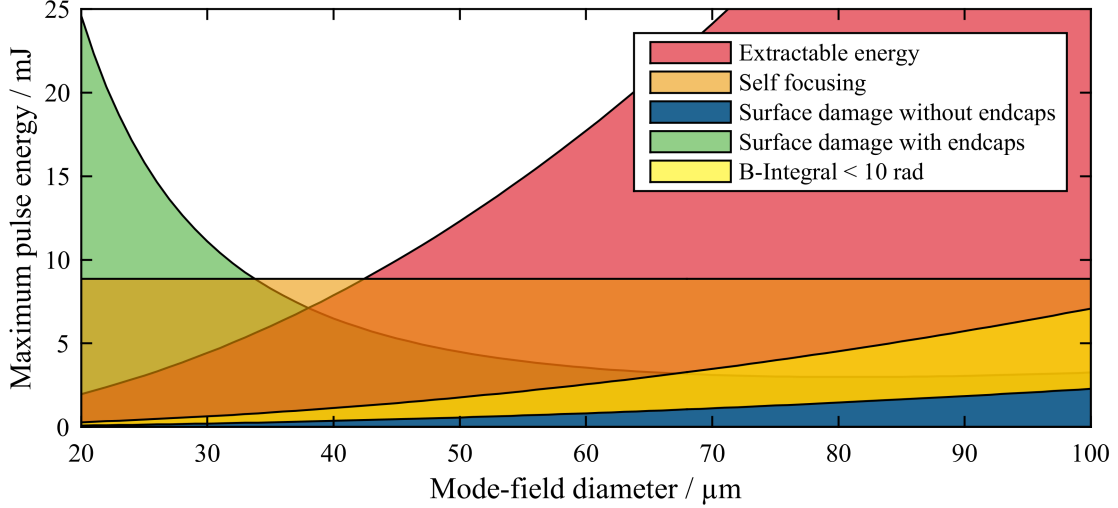


Figure 2.6.: Pulse energy limitations depending on the mode-field diameter for 2 ns stretched pulses.

the use of longer endcaps will be beneficial until the damage of the bulk material itself is reached [49]. The extractable energy is not the limiting factor, confirmed by the fact that the maximum extracted energy from a large-pitch fiber in Q-switched operation [50] is about an order of magnitude larger than for stretched femtosecond pulses [15].

## 2.5. Limitations of the average power

Fiber amplifiers are widely known for achieving high average powers due to the intrinsic advantages described in section 2.3. However, the generated heat in the core can still have detrimental effects ranging from a shrinking of the guided fundamental mode [51] to mode-instabilities [7–9] that limit the maximum average power. The first effect can be neglected for small core sizes [52], but becomes more important for larger core diameters due to the decreasing influence of the waveguide on the propagation (i.e. weaker guidance). For example, the output MFD of a fiber can shrink from 79  $\mu\text{m}$  at low average-power levels to 62  $\mu\text{m}$  at 100 W, which is a decrease of over 20% [51]. Therefore, this effect has to be considered in calculations of the maximum pulse energy and peak power. Alternatively, this effect can also be exploited to achieve mode guiding in an otherwise non-guiding fiber [53].

The more fundamental thermal limitation are mode instabilities, that were first experimentally observed in 2010 [4]. This effect leads to a threshold-like degradation of the

output beam that suddenly changes from the fundamental mode to a superposition of multiple modes once that a certain average power has been reached. The behavior is time dependent, i.e. an oscillation between different superpositions of modes can be observed [8]. Hence, the measured beam-quality value (determined by the  $M^2$  value) is reduced drastically above the threshold. The physical origin of mode instabilities have been a major research topic in the last years. Currently, the best explanation for the root cause of this effect is based on the mismatch of the propagation velocity of different modes in the fiber, which leads to an interference pattern between the fundamental mode and residual higher-order modes being generated along the fiber. Thereby regions where the modes interfere constructively will lead to a larger depletion of the inversion and vice versa. Therefore, the interference pattern is mapped into the inversion pattern in the fiber, which results in a periodic thermal pattern and, ultimately, due to the thermo-optical effect in a periodic refractive-index pattern. This refractive-index profile is basically a grating along the fiber with the same grating period as the interference pattern of the modes. Assuming an additional phase shift between the grating and the interference pattern of the modes, energy can be transferred from the fundamental mode into a higher-order mode [7]. This again changes the structure of the interference pattern, allowing for the process to be reversed so that at a certain point in time the output beam will be again dominated by the fundamental mode. Due to the thermal processes involved, oscillation frequencies between the different states in the kHz range can be observed.

## **2.6. Performance development of femtosecond fiber laser systems**

Over the last decades, the performance of femtosecond fiber laser systems has improved tremendously [7] mainly driven by the development of new fiber designs and the availability of high-power semiconductor diodes [54] delivering multi-kW average powers. In figure 2.7 a) and b), respectively, the evolution of the record pulse-energy and average-power values are depicted over the last years. As can be seen, a nearly exponential growth has been sustained for 20 years. At the time of writing this thesis, the record values were 830 W average power [4] and 2.2 mJ pulse energy [15], which were reached in 2010 and 2011, respectively. However, in the last years no new record values have been reported. Most of the limitations related to the pulse energy and peak power have been described

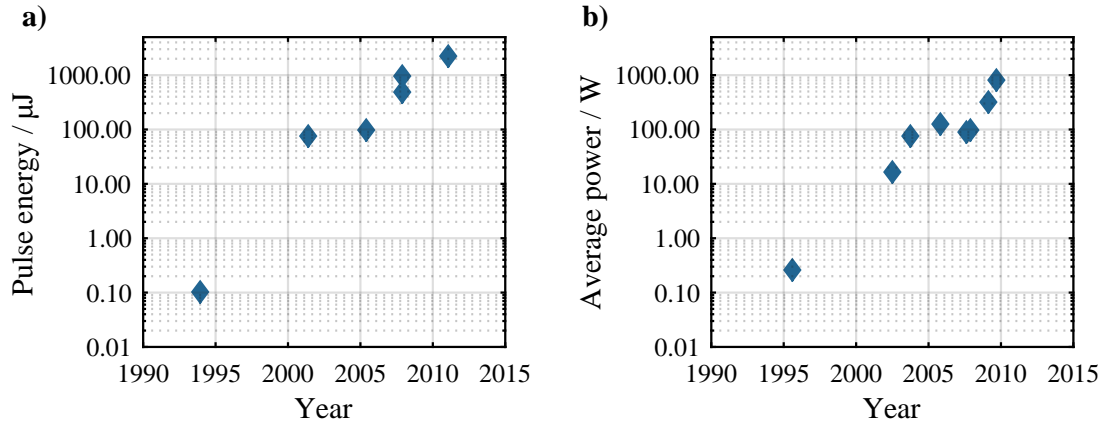


Figure 2.7.: Performance development of femtosecond fiber-laser systems over the recent decades: a) pulse energy [14, 15, 55–57], b) average power [4, 14, 58–63].

in section 2.4. In fact, it was theoretically estimated that the maximum peak power for fibers with an MFD of about  $80\ \mu\text{m}$  should be in the range of 10 GW [64]. Further increases would require even larger MFDs that are difficult to achieve while maintaining single-mode operation. Additionally, the mode-shrinking effect at high average powers becomes more distinct for larger core diameters, thus mitigating the advantages of these larger cores. Another possibility would be to increase the stretched pulse duration by using even larger gratings in the stretcher and compressor. Tiled gratings might be a way to overcome production issues [65]. However, the footprint of the laser system would also increase drastically in this case, therefore, making this approach less viable for table-top systems. For a long time, the average power of femtosecond fiber-laser systems was limited by the available pump power. Today, this is no longer the case for fibers with large core diameters (and, therefore, large pump-cladding diameters allowing for pump diodes with lower brightness).

The main reason for the slow progress in increasing the average power in the last years has been the onset of mode instabilities (see section 2.5). In fact, it has already been shown that average powers of 2 kW from a large-pitch fiber are achievable [66], but no longer in single-mode operation due to this effect. Some active and passive mitigation strategies have been developed [67, 68] and work has been started on producing crystal fibers [69] that consist of materials such as YAG with better thermal conductivity compared to fused silica. But especially the latter technology is still in the very early stages of development. Still, these approaches might allow for further increases of the average power in the future. To achieve higher performance values today, the coherent

combination of multiple amplifiers is of major interest, and it will extensively be covered in the next chapters of this thesis.

# 3. Combination of ultrashort pulses

## 3.1. Basic concept

In chapter 2, the massive progress achieved in the development of fiber laser systems emitting ultrashort pulses over the last decades has been described. However, different physical and technological limitations that make future performance improvements challenging have also been presented. Therefore, it is necessary to think about alternative approaches that might allow increasing the pulse energy, peak power and average power of such systems even further. One of these approaches is the combination of multiple ultrashort pulses. Basically, this means that the outputs of more or less independent systems (often called channels) are added together. The field of laser-pulse combination itself, or even more generally, the combination of lasers, comprises a variety of different techniques. One of the first demonstrations of coherent laser combination was the internal coupling of two semiconductor oscillators [70]. Since then, this concept has been extended to the external combination of the outputs from multiple lasers [71] and, finally, to the combination of fiber amplifiers [72]. While these experiments used continuous-wave lasers, recently the combination of ultrashort pulses from fiber amplifiers was demonstrated [73, 74] as well.

In this chapter the variety of possibilities for ultrashort-pulse combination will be explored and classified. This ranges from spectral combination and non-spectral combination to splitting and combination elements for the beams.

### 3.1.1. Phase-sensitive and non-phase-sensitive combination

In this thesis, the first classification of laser combination techniques that will be made is in phase-sensitive and non-phase-sensitive combination. The difference between both methods lays in the impact that phase fluctuations between the pulses (or the beams themselves in the case of continuous-wave operation (CW)) have on the output of the

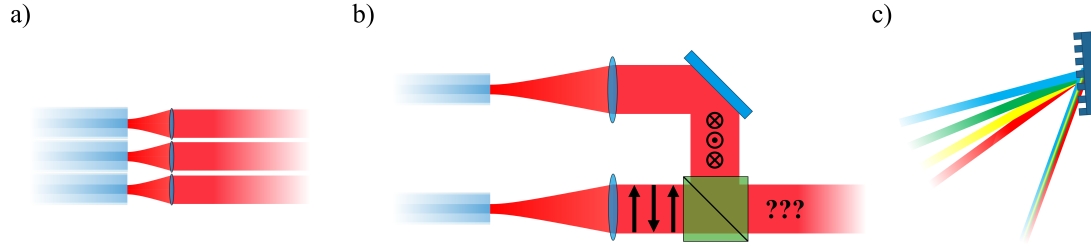


Figure 3.1.: Different non-phase-sensitive combination techniques: a) Side-by-side placement of the amplifiers, b) polarization combination of two linearly polarized beams into an output beam with undetermined polarization state and c) combination of multiple spectrally separated, narrow-bandwidth beams.

system. In the non-phase-sensitive case, occurring phase fluctuations either have no impact or it is small enough to be ignored. For this, the term incoherent combination is sometimes used in this context.

The first example of this type of techniques places multiple laser beams side-by-side without any spatial overlap in the near- and far-field and without any control of the relative phase between them [75], as shown in figure 3.1 a). This is a useful concept if the reduction of beam quality compared to a single emitter is acceptable and no requirement exists on the temporal properties of the beam. The next possibility, illustrated in figure 3.1 b), is to use a polarization-dependent beam combiner to combine beams polarized in orthogonal directions. In this case the combined beam can have a beam quality comparable to that of the two incident beams. However, due to the absence of phase control, the polarization state of the combined beam is undetermined and, therefore, this combination step can only be done once. Finally, as shown in figure 3.1 c), it is possible to employ a diffraction grating to combine beams with multiple spectrally separated components [75]. If the spectral bandwidth of each beam is narrow, the inter-beam angular chirp resulting from the grating can also be reasonably low, which allows achieving a good beam quality. By adding a second grating creating an angular pre-chirp, the angular chirp after combination can be reduced to extend this concept to support a higher spectral density and broader bandwidths [76]. It should be noted that even if every incident beam is CW, the multiple spectral components will result in an output beam with temporal fluctuations. Due to the presence of phase fluctuations, the temporal profile of the beam will not be stable but change over time. Therefore, the application has to be insensitive to this effect.

For the combination of ultrashort pulses, a stable temporal profile of the combined pulse is certainly of capital importance. Additionally, a loss of beam quality is also not acceptable for most applications. Therefore, only phase-sensitive methods will be considered in this thesis. In this field, distinctions between spectral combination and non-spectral combination can be made, as well as between spatial and temporal combination.

### 3.1.2. Spectral combination and non-spectral (or coherent) combination

The next classification that can be done is to distinguish between the spectral and the non-spectral combination of laser pulses. In the first case, the spectral intensity profiles of the pulses are clearly separated. In the second case there is at least some spectral overlap or, in most cases, the spectral intensity profiles are nearly identical. This distinction is supported by the time delay  $\tau$  dependent mutual coherence function for two pulses with the electric fields  $E_1(z = 0, t)$  and  $E_2(z = 0, t)$  that is defined as [77]<sup>1</sup>:

$$\Gamma_{12}(\tau) = \langle E_1^*(t)E_2(t + \tau) \rangle \quad (3.1)$$

Here, it was assumed that the pulses possess the same polarization and beam profile. If the spectral amplitudes and phase profiles  $\tilde{E}_0(\omega)$  of both pulses are assumed to be equal (except for a spectral phase due to the time difference  $\tau$ ), the coherence function can easily be calculated as:

$$\Gamma_{12}(\tau) = \int_{-\infty}^{\infty} d\omega \left| \tilde{E}_0(\omega) \right|^2 \exp [i\omega\tau] \quad (3.2)$$

Depending on the value of  $\tau$  this integral certainly leads to non-zero results. Therefore, the term coherent combination has been established for phase-sensitive non-spectral combination. However, if it is assumed that the spectra of the pulses ( $\tilde{E}_1(\omega)$  and  $\tilde{E}_2(\omega)$ ) are different, the coherence function is:

$$\Gamma_{12}(\tau) = \int_{-\infty}^{\infty} d\omega \tilde{E}_1^*(\omega) \tilde{E}_2(\omega) \exp [i\omega\tau] \quad (3.3)$$

---

<sup>1</sup>Because only a single pulse is considered here and not a pulse train, the definition  $\langle f(t) \rangle = \int_{-\infty}^{\infty} dt f(t)$  is applied instead of the standard time average definition  $\langle f(t) \rangle = \lim_{T \rightarrow \infty} \frac{1}{2T} \int_{-T}^T dt f(t)$ .

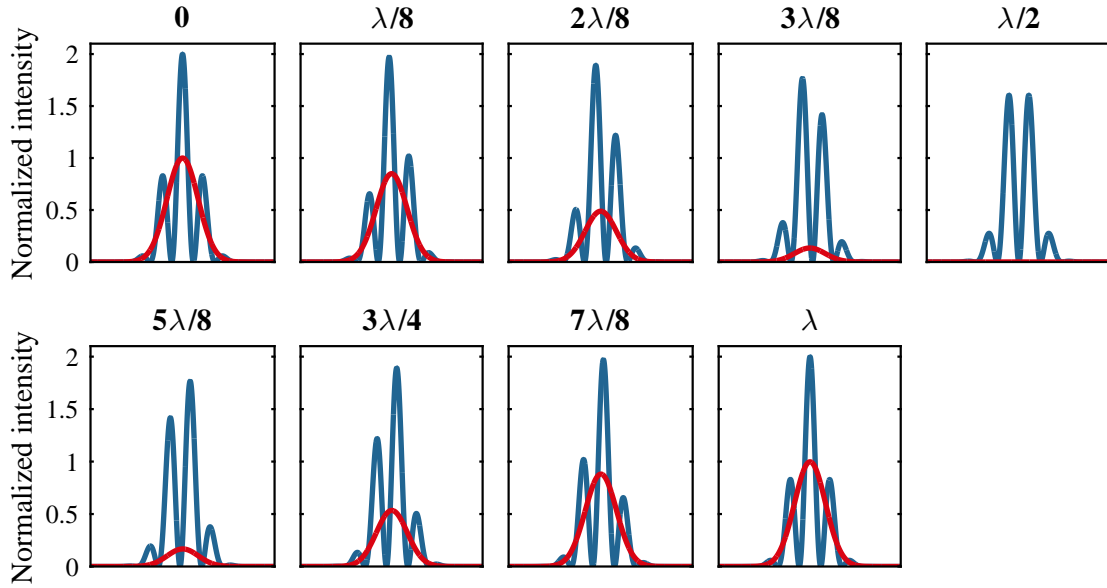


Figure 3.2.: Comparison of the resulting pulse intensity profiles for the combination using the spectral combination technique (blue) and non-spectral (or coherent) combination technique (red) with different delays between the pulses.

Hence, if both spectra are completely spectrally separated,  $\Gamma_{12}(\tau)$  becomes zero. This case is referred to as spectral combination. The difference between both cases can also be demonstrated by the following example. Figure 3.2 shows the combination of two 200 fs pulses applying either coherent combination (red) or spectral combination (blue). In the first case, the spectral pulse profiles are identical, while in the second case the spectrum of the second pulse was additionally shifted from 1030 nm to 1060 nm, which is a large enough shift to avoid any spectral overlap. Then, an additional time delay is applied to the second pulse. A 50:50 ideal intensity combiner (see subsection 3.2.3) was employed for the case of coherent combination case and a dichroic combiner for the case of spectral combination. As can be seen from the figure, for coherent combination the pulse energy changes from constructive interference (for 0 and  $\lambda$  delays) to destructive interference (for a delay of  $\lambda/2$ ). This pattern will be repeated for  $N \cdot \lambda$  and  $(N + \frac{1}{2}) \cdot \lambda$ , with  $N \in \mathbb{Z}$ . However, the contrast between the maximum and minimum will decrease (see subsection 4.2). In the case of zero delay, the energy and peak power of the pulse is the sum of both pulses. In the case of spectral combination, the combined pulse energy



does not change with the delay and the term  $\Gamma_{12}(\tau)$  is always zero, but the temporal pulse form does change drastically. Due to the enhancement of the spectral bandwidth in this case, the combined pulses possess a short feature at the center and the peak power of this feature can be larger than the obtained peak power in the coherent combination case. Because of the spectral gap between the individual pulses, some side pulses appear in the combined pulse.

In summary, this demonstrates that both concepts can be employed to generate a combined pulse. In the case of coherent combination, all of the energy can be shifted into one pulse if the individual pulses possess identical spectral intensity and phase profile. In the case of spectral combination, an additional enhancement of the peak power can be generated. In both cases, the temporal control of the delay is extremely important so that both concepts fall under the term phase-sensitive combination. This will be investigated in detail for ultrashort pulses in subsection 4.2.

Both concepts are applicable for ultrashort pulses emitted by laser systems. However, because a spectral separation of the pulses is required, the supported bandwidth of the system (gain medium, stretcher, compressor, etc...) will limit the number of individual pulses that can be combined with spectral combination. Therefore, as previously mentioned, this concept is very interesting for longer pulses (corresponding to narrower spectra) and CW operation. Nevertheless, there have been some demonstrations with ultrashort pulses coming from fibers that using this technique are able to counteract gain narrowing [78]. Additionally two broadened pulses have also been spectrally combined [79]. In the second example, the channels for each pulse were specifically optimized for a certain wavelength region by choosing the right nonlinear fibers to generate a combined pulse with just one optical cycle. If one also takes a look at other laser concepts, then this wavelength optimization can easily be applied to parametric amplifiers by choosing different crystals or just by tuning their angle [80]. However, for standard ultrashort-pulse fiber amplifiers, the limited gain bandwidth of this gain medium reduces the benefits of this approach. While the combination of amplifiers with different dopants (e.g. ytterbium and thulium) would be possible, a large spectral gap between the gain curves would detrimentally affect the pulse quality (similar to figure 3.2). Therefore, the following parts of the thesis will concentrate on the non-spectral (or coherent) combination of ultrashort pulses.

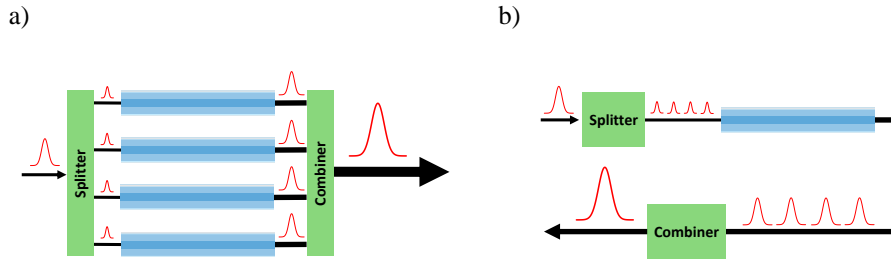


Figure 3.3.: Comparison between a) spatial coherent combination and b) temporal coherent combination for the case of four parallel amplifier channels or four temporal pulse replicas.

### 3.1.3. Spatial and temporal combination

Another distinction that can be made is between the spatial and temporal combination concepts. In the spatial case, the combined laser pulses were previously amplified in spatially separated amplifiers, on the other hand, in the temporal case, they were amplified by the same amplifier subsequently. In both cases the origin of the laser pulses can be from the same oscillator, which should then be followed by a splitting stage that separates them into multiple sub-pulses in the system. The other possibility is to generate the laser pulses independently by using different oscillators. In most scenarios, the first case is preferable because the sub-pulses will automatically be coherent to each other and incoherence can only be introduced between the splitting and combination stages. If an independent generation of the laser pulses is used (e.g. to get pulses at different wavelengths for spectral combination), then special care has to be taken to synchronize the pulses to each other. This synchronization can be realized, for example, passively by optically coupling different oscillators [81]. However, this has not been demonstrated for ultrashort pulses so far. In figure 3.3, two basic setups for spatial and temporal splitting and combination are shown. It should be noted that both approaches can be realized with coherent and spectral combination. However, CPA will be superior to using spectral combination in conjunction with temporal combination for most use cases because it can provide a decrease of the peak power by many orders of magnitude.

The main differences between the spatial and temporal combination schemes are found in the power-scaling possibilities and the way the pulses influence each other during amplification. In the case of spatial combination (figure 3.3 a)), the amplifiers are completely independent from each other. Therefore, every amplifier can be operated at

its highest pulse-energy, peak-power and average-power limit (see section 2.6). If one assumes  $N$  parallel amplifiers of the same type running at the same parameters, emitting equal pulses, then the pulse energy and peak power can also be increased by the same factor  $N$  for the case of perfect combination. If spectral combination is employed, though, then the combined peak power can be even higher than the sum of the individual pulse peak powers. Due to the constant repetition rate, this also results in an average-power increase by a factor  $N$ . Hence, spatial combination is a power-scaling concept for the pulse energy, peak power and average power at the same time. This contrasts with the case of the temporal combination presented in figure 3.3 b), which is also called divided-pulse amplification (DPA) [82]. In this approach the average power cannot be increased above the limit of the amplifier. However, some of the pulse-energy and peak-power limitations can be mitigated. If  $N$  equal temporal pulses are amplified instead a single one, then the peak power is reduced by the same factor. Therefore, limitations due to self-focusing and B-integral (subsections 2.4.2 and 2.4.3) can be mitigated. However, the extractable energy (see subsection 2.4.1) does not change and surface damages (subsection 2.4.4) do not scale linearly with the total duration of the pulse train, because the pulse train can be considered as a single long pulse. Therefore, an increase of the pulse energy by a factor of  $N$  cannot be assumed even in the best case. Additionally, the properties of the amplifier will change during the amplification process (e.g. its inversion will change) and, therefore, one amplified pulse will impact the amplification of subsequent pulses [83, 84].

In summary, a lot of aspects have to be considered to estimate the scaling opportunities of temporal coherent combination. Still, it is a promising concept in combination with long endcaps (to increase the surface damage threshold) to access a larger fraction of the extractable energy for large signal core fibers (see figure 2.6).

Another concept that can be classified as temporal combination is the use of an external enhancement cavity. Generally, the number of pulses that can be combined is a lot larger than in the classical case of DPA with multiple cascaded splitting and combination elements. Therefore, the amplifiers can run in a continuous-pulsed operation mode, i.e. the stored energy is always restored to the same level inbetween two consecutively emitted pulses and the properties of the pulses are constant. With cavity enhancement, an oscillating pulse in the cavity can have an energy that is three orders of magnitude larger than the emitted pulses from the amplifier [85]. However, all experiments have to be realized inside the cavity itself and their impact on the intra-cavity pulse has to be kept low to avoid detrimental effects on the enhancement. One usual application of

these systems is the conversion of light to the XUV spectral region with high-harmonic generation, which has an extremely low conversion efficiency. For other applications, however, the pulse would have to be coupled out of the cavity. Work on this topic has already been started, but it is still in the early stages [86].

It should also be noted that neither coherent and spectral combination, nor spatial and temporal combination exclude each other. In fact, the use of the first two approaches has already been demonstrated in the CW regime [87], as well as the latter two in a proof-of-principle experiment for stretched femtosecond pulses [88].

## **3.2. Splitting and combination elements**

In order to realize a combination of the pulses coming from the different channels as depicted in 3.3 a), a combination of multiple beams is required. The same is true for the combination of multiple pulse replicas as depicted in 3.3 b). In this section the different possibilities to realize the beam combination (and conversely the splitting of one beam into multiple ones) will be discussed.

### **3.2.1. Tiled-aperture and filled-aperture approaches**

The first distinction that can be made is between systems that employ tiled-aperture and filled-aperture spatial combination. In the case of filled-aperture combination, the beams coming from different channels will be overlapped both in the near field and in the far field, as shown in figure 3.4 a). In the example, two beams coming from two different fibers are first collimated and then combined using a polarization-dependent beamsplitter cube from subsection 3.2.3. If one assumes identical beam parameters (i.e. intensity and phase profiles), the combined beam will also possess the same parameters. Therefore, filled-aperture coherent combination basically allows building laser systems where the pulse and beam parameters are very close to those of a single channel, but with higher performance values. However, it also requires dedicated combination elements, which will be described in the next subsections. On the other hand, the tiled-aperture approach (figure 3.4 b)) does not require any combination element at all. Instead, the output beams are placed next to each other, e.g. by placing the fibers adjacent to each other and by employing an array of lenses [89]. In the near field, the beams can be seen side-by-side as in the example for a 4x4 array, as shown in figure 3.4 c). In this

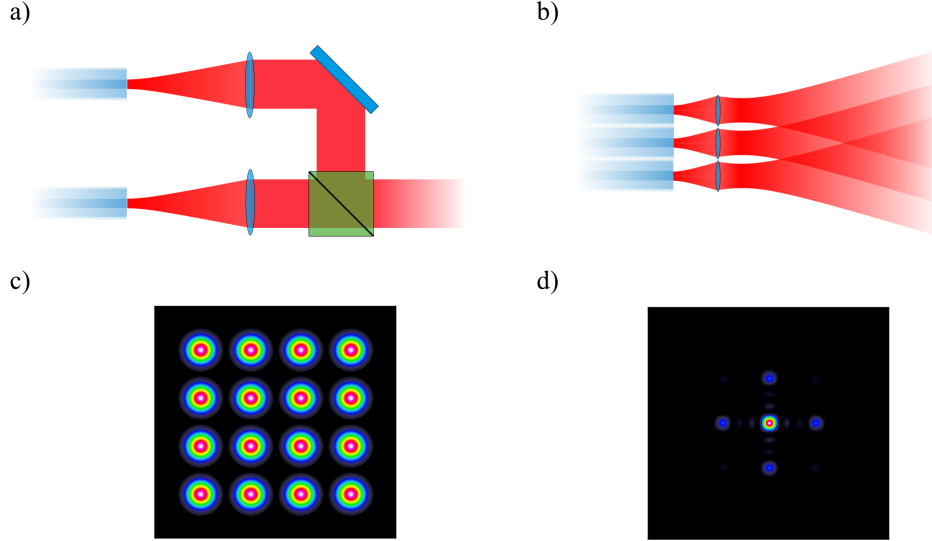


Figure 3.4.: Schematic setup of a) filled-aperture combination and b) tiled-aperture combination. Intensity profile of the near field c) and far field d) of 16x 700  $\mu\text{m}$  diameter beams that are coherently combined in a tiled-aperture configuration.

figure a beam diameter of 700  $\mu\text{m}$  was assumed in combination with a pitch of 1 mm. Additionally, an aperture of 900  $\mu\text{m}$  diameter for each beam was introduced to simulate the impact of the lenses, which reduces the total power by about 9%. Divergence will cause the beams to overlap after a certain propagation distance and create a combined beam profile through the coherent addition of their electric fields. Hence, this method does not work for spectral combination because no constructive interference for the central lobe can take place in this case. The final beam profile in the far field is shown in figure 3.4 d). Even though most power seems to be concentrated in one central lobe, the gaps between the beams in the near field result in the generation of some side lobes. In this example the central lobe only contains about 43% of the power transmitted through the lenses. This can be increased to 50% when employing a hexagonal packing of the beams. A further increase would require a change from a Gaussian intensity profile to one closer to a flat-top profile, which is for example achievable by increasing the diameter of a Gaussian beam and using the aperture to cut the outer parts. However, in this case, more power would be lost at the apertures of the lenses, which would overcompensate the gains made by the higher combination efficiency. Another possibility is to choose a fiber with a fundamental mode closer to a flat-top intensity profile. The different efficiencies depending on the beam diameter are shown in figure 3.5 for the parameters described above. The previously assumed beam diameter of 700  $\mu\text{m}$  already results in

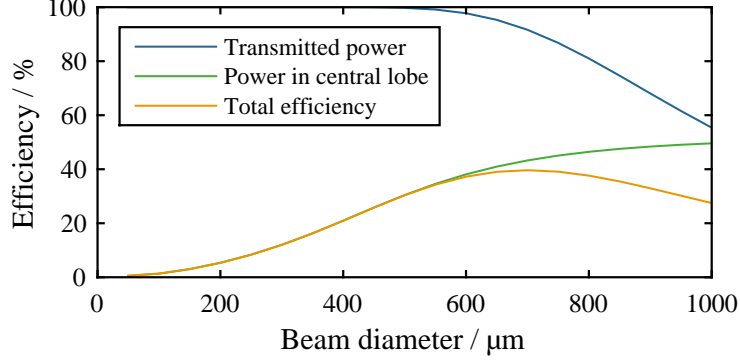


Figure 3.5.: Efficiencies for tiled-aperture combination for a rectangular 4x4 configuration of Gaussian beams depending on the beam diameter. A pitch of 1 mm and apertures of 900  $\mu\text{m}$  diameter for every beam are assumed.

the maximum total efficiency. Even when ignoring the losses at the aperture, only about 50% of the power is in the central lobe. Hence, while the tiled-aperture configuration has the advantage of not needing an element for the beam combination, it generally does not achieve a perfect beam combination. Therefore, the filled-aperture configuration will be preferable in most cases if the challenges for the combination element can be overcome. This will be investigated in the next subsections.

### 3.2.2. Polarization and non-polarization combination

Splitting and combination elements for filled-aperture coherent combination can be realized based on polarization sensitive and non-polarization sensitive techniques. For simplicity, these aspects will be discussed with the combination of two pulses. In the non-polarization case, the electric fields of two pulses  $\vec{E}_1(z, t)$  and  $\vec{E}_2(z, t)$  point in the same direction. If two identical pulses with a small relative delay between them (corresponding to a linear spectral phase) are assumed, then the energy of the combined pulse (e.g. created with a 50:50 intensity 2:1 combiner described in subsection 3.2.3) will change depending on the delay, as seen previously in figure 3.2. If a laser system running at a fixed repetition rate is considered, and therefore, an average power of the system can be defined, then the measurable average power of the output will also change. Of course, the remaining pulse energy and average power do not disappear, but they will appear at a different port of the combiner. In summary, for non-polarization combination, spectral phase differences between the pulses will be reflected in a change of the energy of the combined pulse and the corresponding average power of the combined

beam.

This contrasts with the polarization combination technique. In this case the electric fields of the two pulses are orthogonal to each other. Hence, the mutual coherence function (equation 3.1) results in a value of zero and a change of delay will neither change the combined pulse energy nor the average power of the beam. But the polarization state of the combined pulse will change from linear for zero delay to elliptical polarization and then to circular polarization for a delay of  $\lambda/4$  and back to linear polarization for a delay of  $\lambda/2$ . This pattern will repeat itself for larger delays, but due to the imperfect temporal overlap of the envelopes of the pulses, the contrast between the different polarization states will be reduced (see subsection 4.2). Adding an additional polarizer into the combined beam will project the electric field vector of the combined pulse to a direction given by the polarizer. Changes in the polarization state will then, therefore, be reflected again by pulse energy changes again.

### 3.2.3. 1:2 splitting elements

In general, any splitting element can also be used as a combination element. For clarity they will just be called splitting elements in the following subsections. The simplest implementation of the element is the 1:2 intensity beamsplitter. It consists of a substrate that is anti-reflection coated for the desired wavelength range on one side and has a certain reflectivity on the other one. In figure 3.6 a), the combination of two beams with such an element is shown. In order to interfere, they need to be polarized in the same direction, in this example defined by the p-polarization vector  $\vec{e}_p$ . If a reflectivity  $R$  is assumed (with a corresponding transmittivity of  $T = 1 - R$ ), the combined intensity profile resulting from the transmitted pulse described by  $\vec{E}_1(z, t) = \vec{e}_p E_1(z, t)$  and the reflected one  $\vec{E}_2(z, t) = \vec{e}_p E_2(z, t)$  can be calculated as:

$$\begin{aligned} I_{\text{comb}} &\sim \left| \sqrt{T} E_1(z, t) + \sqrt{R} E_2(z, t) \right|^2 \\ &= T |E_1(z, t)|^2 + R |E_2(z, t)|^2 + 2\sqrt{TR} \Re(E_1^*(z, t) E_2(z, t)) \end{aligned} \quad (3.4)$$

By changing the reflectivity  $R$ , the contrast between the maximum and the minimum of the combined intensity can be maximized depending on the electric fields of the two pulses. The remaining light will be ejected by the other output port of the beamsplitter. For identical pulses, a value of  $R = 0.5$  (i.e. a 50:50 beamsplitter) will give the best result.

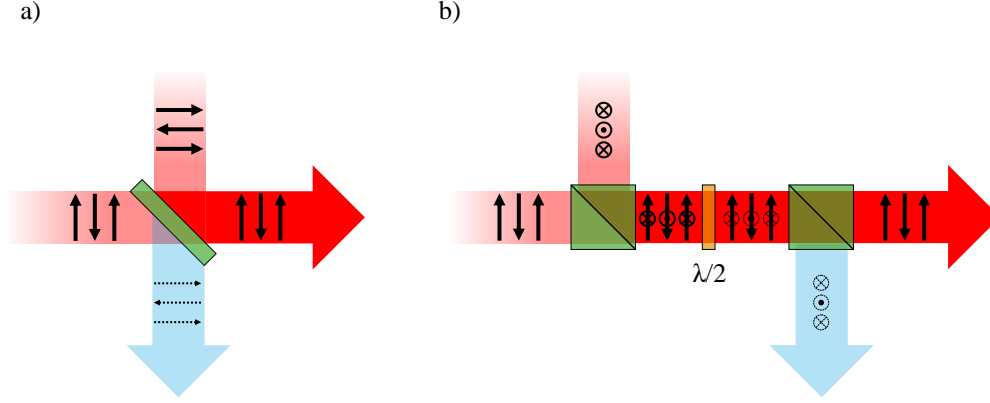


Figure 3.6.: a) 1:2 intensity beamsplitter and b) polarization-dependent 1:2 beamsplitter with additional polarizer cube used as a combination element. The two incoming beams are marked in light red, the combined beam in red and the rejected beam in light blue. The arrows symbolize the direction of the electric field vector.

Using polarization-dependent beamsplitter elements, such as beamsplitter cubes (figure 3.6 b)), on the other hand, seems to be a completely different method at first. However, it will be shown that the result is basically equivalent to equation 3.4. In contrast to the intensity beamsplitter, the electric fields of the incident pulses  $\vec{E}_1(z, t) = \vec{e}_p E_1(z, t)$  and  $\vec{E}_2(z, t) = \vec{e}_s E_2(z, t)$  ( $\vec{e}_s$  is the s-polarization vector) have to be orthogonally polarized in this case. The polarization-dependent beamsplitter consists of two anti-reflection coated prisms with a polarization-dependent dielectric structure in between that reflects s-polarized light and transmits p-polarized light. Hence, the two incident pulses will be combined into a single beam with a variable polarization state (see the previous subsection). Alternatively, a thin-film polarizer can also be employed as a beamsplitter element. A thin-film-polarizer consists of a substrate, which is anti-reflection coated on one side and has a polarization-dependent coating on the other side. Compared to the beamsplitter cubes, the light propagates through less material, resulting in reduced thermal effects and less dispersion. However, the energy related damage threshold is generally lower. Now, if the combined beam is mostly linearly polarized, a  $\lambda/2$  waveplate can be employed to rotate the polarization back to p-polarization or s-polarization (with some remaining energy in the other polarization direction). An additional beamsplitter acting as a polarizer then transmits only the p-polarized part of the beam, thus rejecting the



non-combining energy in the s-polarization. In order to calculate the electric field after the second polarizer, the beamsplitters and the waveplate, which is oriented at an angle of  $\beta$ , need to be defined using Jones matrices [90]. Assuming ideal elements, this results in the following matrices:

$$J_{\text{splitter}} = \begin{pmatrix} 1 & 0 \\ 0 & 1 \end{pmatrix}, J_{\lambda/2} = \begin{pmatrix} \cos(2\beta) & \sin(2\beta) \\ \sin(2\beta) & -\cos(2\beta) \end{pmatrix}, J_{\text{polarizer}} = \begin{pmatrix} 1 & 0 \\ 0 & 0 \end{pmatrix} \quad (3.5)$$

This way, the electric field behind the final polarizer can then be calculated as:

$$\begin{aligned} \vec{E}_{\text{final}} &= (\vec{e}_p, \vec{e}_s) J_{\text{polarizer}} J_{\lambda/2} J_{\text{splitter}} \begin{pmatrix} E_1(z, t) \\ E_2(z, t) \end{pmatrix} \\ &= \vec{e}_p (E_1(z, t) \cos(2\beta) + E_2(z, t) \sin(2\beta)) \end{aligned} \quad (3.6)$$

and, finally, the intensity is:

$$\begin{aligned} I_{\text{comb}} &\sim \cos^2(2\beta) |E_1(z, t)|^2 + \sin^2(2\beta) |E_2(z, t)|^2 \\ &\quad + \cos(2\beta) \sin(2\beta) \Re(E_1^*(z, t) E_2(z, t)) \end{aligned} \quad (3.7)$$

Please note that the free-space propagation between the components has been neglected. It is easy to see that this result is equal to equation 3.4 with  $R = \cos^2(2\beta)$  and  $T = \sin^2(2\beta)$ . Hence, by rotating the waveplate, the setup can be adapted to the incident pulses, e.g. to their power ratio. These results, however, assume a perfect contrast of the beamsplitter. In reality, the non-diagonal elements of the matrix  $J_{\text{splitter}}$  will not be zero and some power might be directed to a wrong output port of the beamsplitter. This effect is a source of power losses and leads to a reduction of the polarization contrast, which can cause additional losses further in the system (e.g. for additional combination steps).

### 3.2.4. 1:N splitting elements

In order for combining techniques to be a viable concept for the scaling of amplifier performance, the number of channels has to be scalable to a larger number. Hence, the splitting into  $N$  beams and their combination back into one single beam has to be realizable. The simplest way to do so is using a cascaded setup of the 1:2 beamsplitters [91] described in the last subsection. In figure 3.7a) the combination of four beams with

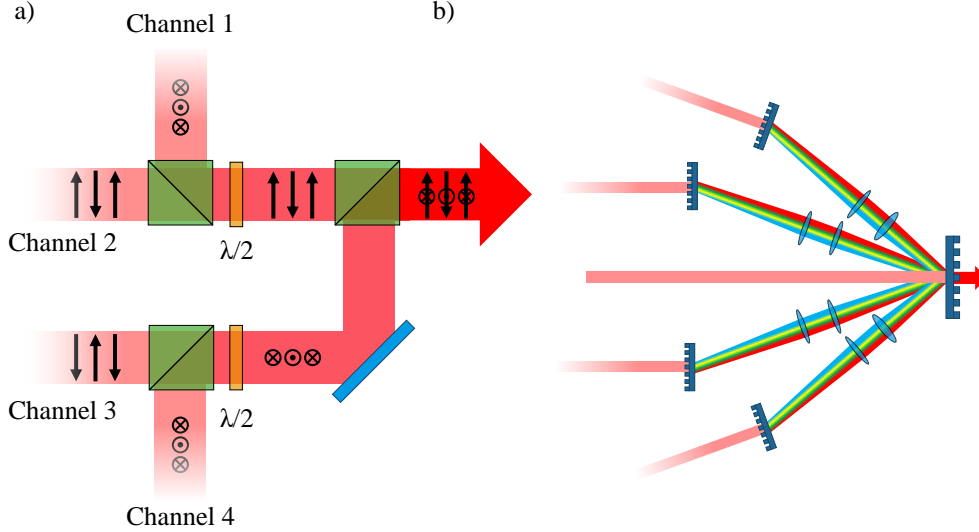


Figure 3.7.: a) Cascaded setup of three polarization-dependent beamsplitter cubes used to combine four beams, b) Schematic setup of the combination of multiple ultrashort pulses with a DOE.

a cascaded setup of polarization-dependent beamsplitter cubes is shown. In the upper left part of the figure, the first and second channel are combined into one beam. With a  $\lambda/2$  waveplate, its polarization can be rotated to p-polarization as described in the previous subsection. Simultaneously in the lower left part of the figure, the third and fourth beam are also combined into one beam. However, the added waveplate is set in a such a way to result in an s-polarized beam. Subsequently, these two beams can be recombined with a third beamsplitter cube. Another waveplate could be added here to set the final beam polarization to the desired state. In fact, such a configuration has been employed in most of the experiments conducted in chapter 6. Of course, intensity beamsplitters could also be instead. However, the setup with polarization beamsplitters allows to emit all linearly polarized power of a certain incident beam the output by rotating the waveplates. Even though such a cascaded setup can be easily realized for a few channels, the number of components required will grow linearly with the channel count, i.e. for  $N$  channels  $N - 1$  elements are required. Additionally, in a setup as shown in figure 3.7 every beam has to pass through  $\log_2(N)$  elements and, therefore, accumulates losses, e.g. due to reflections or imperfect polarization contrasts of the elements. Thus, dedicated 1: $N$  splitting elements that avoid these shortcomings are of great interest. One possibility is to employ a diffractive optical element (DOE) [92] that can split one incident beam into multiple replicas with the same power. Hereby, instead of using

a simple diffraction grating in a certain diffraction order to combine multiple wavelengths, as for the case of spectral combination [75], the different diffraction orders of the grating are employed to realize coherent combination. This technology was already demonstrated in 1986 [71] for the combination of diode lasers. Since then it has been expanded to the coherent combination of fiber lasers [93]. Recently, the combination of 15 fiber lasers in a 2D 3x5 configuration with a total power of 600 W was demonstrated [94]. The side-by-side placement of the beams is similar to the tiled-aperture combination but, due to the DOE, the occurring side lobes in the combined beam can be avoided. Hence, at least theoretically, a perfect combination into a single beam is possible. However, due to the diffractive nature of the DOE, this is only true for CW operation. When using ultrashort pulses with a broad spectral bandwidth, the DOE will cause an angular chirp. In figure 3.7 b), this is shown for a 1:5 DOE. To understand the behavior easily, it is better to consider the splitting from one beam into five beams from right-to-left. Every diffraction order creates an angular chirp, which is different for each beams. With a 4f-setup it is possible to create an equal angular chirp for every beam (except for the central one, which does not possess any angular chirp) by adapting the focal lengths of the lenses. This chirp can then be removed with additional gratings (that can be of the same type and used in the -1 st and 1 st diffraction orders) in every beam. Even though this setup would make the use of a DOE for ultrashort pulses possible, the component count would be roughly comparable to a cascaded setup of 1:2 beamsplitters.

## 4. Efficiency of the coherent combination process

In the previous chapter some of the basic principles of spatial coherent combination were discussed, including some possible splitting and combination elements. It was also discussed that, for  $N$  amplifiers operating at the same power level, an ideal improvement of the pulse energy and average power a factor  $N$  is theoretically achievable. However, this is only true if the spectral intensity and phase profiles of the pulses are identical (a difference of the absolute intensity can be handled by adapting the combination elements accordingly). The same holds true for the spatial intensity and phase profile of the corresponding beams. In real experimental conditions this is not achievable. Any length difference of the dispersive elements (e.g. the amplifiers themselves) or different strengths of the nonlinear effects will cause a difference of the spectral phase profiles in the CPA regime (see subsection 2.2.4), which has a detrimental effect on the achievable combination efficiency [95]. The same is true for mismatches between the beams, e.g. different beam diameters or pointing mismatches. In the following sections it will be discussed how to define and measure the combination efficiency. Additionally, the impact of the above-mentioned mismatches of the pulses and beams will be analyzed, first for the combination of two channels and then extended to a large number of them.

### 4.1. Definition of the combination efficiency

In order to estimate the quality of the combination process, a figure of merit needs to be introduced. This value should include the contributions from both pulse and beam mismatches. Additionally, one has to find a way to describe the efficiency including losses due to the added combination components (e.g. the combination elements or mirrors) and a value for the efficiency which does not include these contributions. Another aspect to consider is the polarization state of the output beams emitted by the

individual channels. Due to depolarization effects their polarization state might not be completely equal. This mismatch will cause a degradation of the combination efficiency. On the other hand, even for single channel systems the power in the wrong polarization state might be lost, e.g. because of polarization-dependent compressor gratings in CPA systems. Therefore, it is important to define if this loss of power should be included in the efficiency value or not. For the case of this thesis, the following rules will be set:

- The term combination efficiency will only include effects strictly related to the combination of pulses and beams, therefore depolarization effects and additional losses due to the components are neglected.
- The term system efficiency will include the power losses due to depolarization. Because of the comparably low channel counts in the experiments, fundamental losses caused by the additionally required components for the coherent combination (e.g. mirrors, combination elements) will be low and will therefore be ignored.

In the case of the polarization combination of two beams, the degree of linear polarization (DOLP) can be defined. It can be calculated by measuring the average power behind the right most polarizer in figure 3.6b) when rotating the waveplate. Thus the maximum and minimum achievable power  $P_{\max}$  and  $P_{\min}$  are measured. Then, the DOLP is defined as [73]:

$$DOLP = \frac{P_{\max} - P_{\min}}{P_{\max} + P_{\min}} \quad (4.1)$$

In the perfect combination case of a beam that is linearly polarized across the whole spatial and temporal domain this will result in a value of one. In the worst case, i.e. two beams that do not interfere at all, the result will be zero. However, it should be noted that the achievable values are ultimately limited by the polarization contrast of the polarizer. Even though this definition works very well for polarization combination of two channels, it is difficult to apply to systems with a larger channel count. In this case, the simplest definition for the combination efficiency is to add the average powers of each individual channel at the output of the system and to compare it to the overall combined power. To do this, it has to be taken into account, that due to the lack of interference when just one channel is operating, only a fraction of its power will arrive at the output. If the measured average power for the  $j$ -th beam is  $P_j$ , the mentioned fraction is  $X_j$  and the combined power  $P_{\text{comb}}$ , then the combination efficiency can be calculated as:

$$\eta_{\text{comb}} = \frac{P_{\text{comb}}}{\sum_j \frac{P_j}{X_j}} \quad (4.2)$$

In order to avoid the impact of depolarization in the individual channels, additional polarization elements might have to be added in order to get the correct result. If a cascaded setup of polarization-dependent beamsplitter cubes is employed as the combination elements, then the waveplates can be rotated in a way that the whole power of a certain channel can be measured at the output. In this case, the condition  $X_j = 1$  is true and equation 4.2 can be simplified accordingly. The system efficiency includes losses due to depolarization effects and losses of the combination elements:

$$\eta_{\text{system}} = \frac{P_{\text{comb}}}{\sum_j P_{\text{raw}_j}} \quad (4.3)$$

with  $P_{\text{raw}_j}$  being the average power directly behind the individual channels but in front of the combination elements. In some cases it might be difficult to measure this value at these points, in which case the system efficiency can be estimated by using equation 4.2 and by adding the power emitted in the wrong polarization direction of every channel to the denominator. However, as mentioned above, losses due to the combination elements are ignored in this case.

In all of these considerations, no differentiation between temporal effects (mismatches of the pulse profiles) and spatial effects (mismatches of the beam profile) has been done. In most cases this is sufficient because the main interest lies in the total efficiency of the combination process. However, especially when optimizing the combination efficiency of a laser system, it is beneficial to estimate the contributions of the various effects. This can be achieved by doing a full measurement of the pulse and beam with techniques such as FROG [96], SPIDER [97] and wavefront reconstruction [98]. In the following subsections, the impact of temporal effects first and the impact of spatial effects later will be theoretically analyzed.

## 4.2. Impact of temporal mismatches of the pulses

The impact of mismatches of the temporal properties of laser pulses can be studied directly in the temporal domain or by Fourier transformation in the spectral domain. In the following sections, the latter possibility will be chosen. As can be deduced from subsection 3.1.2, different wavelength components do not interfere. Therefore, the combination process for every wavelength can be handled independently, followed by integration across the whole spectral range. Hence, strongly stretched pulses in the

CPA regime can be described with equation 2.17. In a first approximation, it will be assumed that the spectral intensity profile in each channel is equal and the impact of dispersion and nonlinear effects will be investigated. Then the spectral phase difference between two pulses can easily be calculated as:

$$\Delta\Phi(\omega) = \frac{1}{2}\beta_2\Delta L(\omega - \omega_0)^2 + \Delta Bs(\omega - \omega_0) + \Delta\Phi_0(\omega) \quad (4.4)$$

with the first term being dispersion caused by a length difference between the dispersive elements (LDEs), the second term being a difference in the B-integral between the pulses, and the last accounting for, e.g. an optical path-length difference. Only second order dispersion is considered here because it has the largest impact on the spectral phase in fused silica. Based on equation 3.4, for every spectral component, the combination efficiency assuming a 50:50 combination element can be then defined as:

$$\eta_{\text{comb}}(\omega) = \frac{1}{2} (1 + \cos(\Delta\Phi(\omega))) \quad (4.5)$$

By integrating over the whole spectral range and weighting with the spectral intensity profile the combination efficiency for two channels can be obtained:

$$\eta_{\text{comb}} = \frac{\int_{-\infty}^{\infty} d\omega s(\omega) \eta_{\text{comb}}(\omega)}{\int_{-\infty}^{\infty} d\omega s(\omega)} \quad (4.6)$$

As previously mentioned, this result is only valid for the combination of two channels, but the model can be extended to a larger channel count by generalizing the average combination efficiency for two randomly selected channels  $\eta_{\text{comb\_av}}$ . If a  $N:1$  combination element for beams with equal intensity profiles is assumed, the efficiency can be calculated using equation 4.2:

$$\begin{aligned} \eta_{\text{comb}} &= \frac{\frac{1}{N} \int_{-\infty}^{\infty} d\omega s(\omega) \left| \sum_j \exp [i\Phi_j(\omega)] \right|^2}{\int_{-\infty}^{\infty} d\omega s(\omega) \sum_j |\exp [i\Phi_j(\omega)]|^2} = \frac{\frac{1}{N} \int_{-\infty}^{\infty} d\omega s(\omega) \sum_j \sum_k \exp [i\Delta\Phi_{jk}(\omega)]}{C \cdot N} \\ &= \frac{1}{C \cdot N^2} \sum_j \sum_k \int_{-\infty}^{\infty} d\omega s(\omega) \cos (\Delta\Phi_{jk}(\omega)) \approx \frac{1}{N} + \left(1 - \frac{1}{N}\right) (2\eta_{\text{comb\_av}} - 1) \end{aligned} \quad (4.7)$$

with the absolute spectral phase  $\Phi_j(\omega)$  for the  $j$ -th channel, the phase difference  $\Delta\Phi_{jk}(\omega) = \Delta\Phi_j(\omega) - \Delta\Phi_k(\omega)$  between the channels  $j$  and  $k$ , and the factor  $C = \int_{-\infty}^{\infty} d\omega s(\omega)$ . The

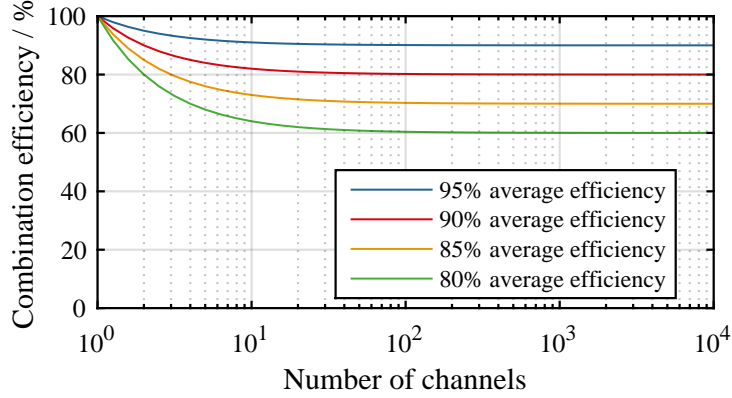


Figure 4.1.: Overall combination efficiency for an increasing number of channels depending on the average combination efficiency between two channels.

spectral phases for the channels are independent from each other. In figure 4.1 the result is shown for different values of  $\eta_{\text{comb\_av}}$ . As can be easily seen for  $N \rightarrow \infty$  the efficiency converges towards a fixed value  $2\eta_{\text{comb\_av}} - 1$ . Please note that this is a theoretical result and does not include losses due to the combination elements, which might grow with the number of channels. However, the results show that the total combination efficiencies for a large number of channels still results in an acceptable value (above 50% in all cases). Therefore, the combination process itself does not limit the possibility to realize such systems.

### Optical path-length differences

To investigate the impact of optical path-length differences (OPDs), only the case where the OPD is a multiple of the carrier wavelength will be considered. In this case, constructive interference of the electric fields will occur (see figure 3.2), but the overlap of the temporal pulse envelopes might be less than perfect. This will be true for most systems with active path-length stabilization, because they can generally only optimize the efficiency to a local maximum (see chapter 5). As a consequence, the intensity ratio at each point in time of two partially overlapping pulses will be different. In order to achieve a perfect recombination, the properties of the combination element would have to be changed while the pulses are passing through it. However, such a dynamic combination element is currently not realizable (the change would have to occur on femtosecond time scales). Even if this were possible, for a large OPD the combined pulse would have a strongly changed temporal profile compared to the single pulses and, therefore, be of little interest. Hence, the discussion will concentrate on the cases where the length



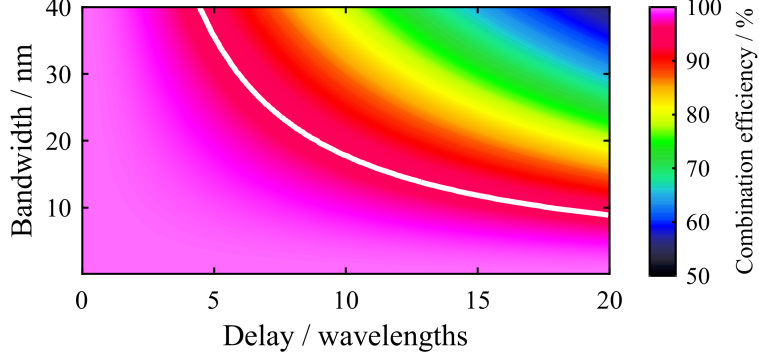


Figure 4.2.: Combination efficiency for two pulses with a Gaussian spectral profile depending on the spectral bandwidth of the pulses and the delay  $k$ . The white line denotes a combination efficiency of 90%.

difference is of the order of a couple of wavelengths. Such precision in the  $\mu\text{m}$ -scale can easily be achieved with standard translation stages. A delay  $\Delta l$  of a multiple  $k$  of the carrier wavelength is represented by a linear phase in the spectral domain:

$$\Delta\Phi(\omega) = \frac{\Delta l}{c}\omega = k\frac{\omega}{\omega_0} \quad (4.8)$$

In order to get predictions for the impact of this additional phase on the combination efficiency, the spectral intensity profile  $s(\omega)$  has to be defined. A Gaussian profile will be assumed here, which allows solving equation 4.6 analytically. Thus,  $s(\omega)$  (with a full-width-half-maximum bandwidth  $\omega_{\text{FWHM}}$ ) is defined as:

$$s(\omega) = \exp\left[-4\ln(2)\left(\frac{\omega - \omega_0}{\omega_{\text{FWHM}}}\right)^2\right] \quad (4.9)$$

Using equations 4.6, 4.8 and 4.9, the resulting combination efficiency can now be calculated to be:

$$\eta_{\text{comb}} = \frac{1}{2} + \frac{1}{2} \exp\left[-\frac{\left(\frac{2\pi k\omega_{\text{FWHM}}}{\omega_0}\right)^2}{16\ln(2)}\right] \quad (4.10)$$

This means, assuming a value for  $\omega_0$  corresponding to a center wavelength of 1030 nm, that the combination efficiency only depends of the spectral bandwidth and on the OPD. Hence, it can be depicted as a 2D plot as done in figure 4.2. If one sets a minimum acceptable combination efficiency of 90%, then the allowed OPD between the pulses is heavily dependent on their spectral bandwidth. This can be easily explained in the temporal domain, where a transform-limited pulse with a broader bandwidth is equivalent

to a shorter pulse. Therefore, a certain OPD has a more detrimental impact on the temporal overlap of these pulses than it has on longer pulses with narrower bandwidths. Even though the considered pulses are strongly stretched in the CPA regime, this has no impact on the previous statements because the applied phase from the stretcher will be equal for both pulses and does not result in any phase difference.

As an example, for a system with about 200 fs pulse duration, corresponding to about 10 nm bandwidth, a OPD of 20 wavelengths is acceptable to keep the combination efficiency above 90%. As described before, this is easily achievable in experiments. For shorter pulses, a more sophisticated mechanism will be required, e.g. some control electronics that find the best combination efficiency by controlling the path lengths.

### Dispersion and nonlinear effects

Optical path-length differences can be easily compensated by controlling the path lengths of the individual channels. On the other hand, the compensation of the two first terms for the spectral phase in equation 4.4 is more challenging. LDE differences will mostly be given by length differences of the amplifiers themselves and B-integral differences will even occur for amplifiers of the same type and same settings when the gain characteristics are different, e.g. due to different couplings of the input signal into the fiber. It should also be mentioned that both effects are not completely independent from each other, e.g. an LDE difference can lead to a difference of the B-integral. However, it will be seen that realistic values for both properties result in an acceptable reduction of the combination efficiency. To calculate the impact, Gaussian shaped spectra from equation 4.9 will be assumed. The B-integral introduces a phase shift, which is strongest at the maximum of the pulse intensity in the temporal domain. Therefore, B-integral differences have their maximum impact on the combination efficiency exactly where the highest power is located in the pulse. In reality, a small OPD between the pulses is introduced to compensate for the phase at this point. So a compensation phase  $\Delta\Phi_{\text{comp}}$  is introduced and the condition  $\Delta\omega \ll \omega_0$  from section 2.1 is assumed:

$$\Delta\Phi_{\text{comp}} = -\Delta B \frac{\omega}{\omega_0} \approx -\Delta B \quad (4.11)$$

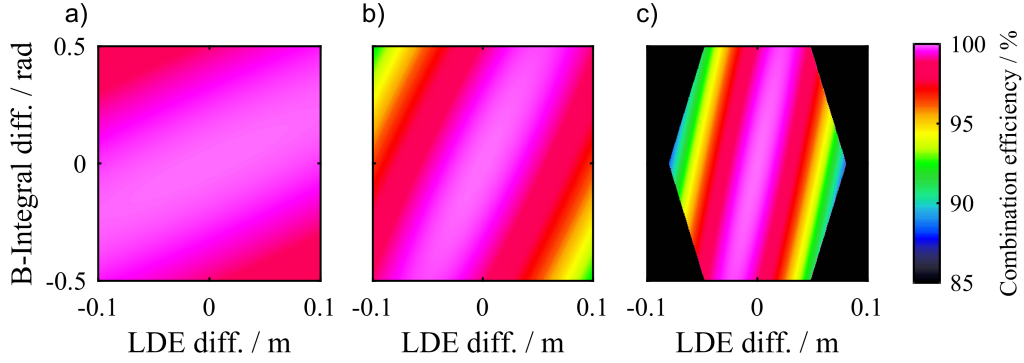


Figure 4.3.: Combination efficiency for two channels as a function of the B-integral and LDE difference for different signal spectral bandwidths a) 10 nm b) 20 nm c) 30 nm.

This phase can now be added to equation 4.4 and used in combination with equations 4.6 and 4.9 to calculate the combination efficiency:

$$\eta_{\text{comb}} \approx 1 + \frac{1}{2} \left( \frac{1}{\sqrt{2}} - \frac{1}{2} - \frac{1}{2\sqrt{3}} \right) \Delta B^2 - \frac{3}{1024 \ln(2)^2} \omega_{\text{FWHM}}^4 \beta_2^2 \Delta L^2 \quad (4.12)$$

$$+ \frac{1}{32 \ln(2)} \left( 1 - \frac{1}{2\sqrt{2}} \right) \omega_{\text{FWHM}}^2 \beta_2 \Delta L \Delta B \quad (4.13)$$

As can be seen the equation depends on the B-integral difference, the LDE difference, the bandwidth, and the dispersion coefficient  $\beta_2$ . For the last parameter, a value of  $0.019 \frac{\text{ps}^2}{\text{m}}$  for fused silica at 1030 nm [99] is used in this example. However, this still leaves an equation with 3 parameters that can be independently chosen. Therefore, in figure 4.3, multiple graphs are shown for different signal spectral bandwidths of 10 nm, 20 nm and 30 nm. In the last graph, certain areas are shown in black to indicate that the approximation made in the equation is no longer valid. In the other cases, the error is less than 3.5%. The first observation is that dispersion has a stronger effect on broader spectra. Therefore, LDE differences have to be kept low in this case compared to pulses with narrower spectra. Still, as long as the value is below 1 cm, the effects are negligible. The effect of the the B-integral differences alone are independent from the bandwidth, as could be expected from the lack of dependence on the bandwidth of the first term in the equation. However, the last term describes the interplay with dispersion and can introduce a dependency on the bandwidth. Due to the opposite signs of the terms, both effects can partially compensate each other. Hence, in a system with an intrinsic LDE difference, parameters of the amplifiers in the channels, such as input and output pulse energy, can be setup in a way that they purposefully create a B-integral difference to

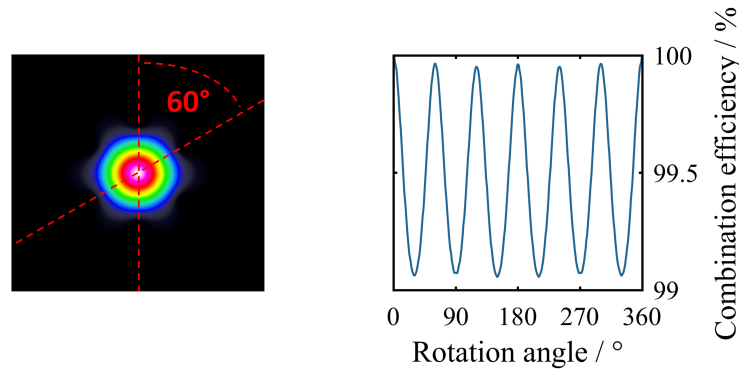


Figure 4.4.: Theoretical intensity profile of a beam emitted by an LPF (without thermal load) and the combination efficiency for two channels if the fibers are rotated against each other.

increase the combination efficiency.

### 4.3. Impact of beam profile mismatches

Besides the temporal mismatches, spatial mismatches of the beams have a major impact on the combination efficiency, including mismatches of the beam intensity profile (form and size) and phase mismatches such as a different divergence. In general, these mismatches will be constant over the different pulses when the beams are emitted by a fiber. Therefore, results of theoretical investigations for coherent combination of CW systems also apply here. For these systems extensive investigations of this topic have already been performed [100]. It turns out that the relative mismatches (i.e. the root-mean-square of the variations over the mean value) of the absolute power, the beam size, pointing and divergence have a quadratic impact on the combination efficiency. Hence, mismatches of these parameters of 10% will result in a drop of efficiency of about 1%. This means that for a carefully designed and adjusted system, like for the temporal mismatches, high combination efficiencies will be achievable even with a large number of channels.

One contribution that can be calculated easily is caused by the fact that the LPF and, therefore, the emitted beam do not have a rotation symmetry for every angle. The intensity profile of the emitted beams by these and other PCFs has a slightly hexagonal shape, and, therefore, the combination efficiency can drop if they are rotated against

each other in angles that are not a multiple of  $60^\circ$ . In figure 4.4, this has been calculated for a simulated LPF beam profile. As can be seen, the efficiency drops by about 1% in the worst case for an angle of  $30^\circ$ , and reaches a maximum for every  $60^\circ$  rotation (deviations from 100% are caused by numerical errors).

## 4.4. Impact of the failure of individual channels

When implementing a system with a large number of channels the probability of one of the channels failing grows. If  $N$  channels and a failure probability of each individual channel  $p_f$  per time frame are assumed, the number of expected faulty channels  $A$  is  $N \cdot p_f$  in this time frame. Therefore, it is necessary to investigate the impact on the combination process of such a failure. The two aspects that have to be considered are the detrimental effect on the combination efficiency and how the stabilization system will behave in this case. The latter will be investigated in the next chapter. In the following, the focus will be on the resulting combination efficiency. If one channel is still partially functional (e.g. just the output power drops), then the considerations done in subsection 4.2 apply. However, the most catastrophic case will be a total failure caused by the destruction of the amplifier or a defect of the pump source. Hence, equation 4.7 will be investigated with  $s(\omega) = 0$  for a number  $A$  of faulty channels. This results in a combination efficiency of  $\eta_{comb} = (N - A)/N$  for the remaining  $N - A$  channels. Please note that for setups based on polarization combination, adjusting the waveplates can avoid this efficiency drop. To calculate the remaining output power fraction of the system compared to the case when all channels operate, this efficiency has to be multiplied with the term  $(N - A)/N$ , which describes the remaining fraction of total available power:

$$\eta_r = \frac{(N - A)^2}{N^2} \quad (4.14)$$

Inserting the expected value calculated above results in  $\eta_r = (1 - p_f)^2$  and is independent from the number of channels  $N$ . Therefore, while the probability of failure of at least one channel in the system grows with the number of channels, the expected fractional efficiency drop (e.g. the power loss relative to the total power when all channels are operating) is constant.

## 4.5. Improvements of the pulse and beam quality with coherent combination

In the previous section the combination efficiency for ultrashort pulses was investigated. In most cases the highest possible efficiency is desired and a deviation from the perfect combination case is considered as a loss of power. However, it should also be noted that this power loss might not be only caused by misalignments and misconfigurations of the system, but also by the filtering effect of coherent combination. This means that distortions of the beam and pulse profile, which could be introduced in a channel, can be partially suppressed. Starting with equation 2.1 for  $N$  equal pulses  $\vec{E}_j(x, y, z, t) = \vec{E}(x, y, z, t)$  individual beam distortions  $\delta T_j(x, y)$  and  $\delta E_j(z, t)$  are added to each one. These additional distortions do not interfere with the other pulses and, therefore, assuming an equal splitting factor of the combination element of  $1/N$ , the resulting combined intensity profile can be calculated as:

$$I_{comb} \sim N \left| \vec{E}(x, y, z, t) \right|^2 + \frac{1}{N} \left( \sum_j |\delta T(x, y) E(z, t)|^2 + |T(x, y) \delta E_j(z, t)|^2 \right) \quad (4.15)$$

for  $\delta T_j(x, y) \delta E_j(z, t) \ll T(x, y) E(z, t)$ . Hence, distortions are suppressed by a factor of  $N$  compared to the combining parts. This effect can be employed to clean the combined beam profile, which might improve its  $M^2$  value. Temporal distortions of the pulses in the individual channels can also be suppressed, leading to a cleaning of the combined temporal pulse form. Additionally, the impact of dynamic incoherent processes, which are different for each channel such as amplified spontaneous emission (ASE) and intensity fluctuations can also be reduced in the combined output.

## 4.6. Coherent combination of spectrally broadened pulses

In the previous sections the focus of the thesis has been set on the coherent combination of pulses emitted by amplifiers located in the respective channels. However, the coherent combination concept is not limited to that case. It can also be applied to overcome some of the limitations of nonlinear compression as well. Here, a spectral broadening

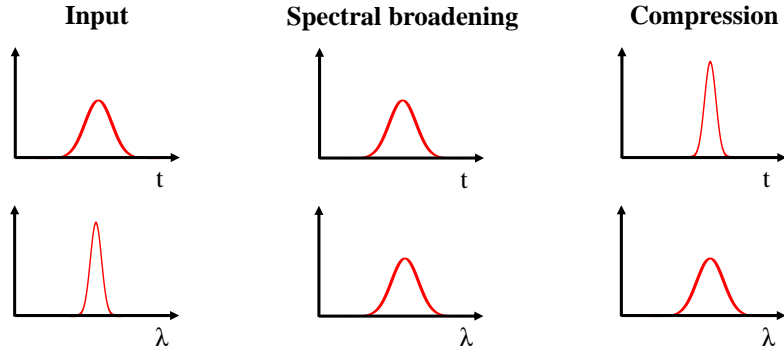


Figure 4.5.: Basic working principle of nonlinear compression. The input pulse is spectrally broadened, followed by temporal compression.

exploiting SPM followed by temporal recompression is employed to generate shorter pulses than those coming directly from a laser system [101]. The working principle of this process is shown in figure 4.5. Similar to what happens in amplifiers, there are some effects that limit the achievable peak power and peak intensity of the incident pulses. In solid-core fibers, these effects are mostly imposed by the comparably low threshold for self-focusing (subsection 2.4.2). Therefore, gas-filled hollow-core fibers are often used for high peak powers, where the broadening and the self-focusing threshold can be adapted by changing the gas pressure. However, the ionization threshold of the gas sets an ultimate limit for the peak intensity and, due to the limited size of the core diameter of the hollow-core fiber (to keep a good beam quality), also for the peak power. On the other hand, working at high average powers can always lead to thermal problems and decrease the stability of the system. Hence, applying the same reasoning as in the case of amplification, the coherent combination of multiple channels should also overcome the limitation of nonlinear compression. Moreover, in this case similar techniques as before can be applied. This includes the basic setup for spatial and temporal combination shown in figure 3.3, the splitting and combination elements and the considerations about the combination efficiency. However, due to the spectral broadening, the absolute B-integral value will be much higher than in the case of amplifiers and, therefore, the resulting B-integral differences can also be significantly higher. In this section this issue will be investigated in detail.

Due to the mentioned larger B-integral differences, the simple analytical model from subsection 4.2 cannot be applied anymore and numerical simulations based on the Fourier-split-step approach will be employed instead. To do that, realistic parameters have to be defined for the simulation. The nonlinear compression both in solid-core and in hollow-

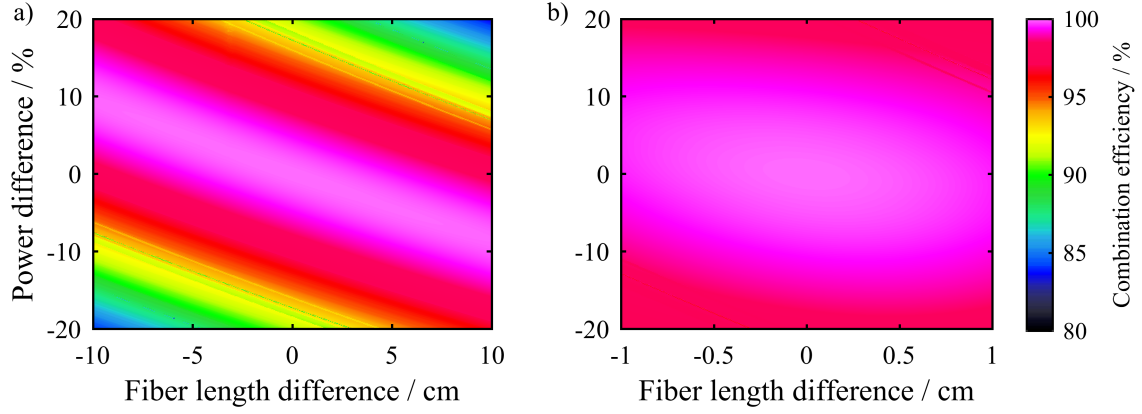


Figure 4.6.: Combination efficiency of two 210 fs pulses that have a) 1 mJ energy and are spectrally broadened in a hollow-core fiber and b) have 1  $\mu$ J energy and are spectrally broadened in a 80  $\mu$ m MFD solid-core fiber.

core fibers will be considered and experimental results of the first case will be shown in section 6.5. A solid-core fiber based on fused silica with a length of 10 cm and an MFD of 80  $\mu$ m is assumed. The incident pulses have a duration of 210 fs (based on the minimum achieved pulse duration in chapter 6) and an energy of 1  $\mu$ J each. For the solid-core fibers, the contributions of dispersion are comparably small due to the short fiber length. For the hollow-core fiber (used for high-peak-power operation) the incident pulse energy is 1 mJ. A 1 m long, 1.5 bar argon-filled hollow-core fiber with a mode-field diameter of 250  $\mu$ m is used as the broadening media. Dispersion is neglected here due to its low value in the gas, so only SPM and self-steepening are taken into account. In figure 4.6, the corresponding combination efficiencies for both cases are shown if a mismatch of the fiber length and the incident power is assumed. The combination of the fiber length and the incident power mismatch leads to a B-integral difference (and in the case of the solid-core fiber to a LDE difference) and to a detrimental effect on the combination efficiency. For the hollow-core fiber, the dominance of the nonlinear effects and the absence of dispersion leads to a strong dependency on power differences compared to fiber length differences. For the solid-core fiber the resulting spectral broadening is smaller (75 nm 10 dB bandwidth compared to 100 nm for the hollow-core fiber). Therefore, the impact of parameter differences has a lower overall impact and due to the presence of dispersion, power differences and LDE differences both have a comparable impact. In any case a good match of the fiber lengths and the parameters causing B-integral differences, such as the gas pressure in the fibers and the incident power, is beneficial. Additionally, the



OPD has to be kept low due to the broad bandwidth, as previously demonstrated. It will be demonstrated in section 6.5 that such a system with nonlinear compression in a solid-core fiber can be realized experimentally.

# 5. Path-length-stabilization techniques for coherent combination

## 5.1. Introduction

In the last chapter it was already explained that the control of the relative phases (i.e. OPD) between the pulses is necessary for the coherent combination of ultrashort pulses. For example, local maxima of the combination efficiency for two pulses are achieved if the OPD is a multiple of the carrier wavelength. Otherwise, a drastic drop of the efficiency can be observed, including the possibility of operating at local minima. Hence, the control of the relative OPD between the pulses at this sub-wavelength scale is of major importance to make coherent combination systems work. This includes static changes for the initial adjustment of the system but also the dynamic compensation of changes that occur due to fluctuations during operation. These fluctuations can be caused by air movements, mechanical vibrations of the components or thermal effects. In this chapter the stabilization techniques will be categorized into active and passive techniques and their difference will be explained and then two of the major active techniques will be explored in detail.

### 5.1.1. Passive and active stabilization techniques

One distinction that has to be made regarding OPD stabilization techniques is between passive and active ones. In the first case the OPDs are either intrinsically zero or are automatically compensated by the system itself. In the second case, active stabilization, an external system controls the individual path lengths of the channels during operation. One example for passive stabilization is a DPA setup using the same element for splitting and combination of the pulses as illustrated in figure 5.1 a) [82]. If the propagation of each pulse replica is tracked from the start to the end (each replica is denoted by a different

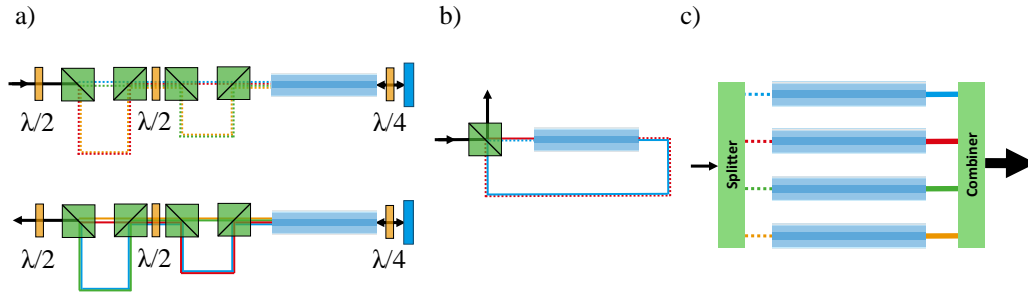


Figure 5.1.: Comparison of coherent combination setups that are intrinsically stable (i.e. that use passive stabilization techniques), such as a) DPA with a single splitting and combination element or b) Sagnac interferometer, with c) the spatial combination of multiple parallel amplifiers, which has to be actively stabilized. The different colors for the beams denote the different pulse replicas. Dashed lines: pulses before amplification, solid lines: pulses after amplification.

color in figure figure 5.1 a)), it can be seen that the travelled path length is always identical. Due to the comparably short duration of the pulse train in time (in the ns range), possible fluctuations that might change its path length can be largely neglected, because the time scale for these changes is typically much longer. This fact makes this setup inherently stable. However, once that a significant part of the stored energy has been extracted from the amplifier by a pulse, this will affect subsequent pulses, resulting in a reduced combination efficiency [83, 84]. This illustrates the limits of this technique because there are not enough degrees of freedom to optimize the system. An adaptation of this approach to the spatial combination approach is clearly not possible due to the spatially separated propagation of each pulse as depicted in 5.1 c). The only partially related approach is to employ a Sagnac interferometer (as shown in figure 5.1 b)) [102], but this is not easily scalable to a larger number of channels or to higher average powers (same as DPA) because every pulse has to pass through all of the amplifiers (if multiple amplifiers are employed). The way around these limitations would be a system which can automatically adapt itself to OPD changes. As previously stated, coupled oscillators have been realized for CW operation and narrow-bandwidth pulses, but not for ultrashort pulses. Hence, for the spatial coherent combination technique, an active stabilization mechanism is necessary.

## 5.2. Active stabilization techniques

Active stabilization techniques are either based on detecting phase differences between the pulses directly or deriving them by slightly dithering the phases and measuring the impact of these changes on the output power. From this phase information, an error signal can be calculated which, is used to change the path lengths in the channels accordingly. For both the detection and the change of the path length a variety of different techniques exist. This thesis will focus on the detection of the phase difference because the way that the path length is modified primarily depends on the experimental conditions, e.g. the amplitude and frequency range of the fluctuations that have to be compensated. The possible choices for this include movable mirrors mounted on piezo-electric actuators, acousto-optical modulators (AOMs) and electro-optical modulators (EOMs). The detection techniques include direct phase-measurement approaches such as Hänsch-Coillaud [103] and indirect ones such as LOCSET [104] and SPGD [105], which work by dithering the phases of the different channels. Please note that these techniques only allow for an optimization to a local maximum of the combination efficiency. In order to find the global maximum (e.g. where the OPD is not just a multiple of the carrier wavelength, but zero), additional methods have to be applied [106]. The techniques described herein can all be applied to spatial combination, but some of them, such as LOCSET or SPGD are also applicable to temporal combination schemes. The Hänsch-Coillaud approach is basically also applicable for temporal combination, but a temporal gating of the detector signal is required if more than 2 pulses are combined using the polarization combination technique [107]. Even though only stabilization techniques for the temporal domain will be investigated here, similar concepts can also be applied for the stabilization of the position and angle of the beams to be combined [108, 109].

### 5.2.1. Hänsch-Couillaud stabilization for polarization combination

The first active stabilization technique that will be reviewed in this work is based on the so-called Hänsch-Couillaud (HC) detector, as seen in figure 5.2 a). In this technique only a small fraction of the combined output beam is directed towards this detector. The HC-detector can determine the phase between orthogonally polarized beams and, therefore, its use is limited to polarization combination setups. One detector is required for every combination step of two beams. Hence, when using a cascaded setup of polarization dependent beamsplitters (see subsection 3.2.4) to combine  $N$  beams  $N - 1$  detectors

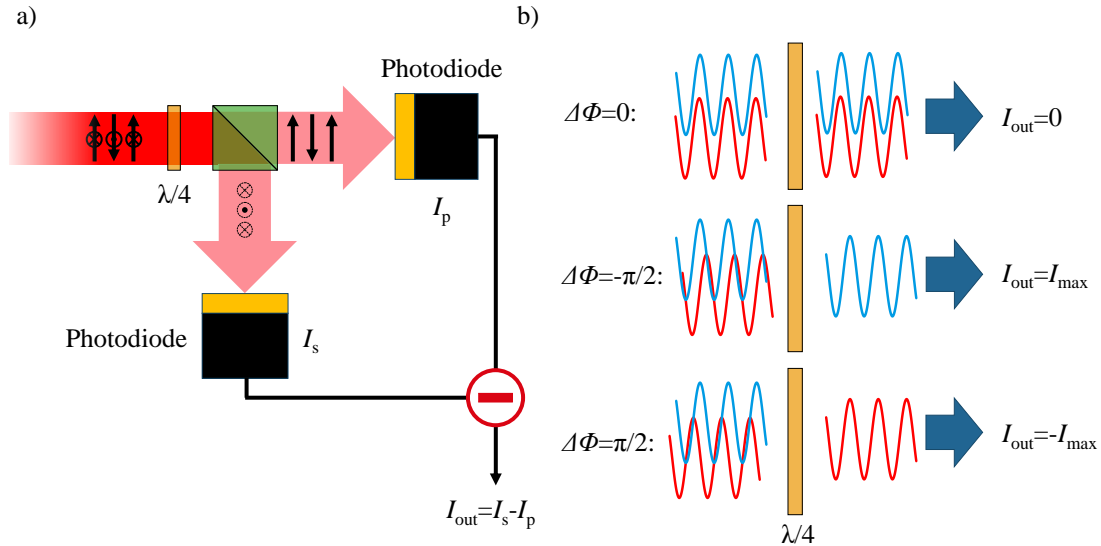


Figure 5.2.: a) Schematic setup of a Hänsch-Couillaud detector, b) Output signal depending on the relative phase between the polarization components (red and blue) of the incident beam.

are necessary. The detector itself comprises a  $\lambda/4$  waveplate, a polarization dependent beamsplitter and one photodiode for each of the two output ports of the beamsplitter. The axis of the waveplate is rotated by  $45^\circ$  relative to the polarization axes of the beamsplitter. The transmitted light is then split up according to the two polarization directions at the beamsplitter before reaching the photodiodes. An electronic device subtracts both signals from each other to generate the detection signal. To obtain the value of the detector signal as a function of the phase difference of the incident beams, it is possible to derive an analytical expression. However, just by looking at the result for certain fixed phase values it is possible to understand the operating principle. Some examples are given in figure 5.2 b). If two orthogonally polarized beams of equal power are assumed that are completely in phase, then the combined beam will also be linearly polarized, but with a polarization angle inclined by  $45^\circ$ . Therefore, since the polarization vector points in the same direction as one of the axis of the waveplate, the beam behind it will still be linearly polarized. The beamsplitter then splits it in two components with equal power, which results in a detection signal of zero. Please note that the temporal profile of the pulses and the temporal gaps between subsequent pulses have been neglected here. It will be assumed that either the photodiodes or an additional low-pass filter creates a time-averaged signal. On the other hand, if the initial phase difference is either  $\Delta\Phi = \pi/2$  or  $\Delta\Phi = -\pi/2$ , the incident light will

be circularly polarized and converted into linearly polarized light by the waveplate in either the s- or the p- polarization directions. Therefore, all power will end up at only one of the photodiodes, resulting in a positive or a negative detection signal with the highest absolute value. For all phase differences inbetween the polarization state can be considered as a superposition of the described cases and the value of the detection signal will be somewhere inbetween those mentioned above. The precise value of this signal can be calculated analytically by employing the Jones formalism with the following matrices for the waveplate and the two output ports of the splitter :

$$J_{\lambda/4} = \begin{pmatrix} i + 1 & -i + 1 \\ -i + 1 & i + 1 \end{pmatrix}, J_{\text{splitter}_s} = \begin{pmatrix} 1 & 0 \\ 0 & 0 \end{pmatrix}, J_{\text{splitter}_p} = \begin{pmatrix} 0 & 0 \\ 0 & 1 \end{pmatrix} \quad (5.1)$$

As previously mentioned, we will define an electric field vector averaged across the temporal pulse profile for both beams and add a phase difference  $\Delta\Phi = \alpha_1$  to the p-component, thus, it is possible to finally calculate the intensities  $I_s$  and  $I_p$  at the photodiodes:

$$\vec{E} = \begin{pmatrix} E_0 \\ E_1 e^{i\alpha_1} \end{pmatrix}, I_s \sim |J_{\text{splitter}_s} J_{\lambda/4} \vec{E}|^2, I_p \sim |J_{\text{splitter}_p} J_{\lambda/4} \vec{E}|^2 \quad (5.2)$$

The detection signal can then be calculated as  $I_{\text{out}} = I_s - I_p \sim 2\sin(\alpha_1) \Re(E_0^* E_1)$ . So the measured signal is a sine function of the phase difference having a zero value for  $\alpha_1 = 0$ , in accordance to the considerations above. Due to the sign change of the function at this zero point, this output can be used as an error signal (might have to be negated first) to correct the path length in the corresponding channel. Additionally, by measuring the maximum and minimum value of this signal, the phase between the beams can be directly calculated in the region from  $-\pi/2$  to  $\pi/2$ . In case of the previously mentioned failure of one of the channels, the correct error signal of zero is measured.

The advantage of the HC stabilization technique is that these measurements do not have any dynamic effect on the system (only a static small power loss for the detector signal), i.e. they do not introduce any additional noise to the system. Also, intensity fluctuations do not change the point of zero crossing of the signal, allowing for stable operation even in noisy systems. However, as previously mentioned, a single HC-detector can only be used for two channels, so the number of detectors grows linearly with the number of channels.

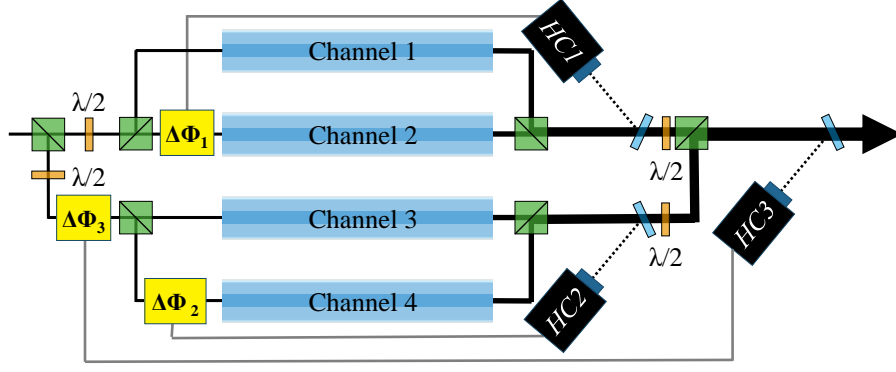


Figure 5.3.: Schematic setup consisting of four parallel channels with cascaded splitting and combination with 1:2 beamsplitters. HC detectors are added at the appropriate points that control the corresponding path-length shifters.

### Application to multichannel systems

When a cascaded setup of 1:2 beamsplitters is employed to combine  $N$  beams, behind each one of these elements, a fraction of the power has to be directed to a HC detector. The calculated error signal will be then fed back to a corresponding path-length shifter to adjust the path-length difference between the two beams at this point. The issue that has to be investigated is how such systems respond to perturbations in one of the channels, i.e. what amount of cross-talk exists between the different detectors and path-length shifters. In figure 5.3, together with a schematic setup comprising four channels, a cascaded splitting and combination scheme together with the HC detectors and path-length shifters is shown. As can be seen, a path-length change in the top channel (channel 1) will not impact the signal received at the bottom HC detector 2 (for channel 3 and 4), but it will affect HC detector 1 behind the combination element of the two upper channels 1 and 2. Additionally, the impact of such a path-length change on the last detector (detector 3) is of major interest. If a zero phase for the first channel is assumed and phases  $\alpha_1, \alpha_2, \alpha_3$  for the other ones in combination with equal field amplitudes  $E_0$ , the two electric fields after the first combination steps (behind the waveplates) can be calculated to be:

$$\vec{E}_{\text{comb}_1} = \frac{E_0}{\sqrt{2}} \begin{pmatrix} 1 + \exp[i\alpha_1] \\ 0 \end{pmatrix}, \quad \vec{E}_{\text{comb}_2} = \frac{E_0}{\sqrt{2}} \begin{pmatrix} 0 \\ \exp[i\alpha_2] + \exp[i\alpha_3] \end{pmatrix} \quad (5.3)$$

As previously stated, additional phases due to the propagation through the combination elements and free space segments are ignored. The electric field in front of the HC

detector can then be calculated:

$$\vec{E}_{\text{comb}} = E_0 \left( \begin{array}{c} \sqrt{1 + \cos(\alpha_1)} \exp \left[ i \frac{\alpha_1}{2} \right] \\ \sqrt{1 + \cos(\alpha_3 - \alpha_2)} \exp \left[ i \frac{\alpha_2 + \alpha_3}{2} \right] \end{array} \right) \quad (5.4)$$

By using equations 5.2, the final detector signal  $I_{\text{out}} = I_s - I_p$  results in:

$$I_{\text{out}} \sim 2 \sin(\alpha_1) \Re(E_0^* E_0) \sqrt{1 + \cos(\alpha_1)} \sqrt{1 + \cos(\alpha_3 - \alpha_2)} \sin \left( \frac{\alpha_2 + \alpha_3}{2} - \frac{\alpha_1}{2} \right) \quad (5.5)$$

It can be deduced from this last equation that the signal is proportional to the sine function of the phase difference between  $\vec{E}_{\text{comb}_1}$  and  $\vec{E}_{\text{comb}_2}$  and, therefore, it results in a correct error signal for the corresponding path-length shifter. The pre-factors also depend on the phases of the channels, but they only reduce the amplitude of the signal and do not change its value of zero crossing. Therefore, if a phase error  $\alpha_1$  is assumed, the cascaded stabilization system will be able to correctly handle it. The first HC detector will be able to see the complete phase difference with its neighboring channel and pass the error signal to the correct path-length shifter. Even though this phase error is also seen by the next detector its impact is reduced by a factor of two (equation 5.5), which is the correct value to optimize for the best combination efficiency for this specific combination step. Hence, the Hänsch-Couillaud technique can be employed in multichannel systems and will be able to reduce all phase differences to zero. Again, phase differences that are a multiple of  $2\pi$  have been ignored in this discussion.

### 5.2.2. LOCSET

A well-known active-stabilization technique that works with intensity beamsplitters as well as with polarization beam splitters (with an additional polarizer at the end) is the so-called self-synchronous (or self-referenced) locking of optical coherence by single-detector electronic-frequency tagging technology, better known by the abbreviation LOCSET [104]. In general, LOCSET is a multichannel implementation of the Pound-Drever-Hall technique [110] used to phase-lock oscillators to a reference cavity. In this technique, each channel (self-synchronous) or each channel  $j$  but one (self-referenced) are phase modulated with a unique frequency  $\omega_j$ , e.g. by the path-length shifters located in the respective channel:

$$\Delta\Phi_j = M_j \cos(\omega_j t) \quad (5.6)$$



This phase modulation has a certain impact on the combination efficiency. It can be calculated with the formula  $\eta_{comb} = 1 - \sigma_\phi^2$  [100], with  $\sigma_\phi^2$  being the RMS parameter variation of the applied phase modulations  $\Delta\Phi_j$ . For a two channel system with one phase modulated channel this results in  $\eta_{comb} = 1 - M^2/8$  and for a larger number of channels, the value can be calculated accordingly. Additionally, the modulation frequency has to be below the repetition rate of the system. By measuring the output power of the system with a photodiode and by multiplying the signal with the channel specific frequency, the signal can be demodulated. This is followed by a low-pass filter, which bandwidth has to be chosen accordingly to filter out the modulation frequency. For the self-referenced case the output signal is a sine function of the phase error difference to the non-modulated channel. As for the Hänsch-Couillaud system this signal can be used as an error signal to control the path-length shifters.

Besides the compatibility with intensity beamsplitters, only a single detector is required, resulting in a compact setup that is theoretically scalable to a very large number of channels. However, a unique modulation frequency has to be chosen for every channel and the stabilization bandwidth for each channel is limited by the frequency distance to the next channels. Hence, the required modulation frequencies of the path-length shifters grow with the number of channels and piezo-based mirrors might not be able to support it. Therefore, a second phase shifter for high frequencies might have to be added to each channel. Another issue is the cross-talk between the error signals if the modulation frequency in one channel is an odd multiple of another one [104]. Additionally, one has to find a compromise between a well-defined error signal (the signal-to-noise ratio for channel  $j$  is proportional to  $J_1(M_j)^2$  [104] for systems with a large number of channels) and the previously mentioned reduction of the combination efficiency due to the applied phase modulation.

In summary, LOCSET provides a way to realize a compact stabilization for a large number of channels and is compatible with all combination techniques, but it is also more difficult to setup than the Hänsch-Couillaud stabilization. The same conclusion is also valid for the SPGD (stochastic parallel gradient descent) technique, which works by applying random phase dithers to the channels and measuring the change of the output power. This comparison step results in a more complex algorithm and requires sophisticated digital control electronics. Due to the easier implementation, LOCSET has been employed in some of the experiments where a single detector stabilization system is required.

# 6. Experimental demonstration of coherent combination

In this chapter, some of the experiments of laser systems based on spatial coherent combination of ultrashort pulses will be presented that have been conducted in the frame of this thesis. First, a few of the previously demonstrated experimental results in this field will be recapitulated. Then the results for a four channel fiber CPA system will be presented: first optimized for high average power and then for high peak powers. Both experiments have set new performance records in the parameter field of average power, pulse energy and peak power. This is followed by the description of a system based on bulk amplifiers that demonstrates that coherent combination is not limited to fiber-based sources. Additionally, a proof-of-principle experiment related to the combination of spectrally broadened pulses for nonlinear compression will be shown. Finally, the integration of multiple amplification channels into a single fiber will be discussed in combination with a compact  $1:N$  beamsplitter design.

## 6.1. State of the art

Spatial coherent combination of ultrashort pulses is a relatively new concept, with the first experimental descriptions appearing shortly before this thesis. Moreover, the number of experimental demonstrations since then has been limited. The first publications in this field dates back to 2010, when the combination of two fiber amplifiers in a Mach-Zehnder-type interferometer was demonstrated [73, 74], among others by the author of this thesis. These were systems with limited average powers of a few Watts at maximum (0.5 W and 4.3 W, respectively) in combination with high repetition rates and, therefore, low pulse energies (below 1  $\mu$ J). Crucially, different stabilization systems such as Hänsch-Couillaud and LOCSET were employed and found to be compatible with the combination scheme. Later on, a first system incorporating a higher channel count of

four amplifiers was shown, also using the LOCSET scheme [111]. All of these systems were proof-of-principle demonstrations of the technology, without demonstrating the capability to provide new average-power, pulse-energy or peak-power record values. In 2011, coherent combination in conjunction with the combination of two PCF amplifiers with very large core sizes above  $70\ \mu\text{m}$  was realized. Here, sub-ps pulses with average powers of 88 W and pulse energies of 0.5 mJ could be realized [112], already close to the single-channel record value of 1 mJ at that time [14]. Additionally, a high system efficiency of 90% was achieved. Moreover, a residual path-length fluctuation of less than  $\lambda/70$  was measured, resulting in a coefficient-of-variation of the average power (defined as the root-mean-square of the average power fluctuations over the mean value of the average power) of just 0.2%. In the first experiment that was part of my work for this thesis, with a state-of-the-art front-end system similar to that described in the next section, combined and compressed 470 fs pulses with an energy of 3 mJ were achieved at a moderate average power of 30 W [113]. At that time this was the highest pulse-energy obtained from a femtosecond fiber laser system, and, to the best of my knowledge, it was the first time that a fiber laser system based on coherent combination could set an absolute record value. Later on, I could demonstrate an average power of 215 W with two large-pitch fibers. I will refrain here from a more detailed description of these experiments, in order to focus the discussion on more advanced systems with a larger channel count in the next sections. Another related application of coherent combination for a different amplifier architecture was the creation of pulses with relativistic intensities by combination of two high pulse energy OPAs [114].

## 6.2. Setup of the front-end system

While the main amplification stage with multiple parallel fibers changed for different experiments, the subsystem in front of it stayed mostly constant. A schematic view of the front-end system is shown in figure 6.1. The first element is a femtosecond mode-locked oscillator. For some of the earlier experiments, a 40 MHz commercial solid-state laser system with an average output power of about 150 mW was used, emitting 300 fs transform-limited pulses. This system was replaced later with a 62 MHz, 1 W oscillator emitting very broadband 60 fs pulses. This system is also able to stabilize the CE-phase, but this option was not used during the experiments. The stretcher and compressor of the system only support a fraction of the available bandwidth and in combination with the limited gain bandwidth of the amplifiers this results in output pulses that will be

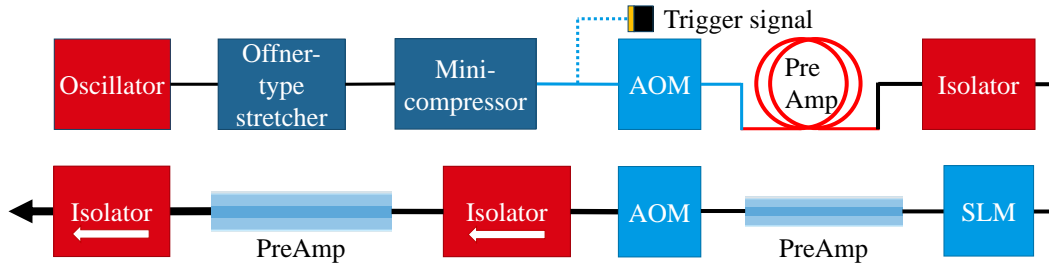


Figure 6.1.: Schematic setup of the front-end system consisting of the oscillator, a grating stretcher, multiple acousto-optical modulators (AOM), a spatial-light modulator (SLM) and three pre-amplifiers. Black lines denote free-space propagation sections between the components, and blue lines represent propagation in fibers.

considerably longer than the initial pulse duration. The stretcher is based on an Offner-type design [115] with a 35 cm wide 1740 lines/mm grating with a diffraction efficiency of about 90%. One horizontal and one vertical optical roof prism lead to two passes through the stretcher, corresponding to eight passes on the grating. For the first oscillator, the curved mirror parameters were chosen to support a bandwidth of 7.5 nm, while for the later one this value was increased to 22 nm. In both cases, the time difference between the shortest and longest passing wavelength is in total 4.2 ns. Hence, the stretcher is able to increase the pulse duration of the incoming femtosecond pulses by about four order of magnitudes. The stretcher is followed by a small (mini-) compressor that is used to slightly change the stretched pulse duration in order to optimize the pulse duration after compression. By using a motorized stage the adjustment can be done while the system is operating (even at maximum power levels) without touching the compressor itself.

After passing through it, the pulses are coupled into a standard 6  $\mu\text{m}$  passive fiber, where a 90:10 splitter directs a fraction of the power to a photodiode, which acts as a trigger signal for the AOMs in the system. The remaining power then passes through a fiber-coupled AOM that reduces the repetition rate to a value of around 2 MHz (depending on the configuration). To compensate the loss of average power associated with the reduction of the repetition rate, the AOM is followed by a 1 m long fiber amplifier to increase the average power to a level of 300 mW. The previously mentioned splitter, AOM and amplifier are all spliced together to form a stable monolithic setup. The output beam then continues propagating in free-space where it goes through an isolator to protect the system from back-reflections originating from the subsequent system components. A spatial-light-modulator (SLM) with 128 horizontally placed pixels is incorporated in a

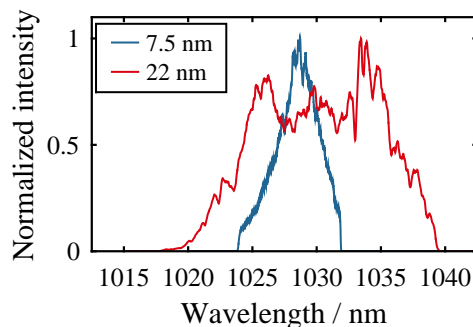


Figure 6.2.: Spectra of the front-end system after the last pre-amplifier for both, the narrow-bandwidth (blue) and the broad-bandwidth configuration (red).

zero-phase grating stretcher and is employed as a phase shaper. It is connected via a PC to a diagnostics setup at the end of the laser system (described later on) to form the “multiphoton intrapulse interference phase scan” (MIIPS) system [46]. About 50% of the power is lost due to the pass through the SLM. This phase shaper is followed by the second pre-amplifier, a 80 cm long large-pitch fiber with an MFD of  $49\ \mu\text{m}$ , pumped by a 30 W fiber-coupled pump diode. This amplifier delivers an output an average power of 1.5 W. A second (free-space) AOM is employed to reduce the repetition rate to the final desired value. Both AOMs in the system are synchronized via electronic pulse-pickers with adjustable window delays and durations to the previously mentioned trigger signal. Finally, a second pre-amplifier based on a 80 cm long large-pitch fiber (LPF) with an MFD of  $59\ \mu\text{m}$  or  $85\ \mu\text{m}$ , depending on the experiment, ends the front-end system. For the high-energy experiments the previously used small-core LPF was replaced by the large-core one to provide enough pulse energy to seed the main amplification stage without causing strong nonlinearities. In total, the front-end system can operate from repetition rates of a few-tens of kHz up to the MHz range and it can provide up to 50 W of average power. However, just a few Watts of average power were sufficient for all the following experiments. In figure 6.2 the spectra of the front-end system are shown for both configurations discussed above.

### 6.3. Combination of high-performance fiber amplifiers

In this section, the spatial coherent combination of four LPF amplifiers will be demonstrated. The amplifiers are incorporated in a cascaded setup of 1:2 beamsplitters (subsec-

tion 3.2.4) with a multichannel Hänsch-Coillaud stabilization system (subsection 5.2.1) to form the main amplification stage. The first experiment will focus on achieving high average powers [116], while the second one will focus on generating high pulse energies and peak powers [117]. The system design, results and challenges will be discussed in the following.

### 6.3.1. High-average-power system

The 40 MHz oscillator in combination with the 7.5 nm bandwidth stretcher is employed for the high-average-power experiments. To form the compressor, the stretcher grating is used in combination with a second grating with the same grating parameter. This second grating is used as the first grating in the compressor and can, therefore, be considerably smaller than the other one with 4 cm width. It has been manufactured with the electron-beam process that results in a diffraction efficiency very close to 100%. A vertical roof prism is employed to achieve a double pass through the compressor. Due to the comparably low signal bandwidth and the resulting low angular dispersion, a long propagation length between the two gratings is required to compress the pulses. In order to keep the footprint of the unit compact, a horizontal roof prism is inserted between the two gratings to fold the propagation path. In total, the compressor unit provides a transmission efficiency of 80%.

The basic scheme of the main amplification stage is similar to that shown in figure 5.3. A cascaded setup of three polarization-dependent beamsplitter cubes (PBCs) is used to split the beam coming from the front-end into four channels. A double-pass delay line is attached to each of the cubes consisting of a  $\lambda/4$  waveplate and a piezo-mounted mirror. The piezo has a maximum range of 40  $\mu\text{m}$  and is mounted on a manual translation stage. This translation stage is used to coarsely match the path lengths of the channels with an accuracy of a few wavelengths, while the piezo compensates the fluctuations of the OPDs during operation. The bandwidth for all the control signals for the piezos is limited to around 1 kHz in order to stay below their resonance frequency. The input beam in each channel is coupled into a 1.2 m long LPF with 59  $\mu\text{m}$  MFD. The fibers have angled endcaps on both sides to avoid back reflections and are pumped by four individual 400  $\mu\text{m}$  fiber-coupled pump diodes that can provide up to 600 W each. To couple the pump light into the 170  $\mu\text{m}$  pump cladding of the fibers, 2 inch diameter pump optics, providing the necessary imaging, are used. The output beams from the fibers are separated from the pump with dichroic mirrors and combined into a single beam

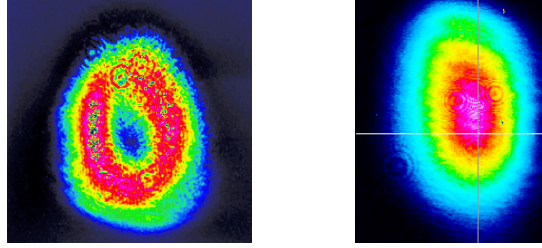


Figure 6.3.: Output beams behind the compressor at full average power for lenses provided by two different manufacturers. These lenses are used in the telescope in front of the compressor.

with three thin-film polarizers (TFPs). These polarizers have been specifically tested and selected to withstand high average powers.

Behind every combination step an antireflection-coated fused silica window directs a very small fraction (0.2%) of power to the HC detectors. The beams emitted from the channels are divergent due to the small beam diameter after the lens behind the fiber and reach a beam diameter of 3 mm behind the last TFP. In order to propagate the 10 m long path through the compressor to the output of the system, a telescope is inserted after the combination steps to properly collimate the beam. However, due to the high average powers and the long propagation paths, thermal issues on the lenses became apparent very rapidly. For this experiment, two 40 mm lenses with the best thermal properties, i.e. showing the least impact of high average powers on the output beam, have been selected. Compared to other configurations, this improves the output beam quality dramatically, as shown in figure 6.3. Still the telescope has to be readjusted for the high-average-power case. For further experiments, this telescope has been replaced by two curved mirrors with curvature radii of 300 mm and 350 mm, respectively, to form a reflective telescope.

Besides measuring the average output power behind the compressor, different additional diagnostic tools have been employed. This includes a spectrometer, an autocorrelator and the diagnostic part necessary for the MIIPS measurement. This latter part comprises a nonlinear crystal used to generate the second-harmonic signal around 515 nm wavelength and a spectrometer for this signal. This spectrometer is connected to a PC where the MIIPS software drives the SLM to optimize for a flat phase profile of the output pulses by using an iterative algorithm. Due to the limited dynamic range of the SLM, phase jumps between adjacent pixels can appear. They manifest themselves as diffraction at these spectral components, resulting in a reduction of the coupling efficiency of this spectral component into the second pre-amplifier. Therefore, they can be

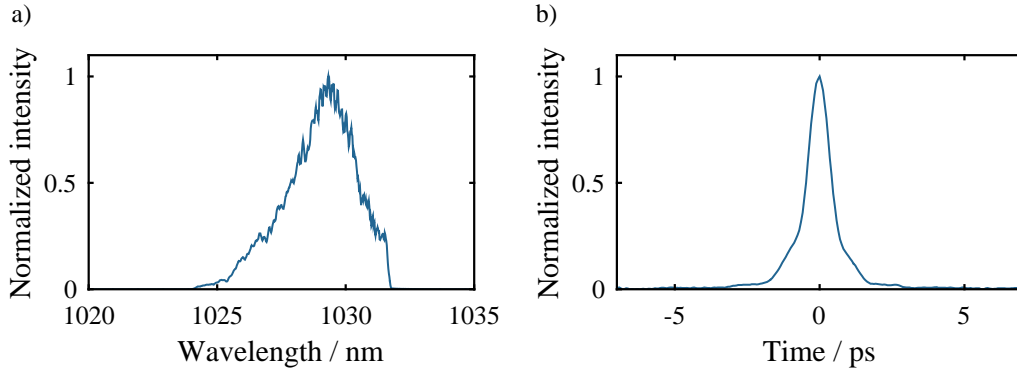


Figure 6.4.: a) Measured spectrum and b) measured autocorrelation trace of the combined pulses when running at the maximum combined average power of 530 W.

observed as dips in the spectrum. Because these dips have an effect on the nonlinear phase, a coupling between the applied phase-mask on the SLM, the spectral intensity profile of the pulse and the spectral phase profile exists. This explains why the MIIPS can flatten the spectral phase profile at the output and improve the pulse quality, but still leaves a certain residual phase, resulting in residual side-pulses. Finally, to measure the quality of the output beam, a  $M^2$  measurement device has been used.

In the experiment, the front-end system is setup to deliver a seed with an average power of 1 W for every channel and a repetition rate of 400 kHz. In order to determine the combination efficiency at the end, each channel is first operated individually and the waveplates are setup in such a way that the highest power of this specific channel is delivered at the output of the system. Compressed average powers of 133 W, 137 W, 126 W and 129 W are measured per channel. When all amplifiers are turned on and the waveplate positions have been adjusted for the maximum combined average power while the stabilization system is turned on, an average power of 530 W is measured, corresponding to a pulse energy of 1.3 mJ. The combination efficiency can simply be calculated by dividing this value through the sum of the individual output powers, resulting in a value of 94%. Taking into account the non-perfect polarization of the channel output beams, being measured at the specific ports of the TFPs, an additional loss can be determined that leads to a system efficiency of 93%. The spectral and temporal characteristics of the output are shown in figure 6.4. A FWHM bandwidth of 2.7 nm can be obtained and an autocorrelation trace with a duration of 940 fs is measured. By applying the deconvolution factor calculated from the transform-limited pulse duration and the duration of its autocorrelation trace, a pulse duration of 670 fs can be estimated in combination with a peak power of 1.8 GW. The theoretical investigations in subsection 4.2 support



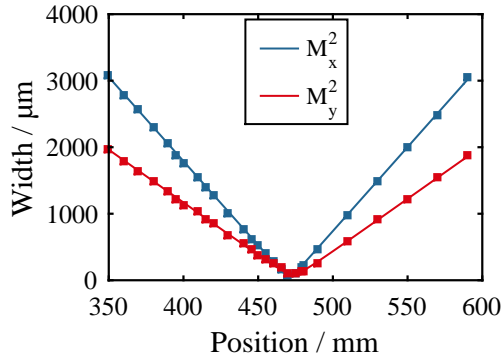


Figure 6.5.:  $M^2$  measurement of the combined beam at 530 W.

the high combination efficiency due to the low sensitivity to B-integral differences with low spectral bandwidths (the LDE differences are small due to a good match of the fiber lengths).

As previously mentioned, an  $M^2$  measurement is performed to measure the beam quality of the combined beam at the output (see figure 6.5). This measurement is also done for the first channel to have a comparison to what can be achieved with a single channel system. In the combined case a value of  $M_x^2 < 1.1$ ,  $M_y^2 < 1.2$  is achieved compared to  $M_x^2 < 1.1$ ,  $M_y^2 < 1.3$  for the single channel. Hence, the combined system delivers a near diffraction-limited beam quality that is comparable or even slightly better than what can be achieved with a single channel system. This improvement was theoretically investigated in section 4.5.

In summary, the experiment shows the viability of coherent combination for high average power femtosecond CPA systems. The output pulses and the output beam have properties that are basically equal to those of a single channel system, just with a higher performance. Therefore, this combined radiation can be used for the same kind of applications as that coming from a single channel system. Most of the problems that occurred during the experiment have been related to the handling of the output parameters and not to the combination itself. Additionally, the specific combination of pulse energy, peak power and average power has not been demonstrated with any other femtosecond fiber laser system yet and is beyond what is achievable with a single channel today.

### 6.3.2. High-peak-power system

The focus of this second experiment shifts towards achieving the highest possible pulse energy and peak power. Therefore, a number of modifications have been made to the

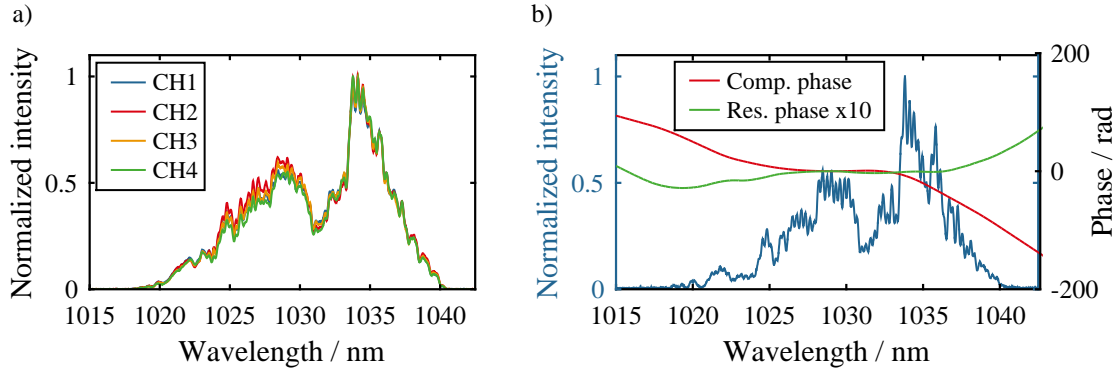


Figure 6.6.: a) Spectra of the four individual channels after compression and b) spectrum of the combined pulse with compensated (applied by the phase shaper) and residual phase (scaled by a factor of 10).

system compared to the previous experiment. In order to generate shorter pulses and increase the peak power, the oscillator, stretcher and third pre-amplifier have been changed to the later configuration described in section 6.2. Due to the higher angular dispersion of the beam for the new spectrally broader signals, a shorter propagation length is sufficient in the compressor and the horizontal roof prism can be removed. To support higher pulse energies, the 59  $\mu\text{m}$  MFD fiber amplifiers have been replaced by 85  $\mu\text{m}$  MFD fiber amplifiers, providing around two times the mode area. This reduces the B-integral by a factor of two, while increasing the stored energy by the same factor. An additional reduction of the B-integral is provided by using shorter fiber lengths between 85 cm and 95 cm. Additionally,  $\lambda/4$  waveplates are placed in front of and behind each amplifier to achieve circular polarization during propagation through the fiber. As stated in chapter 2, this further reduces the B-integral. However, due to the onset of nonlinear polarization rotation in the fiber at the highest power levels, circular polarization might only be reached at the end of the fiber and the evolution of the polarization state during propagation is unknown. Due to this, an exact determination of the B-integral is impossible. Finally, the telescope in front of the compressor has been replaced by a Galilean telescope with focal lengths of -150 mm and 200 mm. This avoids a focal spot between the lenses that might cause peak-intensity related issues, which will be discussed later. The system is operated at a repetition rate of 40 kHz and with a seed average power of 500 mW per channel, corresponding to 50  $\mu\text{J}$  pulse energy coming from the front-end. Each of the main amplifiers is set up to emit an output power of 65 W and 1.6 mJ pulse energy after compression. Due to the high inversion level in the fiber, the system is very susceptible to back reflections, which have to be avoided. The B-integral can be esti-

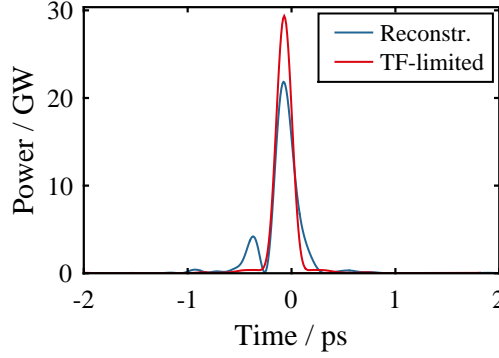


Figure 6.7.: Reconstructed temporal pulse profile (blue) and transform-limited pulse profile (red).

mated with the help of the one-dimensional rate equations [118] and all the reservations described above to be around 5 rad. The spectra of each channel running individually is shown in figure 6.6 a). As can be seen, a very good match of the spectral intensity profile is achieved, even though the amplifier is already starting to work in saturation. This can be seen by the higher amplification of the longer wavelengths due to the up-chirp of the stretcher.

Despite the high total gain of 75 dB (including about 20 dB loss in the system due to the losses in the stretcher, pulse pickers and fiber coupling), a FWHM spectral bandwidth of 10 nm could be maintained. When the output of all four amplifiers is combined, an average power of 230 W can be achieved, resulting in a pulse energy of 5.7 mJ and a peak power of 22 GW. The corresponding combined spectrum with the compensated (applied by the phase shaper) and residual phase is depicted in figure 6.6 b). It shows a similar intensity profile to the single channels but with some additional high-frequency modulations, which might be caused by phase differences between the individual pulses. Finally, the reconstructed pulse profile (in blue) and the transform-limited pulse calculated from the spectrum (in red) can be seen in figure 6.7. About 16% of the power of the 200 fs pulse is contained in a side pulse caused by the residual phase. According to this estimation 30 GW of peak power should be achievable with a transform-limited pulse. It should be noted that the residual spectral phase (enlarged by a factor of 10 in figure 6.6 b)) is very small compared to the phase compensated by the SLM. Most of this phase is not actually caused by the amplifiers, but by a mismatch between stretcher and compressor, which origin could not be determined so far. The peak power per channel can be estimated to an average value of 6.3 GW. Therefore, if the compressor had an efficiency of 100%, this would result in a value of 7.8 GW, which is close to the proposed

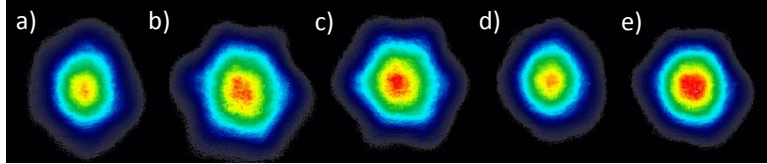


Figure 6.8.: Output beam profiles for a)-d) channel 1-4 and e) the combined beam.

theoretical 10 GW limit for a fiber laser system in this configuration (see section 2.6). Hence, this experiment demonstrates that the coherent combination of amplifiers running near their peak-power limit (or pulse energy limit if the stretched pulse duration is taken into account) is possible. In spite of this, the combination efficiency has a value of 89%, which is only slightly lower than in the high-average-power experiment. The reason for this includes the larger differences of the fiber lengths, the lower beam quality emitted from the larger fiber cores as well as phase differences due to the nonlinear polarization rotation in the fibers. While it is not possible to calculate the impact of the last effect, the impact of the different fiber lengths can be estimated by the equations 4.7 and 4.13 from subsection 4.2. With the 10 nm FWHM bandwidth, this results in an expected drop of the combination efficiency of less than 1%. In figure 6.8, the measured output beam profiles behind the compressor are shown for every single amplifier together with that of the combined beam. Due to slightly different collimations, some differences between the intensity profiles can be observed. Still, a very clean combined intensity profile is achieved. Again, in order to include the spatial phase into the assessment of the beam quality,  $M^2$  values are measured. The following table lists the result for every channel and for the combined beam:

Channel	$M_x^2$	$M_y^2$
1	1.31	1.27
2	1.36	1.27
3	1.34	1.29
4	1.34	1.29
Combined	1.31	1.23

As in the previous experiment, a small cleaning effect due to coherent combination can be observed, resulting in a slightly better beam quality of the combined beam.

During the experiment, peak-intensity effects taking place while propagating in air caused the most challenging problem. According to [119], air breakdown starts to occur for intensities approaching  $1 \cdot 10^{11} \frac{\text{W}}{\text{cm}^2}$  for the wavelengths used in this experiment. This

value is reached when employing the reflective telescope, even for the long stretched pulse duration of 2 ns. Taking into account a focal length of 175 mm, an uncompressed combined pulse energy of 7.1 mJ and an incident beam size of 3.5 mm, the intensity in the focal spot will be  $1.05 \cdot 10^{11} \frac{\text{W}}{\text{cm}^2}$ . Due to the following long propagation length through the compressor, this has a major detrimental impact on the output beam. A value above this threshold is also reached for the pulses behind the compressor when maintaining a beam size of 3 mm from the last experiment ( $3.1 \cdot 10^{11} \frac{\text{W}}{\text{cm}^2}$ ). These effects are mitigated by employing the Galilean telescope without a focal spot and by increasing the output beam size to 5 mm. Even though the resulting peak intensity after compression is still slightly above the threshold, due to the short propagation length from the compressor to the diagnostic components, no detrimental impact on the output beam is observed. In summary, the presented laser system has achieved a higher peak power than any previously reported femtosecond fiber laser system. Even at these parameters, a high combination efficiency and beam quality has been maintained.

### 6.3.3. Applications

Even though the focus of this thesis lies on coherently combined laser systems, in the following some experimental results for applications using these laser systems are mentioned here. Apart from the characterization of these systems, the applications will prove that laser systems based on this technology are actually a viable alternative for real world applications. One of the most interesting applications for high-power fiber-CPA systems is the so-called high-harmonic-generation (HHG) process [10, 11], where the laser beam is partially converted to coherent radiation in the XUV wavelength region. For this process very short laser pulses are often preferred [120]. One technique to shorten the output pulses from laser systems is nonlinear pulse compression (see section 4.6). In the experiments presented herein, gas-filled hollow-core fibers are employed as the broadening medium, which require a very good beam quality of the incoming beam to achieve a good coupling efficiency. Both configurations of the laser system demonstrated above have been employed as the driver for nonlinear compression.

In a first experiment, the system is operated at 280 W average power (due to thermal limitations of the compression setup) and 1.1 mJ pulse energy [121]. The system uses the broadband stretcher and also a 15 nm bandwidth fiber oscillator that results in a pulse duration of 340 fs. The pulses are first spectrally broadened in a 1 m long hollow-core fiber with a core diameter of 250  $\mu\text{m}$ . The fiber is placed on a V-groove in a water-cooled

tube to dissipate the heat caused by the comparably high propagation losses resulting from the grazing-incident guiding mechanism. The tube is filled with 1.9 bar of krypton as the nonlinear medium for spectral broadening, providing a 10 dB bandwidth of 90 nm at the output. With 14 bounces on chirped mirrors, a total group delay dispersion of  $-1400 \text{ fs}^2$  is applied for compression. With this setup, the pulse duration can be reduced from the input value of 340 fs to 26 fs. With a total efficiency of 48%, in which the propagation efficiency through the hollow-core fiber is 56%, this results in 135 W average power and 540  $\mu\text{J}$  pulse energy with a peak power of 11 GW. This setup allowed for the generation of an unprecedented XUV flux of 143  $\mu\text{W}$  ( $3 \cdot 10^{13} \frac{\text{photons}}{\text{s}}$ ) at 30 nm via HHG [122].

In a second experiment, the high peak-power configuration of the laser system in combination with a second compression stage is employed [123]. The first hollow-core fiber with a length of 1 m and a core diameter of 250  $\mu\text{m}$  is filled with 2 bar of argon. With the same group delay dispersion as in the previous setup, a pulse duration of 30 fs is achieved after this first compression stage. In the second stage, a 0.5 m hollow-core fiber is employed, filled with 6 bar of neon, chosen due to its higher ionisation potential compared to argon. With a pair of ultra-broadband chirped mirrors providing a total group delay dispersion of  $-200 \text{ fs}^2$  in combination with a 5.3 mm thick bulk fused-silica window, the pulse can be compressed to sub-8 fs. With a repetition rate of 150 kHz, the achieved 53 W average power correspond to 353  $\mu\text{J}$  of pulse energy. The total efficiency from the output of the CPA system to the output after the two-stage compression is 35%. resulting 25 GW peak power pulses. With them coherent XUV radiation in the water window wavelength region (below 4.2 nm) can be generated.

In summary, these results show that the pulses emitted from coherently combined fiber laser systems can be shortened successfully with nonlinear pulse compression. The resulting laser systems are perfect drivers for HHG experiments at high average powers and even allow generating light with very short wavelengths in the water window wavelength region.

## 6.4. Combination of bulk amplifiers

Even though fiber based sources are the perfect amplifier architecture for coherent combination due to their single pass setup and nearly power-independent beam profile, other architectures can be used as well. To demonstrate this have been coherently combined in the frame of this thesis [124]. These amplifiers are commercially available single crystal

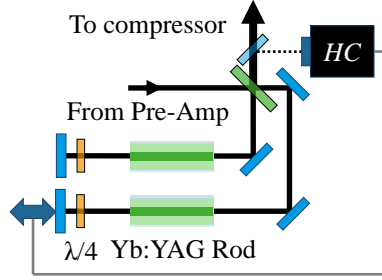


Figure 6.9.: Schematic setup of the main amplification stage consisting of two Yb:YAG rod amplifiers operating in a double-pass configuration. A TFP is employed for splitting and combination, while a HC detector is used to generate an error signal for the piezo-mounted mirror.

Yb:YAG rods with a length of 4 cm and a diameter of 1 mm each, embedded in a water-cooled copper block [125]. While the signal is not guided, the pump light is partially guided in the rear part of the rod for a better pump-to-signal conversion efficiency. In this experiment the two amplifiers are placed in the arms of a Michelson-Interferometer-type setup, which is depicted in figure 6.9. This allows employing just one common splitting and combination element, which is realized by a TFP. Additionally, the amplifiers are used in a double-pass configuration, which is preferable considering the relatively low single-pass gain. In order to stabilize the interferometer, a fraction of the combined beam is directed towards a HC-detector, which controls the position of the feedback mirror in one channel. As in the previously discussed experiments, a piezo-mounted mirror is employed to compensate for path-length fluctuations, while the piezo is mounted on a manual translation stage for the initial path length matching with a coarse precision of a few wavelengths. Compared to the previously used fused-silica fibers, the doping concentration of these bulk amplifiers is around four times larger ( $1.2 \cdot 10^{26} \frac{\text{ions}}{\text{m}^3}$  vs.  $3 \cdot 10^{25} \frac{\text{ions}}{\text{m}^3}$ ). However, the crystals are also at least 20 times shorter. Therefore, a significantly higher seed pulse energy and a higher inversion level are required to achieve an acceptable output power (the small signal gain is limited to about 23). The latter point requires, additionally, a good spatial overlap of the signal and pump beams. Therefore, two high-brightness 105  $\mu\text{m}$ -fiber-coupled pump diodes at 940 nm central wavelength are used, providing up to 65 W of average power.

A different front-end system has been employed for this experiment, however the setup is comparable to the narrow-bandwidth configuration of the previously described front-end. A seed power of up to 3 W is applied to each amplifier, limited at lower repetition rates by a pulse energy of 300  $\mu\text{J}$  per channel, which is the maximum value achievable

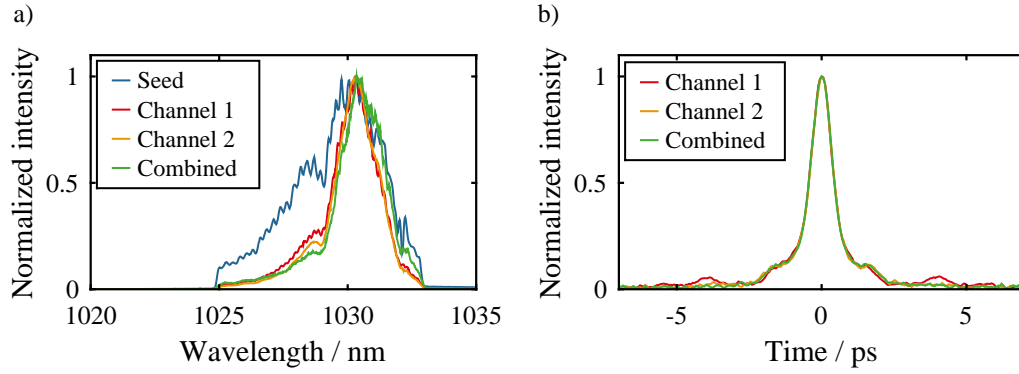


Figure 6.10.: a) Spectra of the seed pulses (blue), the pulses from the two channels (red and orange) and the combined pulse (green), b) autocorrelation trace of the combined pulse and the single pulses.

with the pre-amplifier. The achievable average power delivered by the amplifiers is limited by the available pump power and the onset of thermal lensing. Additionally, the pulse energy is limited to about 2.3 mJ by the damage threshold of the coatings of the rods, which is necessary to avoid higher losses at the end facets due to the higher refractive index of YAG (1.81 at 1030 nm [21]) compared to fused silica (1.45 [99]). In general, the self focusing limit in YAG is about three times smaller than in fused silica, which is caused by the three times larger nonlinear refractive index [126]. To achieve this pulse energy the repetition rate has to be reduced to values as low as 6 kHz. In figure 6.10 a), the spectra of the seed (blue), of the individual channels (red and orange) and the combined beam (green) are shown. As can be seen, the output pulses show an excellent match. However, the narrow gain bandwidth of Yb:YAG [127] results in spectral gain-narrowing of these pulses compared to the seed spectrum. With these parameters, the system emits 3 mJ combined and compressed pulses with a pulse duration of 695 fs (derived from the spectrum and residual phase; corresponding autocorrelation traces in figure 6.10 b)) and a peak power of 3.7 GW. The compressed average power is 18 W and even at these comparably low-average-power levels, some of the components had to be readjusted to compensate for thermal lensing in the amplifiers. The determined combination efficiency is 94% and the beam quality is characterized by an  $M^2 < 1.2$ . This high combination efficiency demonstrates that coherent combination is not limited to fiber amplifiers, but can even be applied to other types of optical amplifiers without any guiding mechanisms for the signal beam.



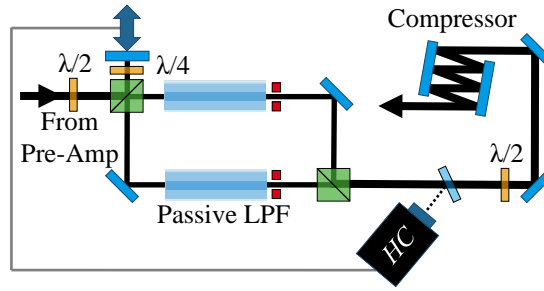


Figure 6.11.: Schematic setup of the coherent combination of two solid-core fibers for spectral broadening, stabilized with a HC system. The combined pulses are compressed in a chirped-mirror compressor.

## 6.5. Combination of solid-core fibers for nonlinear pulse compression

Besides the power scaling of amplifiers, coherent combination can also be used to increase the performance of nonlinear pulse compression stages. In section 4.6, this process was already investigated theoretically. In the following, some results from a proof-of-principle experiment, the combination of two passive LPFs for spectral broadening in combination with a single chirped-mirror compressor [128], will be presented.

### 6.5.1. Setup and results

The fiber CPA system discussed in section 6.3 is used as the source for this experiment, delivering 340 fs pulses at a repetition rate of 2.1 MHz. Two passive solid-core LPFs with an MFD of  $75 \mu\text{m}$  are employed for the spectral broadening and are incorporated into a Mach-Zehnde interferometric setup, as can be seen in figure 6.11. The fibers have a length of 10.3 cm and 10.8 cm, respectively. The required adjustable delay line is attached to the first PBC. As in the case of the combination of fiber amplifier this delay line is realized with a double-pass configuration consisting of a  $\lambda/4$  waveplate and a piezo-mounted mirror, with the piezo again placed on a manual translation stage. After splitting the incident beam into two beams, the pulses are then spectrally broadened in their respective fibers and, finally, recombined with a second PBC. The fibers have the same structure as the previously described LPFs used in amplifiers, but their cores are not Ytterbium doped. Therefore, they also possess an air-clad for the pump light, which means that signal light that is not correctly coupled into the core will still be guided by the fiber cladding. This can have a detrimental effect on the combination

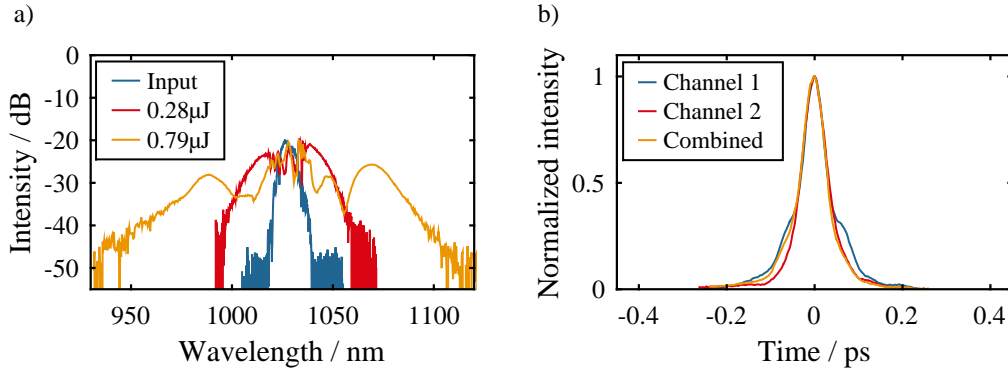


Figure 6.12.: a) Spectra of the input (blue) and broadened pulses (red and orange) for two different pulse energies (measured behind the apertures), b) Autocorrelation traces at the highest pulse energy for both channels (blue and red) and the combined pulse (orange) after compression.

process because light in this multimode cladding does not combine coherently. In order to reduce this effect, apertures are placed behind the fibers to filter out as much of this cladding light as possible, without impacting the output from the signal cores. The standard configuration for polarization combination with an HC detector connected to the piezo is also employed here. A  $\lambda/2$  waveplate is used to rotate the polarization of the combined beam to p-polarization, which is required for the subsequent compression using two chirped-mirrors. These chirped-mirrors provide a dispersion of  $-350 \text{ fs}^2$  per bounce, which results for 8 bounces in a total compensated dispersion of  $-5600 \text{ fs}^2$ . The efficiency of this compressor is measured to be 92%.

The pulse energies per channel behind the apertures are changed between  $0.28 \mu\text{J}$  and  $0.78 \mu\text{J}$ , which corresponds to  $0.71 \mu\text{J}$  to  $1.95 \mu\text{J}$  in front of each fiber. This leads to a significant broadening of the spectrum, as shown in figure 6.12 a), from the few nanometers of the input pulse to 100 nm at the highest pulse energy (10 dB bandwidth). To calculate the combination efficiency, a polarization analyzer cube is placed in front of the compressor and the maximum and minimum power are measured behind it. This results in values in the range between 75% and 80%, independently from the broadening. The reason for this considerably low efficiency is the remaining light in the cladding that is not filtered out by the apertures. After compression, pulse energies of up to  $1.1 \mu\text{J}$  can be achieved. The autocorrelation traces at the highest energy level are depicted in figure 6.12 b). The combined autocorrelation trace has a duration of 39 fs, which corresponds to a sub-30 fs pulse duration if a Gaussian temporal profile is assumed. The figure also shows a slight difference between the traces for channel 1 and channel 2.

However, the impact of this issue on the combination process is small, as confirmed by the virtually constant combination efficiency.

Taking the pulse duration and the pulse energy into account, the resulting peak power of 5 MW is beyond the self-focusing limit of a single fiber, which shows that coherent combination is a way to get around physical limitations in nonlinear pulse compression. To the best of my knowledge, this is the first demonstration of this technique with spatial coherent combination. In order to further improve this efficiency, broadening fibers without a pump cladding might be employed to filter out the residual light even better. One example would be to use gas-filled hollow-core fibers as already discussed in section 4.6. This will allow to increase the performance of laser systems like the ones described in subsection 6.3.3 further once limitations of the nonlinear pulse compression stages are encountered.

## 6.6. System integration of multiple channels

In the previously described experiments, the coherent combination technique has been applied to different cases, starting from fiber amplifiers to solid-state bulk amplifiers and, finally, to passive fibers used for spectral broadening. However, all of these experiments have in common that the individual channels are constituted by the same components used for conventional single channel systems. While this eases the construction of such systems by employing already developed components, increasing the channel count might result in complex systems with a large footprint. Hence, a compact integration of multiple channels into a single module is of major interest. In this section, an amplifier design incorporating a four-channel multicore fiber, applying a compact 1: $N$  splitter design and the LOCSET stabilization system, will be demonstrated.

### 6.6.1. 1: $N$ segmented-mirror splitter

A promising way to implement a compact 1: $N$  splitter [129] was adapted during this thesis especially for the combination of the individual beams emitted by multicore fibers (see section 6.6). The basic setup for this 1:4 segmented mirror splitter (SMS) is shown in figure 6.13 a). The incoming beam propagates in a zig-zag path between the segmented mirror, shown in figure 6.13 b), and a mirror with a constant high reflectivity. The reflectivities of the front side of the segmented mirror are chosen in a way that every

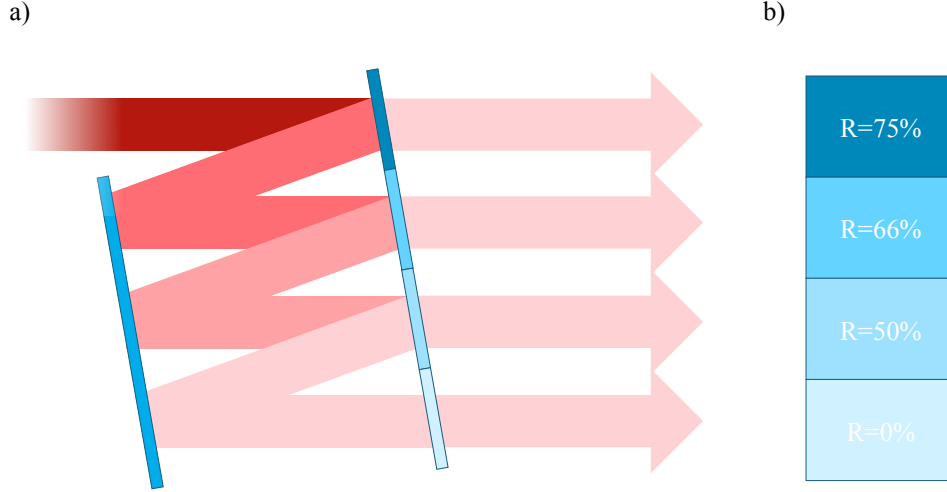


Figure 6.13.: a) Segmented mirror splitter in 1:4 configuration, b) corresponding reflectivity profile of the segmented mirror.

ejected beam has the same power. For  $N$  beams, the reflectivity of the  $j$ -th segment can be calculated as:

$$R_j = 1 - \frac{1}{N + 1 - j}$$

The backside of the element is anti-reflection coated. If the two mirrors are aligned parallel to each other, the  $N$  output beams will also be parallel. In fact, the configuration is very similar to that used for pulse compression with chirped-mirrors [130]. Additionally, instead of using a one-dimensional setup with one splitter, two of such splitters can be arranged orthogonally to each other, thus generating a 2D  $N \times M$  array of output beams. In this case, the maximum number of reflections for every beam is always below  $2 \cdot (N + M)$ . The main benefits of this SMS element are that it is nearly-diffraction-free and able to handle high average powers. The first aspect can be explained by the fact that only material dispersion in combination with a small incident angle on the material occur, resulting in a very small spatial chirp of the transmitted beams. On the other hand, the high-power capabilities come from the fact that even though the  $N$  beams are transmitted through the element when it is used as a combination element, the high-power combined beam itself is only reflected if constructive interference occurs. Therefore, the thermal demands on every segment are comparable to those composed on the coupling elements as used for cavity enhancement, i.e. the high average power beam inside the cavity is reflected and the lower power incident beam is transmitted. Here,

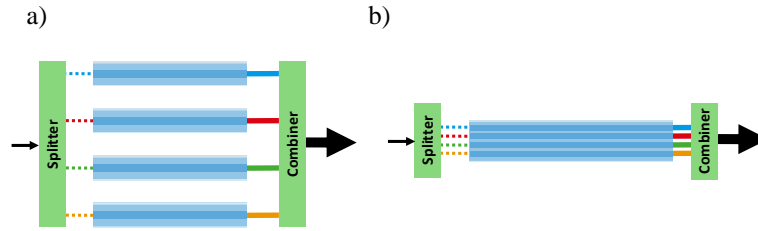


Figure 6.14.: Comparison of the schematic spatial coherent combination setup when a) using multiple parallel amplifiers, b) using the single cores of a multicore fiber.

extremely high average powers close to a Megawatt have already been demonstrated by employing substrates made of ultra-low expansion glass [131]. Hence, the application of the SMS element for the combination of beams with extreme average powers is expected to be possible. Because such a laser system will mostly operate in the CPA regime, the occurring peak powers and peak intensities at the SMS element will be low compared to the related damage thresholds of the substrates and coatings. Thus, the only limitations of this splitter will be the losses due to the multiple reflections of the combined beam at the two elements in combination with non-perfect reflectivities of the element. This is again equivalent to the issues found in enhancement cavities, where the reflectivities of the coupling mirrors and of the other high-reflectivity mirrors have to be well controlled.

### 6.6.2. Multicore fiber amplifiers

Integrating multiple signal cores into a single fiber has been thoroughly investigated for optical communication [132]. A similar idea can be employed for fiber amplifiers as well, as seen in figure 6.14 and demonstrated in proof-of-principle experiments for CW [133] and ultrashort pulses [134] in tiled-aperture configuration. In order to achieve spatially separated amplification, the different signal cores have to be optically isolated independent from each other, i.e. they should behave in the same way as multiple separate fibers. Due to the integration into one single fiber, thermal cross-talk between the cores cannot be completely avoided and might be of concern, e.g. regarding mode-instabilities. However, recently it could be demonstrated with a four-core large-mode-area PCF that the mode-instability threshold basically scales linearly with the number of cores [135]. A total average power of 536 W was achieved, pumped by a single pump source into a shared pump cladding. In fact, in the case of Ytterbium-doped double-cladding very large-mode-area fibers, the available pump sources today provide higher average pow-

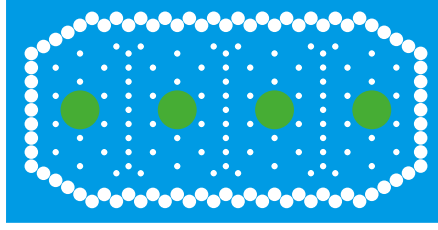


Figure 6.15.: Schematic structure of the multicore large-pitch fiber [136]. Green: Ytterbium doped areas.

ers than can be handled with a single signal core without hitting the mode instability threshold. Therefore, such a configuration allows enhancing the performance of fiber laser systems and reducing the component count due to the shared pump source. Even though in the frame of this thesis the fiber used in [135] was available for experiments, it is not actually suited for coherent combination. The reason for this is the inhomogeneous refractive-index profile of the cores, resulting in output beams with different intensity and phase profiles from each of the individual cores. Experimental investigations resulted in combination efficiencies below 40%. Hence, a new fiber was designed and produced based on the LPF design. The micro structure of the fiber is shown in figure 6.15. This fiber was produced in different sizes (LPF 20, LPF 30, LPF 40 and LPF 50). The resulting MFD per core can be estimated (for low average powers and neglecting the thermal profile) by the formula  $MFD=2\Lambda - d$ , where  $\Lambda$  is the pitch between the holes and  $d$  their diameter (with a value of  $d = 0.2\Lambda$  for these fibers).

Unfortunately, various issues impact the performance of the fibers. Due to a mismatch between the refractive index of the active material and the silica matrix [137], only the smallest fiber is usable and even this one shows an imperfect confinement of the fundamental mode in the core. Additionally, an insufficient strength of the optical barrier between the different cores leads to optical coupling between them. The effect of this coupling affects the beam quality negatively, and also reduces the achievable combination efficiency. This will be investigated in more detail in the next subsection. Still, despite all these issues, the fiber can be employed to realize a complete setup, including the splitting, combination and stabilization of the path lengths with only a moderate loss of combination efficiency.

So far, the fibers employed have their cores distributed in a single row. However, a 2D-setup of cores would also be possible. As discussed in subsection 6.6.1, splitting and combination elements for this case are easily realizable.

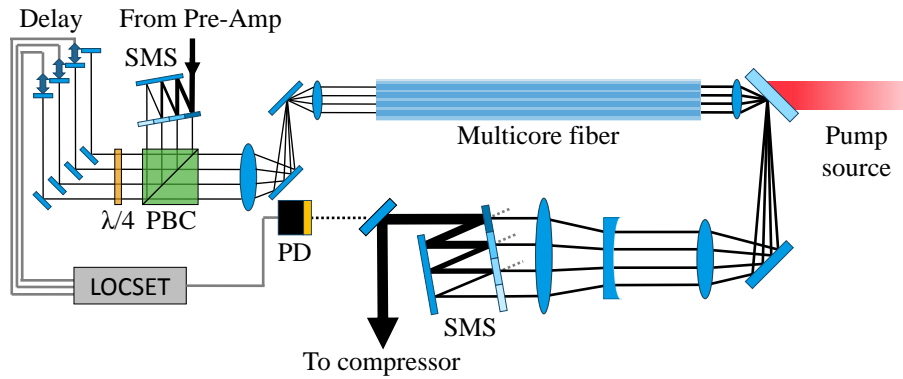


Figure 6.16.: Schematic setup of a four-core large-pitch multicore fiber with the SMS element used as a splitter and combiner. The active path length control of three of the channels is realized with a LOCSET based system.

### 6.6.3. Setup and experimental results

In figure 6.16, the schematic setup of the main amplification stage including the 1.15 m long multicore fiber is shown. It is seeded by the front-end system as applied for the first two experiments (broadband configuration). The SMS, element presented in subsection 6.6.1, is employed to split the incoming beam with a diameter of 900  $\mu\text{m}$  into four parallel channels. They are first reflected at the PBC and directed to a piezo-mounted mirror for each beam (with the exception of the mirror of the first channel, which is static). By employing a  $\lambda/4$  waveplate, a double pass can be realized to use the piezos as path-length shifters. The SMS element has a pitch of 2 mm between the different segments, leading to a similar separation between the four resulting beams. Due to the size of the piezos with the mounted mirrors being larger than 2 mm across, additional mirrors have to be employed to increase the spacing of the beams from the 2 mm to about 4 cm. Instead of this setup, which introduces additional components, it would also be possible to let the four beams pass through a magnifying telescope to increase the absolute distance between them. If a 4f-setup were employed, this would not introduce any significant errors due to divergence. However, large enough aspheric lenses for the telescope were not available at the time of the experiment. Using a standard spherical lens, on the other hand, would introduce too many aberrations on the outer beams. After going through these delay lines the four parallel beams are demagnified by a factor of 25 with a combination of a 500 mm and 20 mm lens in a 4f-configuration and imaged directly onto the end facet of the multicore fiber to be coupled into its respective cores. This factor was chosen to provide the correct beam sizes at the end facet (MFD

$\sim 36 \mu\text{m}$ ). The first beam is coupled into the right core by adjusting the two mirrors inside the telescope. Then, by changing the angles of the SMS components, the distance between the beams can be adjusted, resulting in a simultaneous coupling of all the other beams.

At the output of the fiber another 4f-setup is used to generate four parallel output beams again. In between, a dichroic mirror separates the signal light from the light of the pump source. The pump cladding of this fiber has a size of  $116 \mu\text{m} \times 269 \mu\text{m}$ . Due to the roundness of the output fibers of standard pump sources, the smaller dimension has to be considered for the pump coupling. In the experiment, a 600 W,  $200 \mu\text{m}$  fiber-coupled pump diode is used and its output beam is imaged to the required size by the same optics as employed in section 6.3, providing a demagnification factor of around 2.4. The focal length of the lens behind the fiber is around 40 mm (it is part of the pump coupling optics and cannot be changed) and with an additional 400 mm lens, a magnification factor of 10 can be achieved. Hence, the resulting beam distance is too small to use the SMS element again for combination. Instead of using a second lens with a very large focal length, resulting in a very large footprint, a second telescope with a -100 mm, 200 mm lens combination provides the right beam distances for the next SMS element. In the same way that the input beam is split into four, the four output beams can now be coherently combined back into one. The non-combined parts (gray dashed lines in figure 6.16) are reflected (and transmitted) in a direction defined by the SMS angle and caught by a beam dump.

A small leakage of the combined beam through a mirror is directed towards a photo-diode that is connected to a LOCSET system which drives the piezos to obtain a maximum combined average power. In the experiment, the modulation frequencies of the piezos are set to 2 kHz, 3 kHz and 4 kHz, respectively to generate the required phase modulations for the LOCSET scheme. As can be seen in the schematic setup, the path lengths from the input beam to the input end facet of the fiber and also from the output end facet to the combined beam are different for each channel. Hence, the 4f-requirement cannot be fulfilled for all channels at once. This means that the beam diameters at the input of the fiber will be slightly different from each other. The same holds true at the combination element due to the divergence of the beam. While the slightly different coupling efficiency into the fibers might be neglectable, the different beam diameters at the combination element will have an impact on the combination efficiency. As an estimation, a beam diameter of  $900 \mu\text{m}$  at the element will be assumed. The distance between both components of the SMS element is 5 cm, resulting in a maximum path-length



difference of  $2 \cdot 3 \cdot 5 \text{ cm} = 30 \text{ cm}$ . By calculating the propagation of the different beams, a maximum achievable combination efficiency of 98.5% can be determined. Hence, the losses due to this beam-diameter mismatch are small, but they will become more pronounced if the number of channels is increased. In this case, larger beam sizes (to reduce the divergence) and beam distances should be chosen and the SMS element has to be designed accordingly. Finally, the combined beam is sent to the previously employed grating compressor with a bandwidth of 22 nm.

As in the previous experiments, the combination efficiency will be determined as a measure to describe the quality of the combination process. In all of the previous experiments, this could be done by just operating each of the amplifier channels one-by-one and then comparing their added output power to that of the combined case (see equation 4.2). However, in the multicore fiber the amplification in each signal channel is not completely independent from the amplification in the other channels due to the shared pump cladding. Therefore, the output power of each signal channel would have to be measured individually while all signal channels are running. Due to the small distance between the beams, this is a difficult and error-prone task. Another way is to measure the reflected power of the SMS element, but this is also challenging in high-average-power operation due to space constraints. The alternative is to let the stabilization system optimize the combined output power to the maximum and minimum values and derive the combination efficiency from them. For a four channel SMS element with the stated reflectivities, the expected combination efficiency is 25% if the pulses from each channel do not overlap in time and, therefore, neither constructive nor destructive interference happens at the combination element. In this case, changing the phases of the individual channels will not alter the output power of the combined beam, resulting in  $P_{\max} = P_{\min}$ . Hence, in order to get to the expected combination efficiency, the following formula can be derived:

$$\eta_{\text{comb}} = \frac{P_{\max}}{P_{\max} + 3P_{\min}} \quad (6.1)$$

A more detailed derivation of the equation can be found in appendix B and it can also be confirmed experimentally at lower average-power levels by measuring  $P_{\max}$  and  $P_{\min}$  and comparing them with the reflected power of the SMS element while the combined output power is maximized.

In the experiment, the coupling between the cores is estimated first by only seeding one of the signal cores and by measuring the percentage of the total output power coming out of this specific core. It should be noted that a back and forth transfer of power between the cores might happen during the propagation through the fiber. In the following table

the percentage of power emitted by each of the seeded signal cores is shown for different power levels at the output:

Core	Average power / W	Power in the core
1	0.03	89%
1	5	96%
2	5	77%
3	2.5	70%
3	5	83%
4	0.03	89%
4	5	94%

As expected, a higher percentage of power remains in the outer cores at the same power level since they only have a single adjacent core. Besides the intensity, this coupling effect might also impact the temporal phase (and, thereby, the spectral phase) of the strongly stretched pulses. However, it is expected that at higher average powers, the thermal refractive index profile will confine the modes stronger in the core and reduce this coupling.

In operation the stabilization system is activated to optimize the combined output power to its maximum value. Below are the measured values and the combination efficiency calculated according to equation 6.1 for different average powers :

$P_{\max}$ / W	$P_{\min}$ / W	$\eta_{\text{comb}}$
50	1.9	90%
85	4	88%
152	8	86%
176	10	85%

Due to the coupling of the cores an average drop of efficiency (with respect to the ideal case) by about 10% (average of the coupled power) is expected and, therefore, these values fall in the range given by the theoretical maximum efficiency. The drop of efficiency at higher average powers can be explained by thermal effects. Despite the high-quality fused-silica lenses in the telescope behind the fiber, a temperature increase can be observed in them, supported by a visible change of the combined beam profile. These thermal effects can change the angles of the beams at the SMS element and can, therefore, have a detrimental effect on the overlap of the beams and the quality of the

combination process. Additionally, some stability issues could also be observed at higher average powers, which can be related to the coupling lens in front of the fiber. Due to the comparably low efficiency of the amplification process in this fiber, a significant amount of residual pump light will pass through this lens before it is removed by a dichroic pump blocker (placing the pump blocker between the lens and the fiber is not possible due to space constraints). Because this lens is not made of fused silica, a thermal lens impacting the seed beam will also appear. Unfortunately, manufacturing a lens with such a short focal length (20 mm) out of fused silica is very challenging due to the lower refractive index compared to materials such as BK7. Moreover, tests with a 25 mm fused-silica lens did not yield acceptable results (coupling of all four beams simultaneously was not possible).

At a low combined average powers of 10 W, a coefficient-of-variation of the output power of 1% is measured, which is comparable to the fluctuations of the pre-amplifier. In a separate experiment, the origin of the path-length fluctuations to be compensated is investigated. By only employing a piezo to control the distance between the two components of the SMS splitter and using static phase shifters in the different channels, intra-channel fluctuations can be separated from those affecting all channels equally. In this case, a coefficient of variation of 3% is measured, meaning the residual path-length fluctuations are far below the wavelength scale. This stands in contrast to the behaviour observed for spatially separated amplifiers in section 6.3, where path-length fluctuations of multiple wavelengths have to be compensated. In fact, in a carefully designed system, it might be possible to avoid having an active phase control of each individual channel. Finally, the amplified and combined pulses are compressed back to the femtosecond regime. To show the benefits of the multicore fiber, the case where all four signal channels are combined is compared to the case in which the same pulse energy is extracted from a single channel. Due to the large cladding-to-core ratio in the latter case and the limited fiber length, the efficiency of the amplification process is low and only low average powers are achievable. In figure 6.17, the spectra and autocorrelation traces are compared for a repetition rate of 354 kHz and 40 W combined average power (83% combination efficiency measured behind the compressor) and for a repetition rate of 211 kHz and 24 W average power for just the fourth signal core (only 6 W actually arrived at the output due to the lack of constructive interference at the SMS element). In both cases, the combined and compressed pulse energy is 110  $\mu$ J (again, taking into account that only 25% of this power arrives at the output for the single channel case). However, the B-integral is significantly lower when using four signal channels instead of

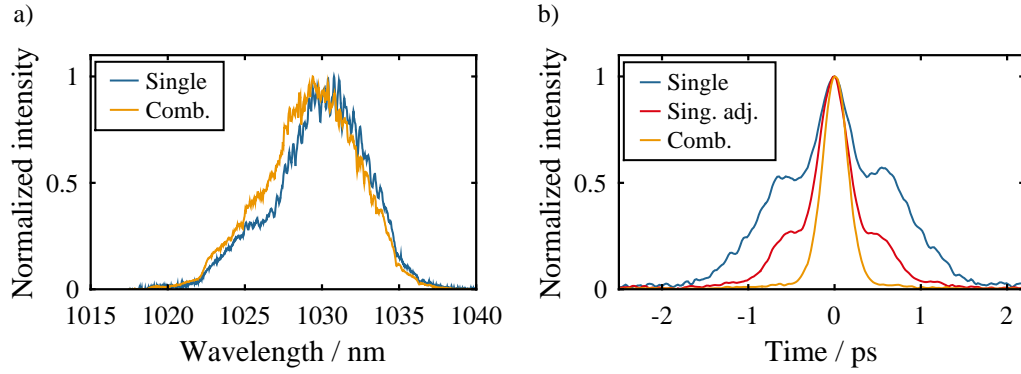


Figure 6.17.: a) Spectra of the single channel (blue) and combined case (orange) for a compressed and combined pulse energy of 110  $\mu\text{J}$  and b) autocorrelation traces for the same setup. The autocorrelation trace for the single channel is first shown for the mini-compressor optimized for the combined case (blue) and then readjusted to provide the shortest pulse (red).

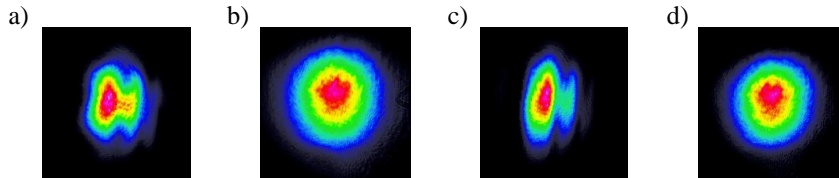


Figure 6.18.: a) Beam after the SMS element and b) after the compressor for a single channel, c) beam after the SMS element and d) after the compressor for the combination of all signal cores.

one (1.1 rad vs. 3.1 rad). In the spectrum, this is visible by the stronger modulation-depth of the spectral modulations and in the autocorrelation trace by a reduction of the pulse quality. Additionally, the mini-compressor had to be readjusted to achieve the shortest pulse duration in this case. It should be noted that the pulse shaper in the system is optimized to provide the best pulse quality in the combined case to allow for a good comparison between both configurations. In figure 6.18 the beams a few cm after the SMS element and after the compressor are shown. As can be seen, fringes are visible on the beam profiles due to diffraction at the edges of the SMS element segments caused by the imperfect confinement of the individual signal modes in the cores. However, after compression, an acceptable intensity beam profile is achieved for both configurations. In summary, the multicore experiment shows a way to integrate many signal channels in a compact footprint which will allow to dramatically increase the number of channels in the future.

## 7. Conclusion & Outlook

In this thesis, the combination of ultrashort laser pulses was explored as a power-scaling concept. The work is motivated by the evolution of the performance of ultrashort fiber laser systems over the last years. Even though tremendous improvements had been made in the decades before and important parameters such as the average power, pulse energy and peak power have been increased by many orders of magnitude, in the last years the progress rate has begun to decline. On the one hand, the pulse energy and peak power are limited by physical effects such as surface damage of the material or self-focusing inside the core. Although a longer stretched pulse duration in the CPA regime would allow to increase these values, they would still be limited by the energy extractable out of the fiber and by the footprint of the compressor. On the other hand, the average power is currently limited by mode-instabilities.

Hence, the coherent combination of ultrashort pulses has been investigated as a way to overcome these shortcomings. More specifically, the combination of multiple spatially separated amplifiers with the filled-aperture beam-combination technique was explored, since this concept can provide a simultaneous increase of the average power, pulse energy and peak power while preserving the beam quality and temporal pulse profile of a single-channel system. Theoretically, this approach allows for a combination with perfect efficiency. However, there are a variety of effects that detrimentally affect the combination process. Theoretical considerations were carried out to investigate the impact of differences between the pulses emitted by the amplifiers. This includes differences in the B-integral or in the optical-path-lengths. For these effects, analytical solutions for the resulting combination efficiency were derived. It could be shown that their impact is small enough to realize laser systems based on coherent combination experimentally with a good combination efficiency. Additionally, the total combination efficiency converges to a fixed values for an increasing number of channels. However, active path-length-stabilization mechanisms are required for stable operation and their mode of operation, especially with a focus on multichannel systems, was investigated.

The spatial coherent combination concept with a fiber-CPA system comprising four

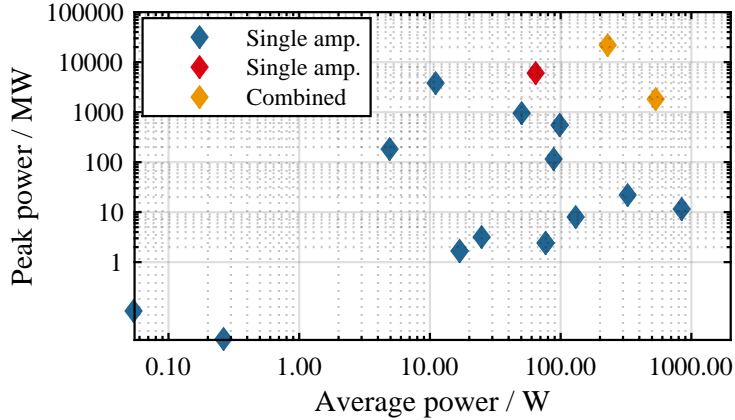


Figure 7.1.: Average power and peak power values of various selected fiber-CPA systems. Blue: previous results with single amplifier systems [4, 14, 15, 55, 57–63, 138, 139], Red: single channel of the high peak power experiment in this thesis, orange: Result of the high average power and high peak power experiments from section 6.3.

parallel state-of-the-art amplifiers was demonstrated experimentally. The system was operated in a high-average-power and in a high-peak-power configuration, differentiated mainly by the type of fiber used and by the bandwidth of the pre-amplifier system. In the first experiment, a compressed average power of 530 W with pulse energies of 1.3 mJ were achieved together with an excellent combination efficiency of 93% and high beam quality. In the second configuration, the system emitted 210 fs pulses with a pulse energy of 5.7 mJ and 22 GW peak power. Again, a very high combination efficiency and beam quality were achieved. While the first experiment provides an unprecedented combination of average power and pulse energy for fiber CPA systems, the second one is, to the best of my knowledge, the highest peak power emitted from a fiber laser system so far. In fact, the peak power from a single channel of the latter system is higher than any previously reported value. In figure 7.1, these results are compared to the output parameters of single-channel ultrashort fiber laser systems with regard to the average power and the peak power. As can be seen, due to the scaling of both parameters with the number of channels, the results presented in this work can be found in the upper right corner of the figure. Hence, the achieved experimental results show the viability of the coherent combination technique as a power-scaling concept for average power and peak power.

Additionally, the coherent combination of two bulk amplifiers has been demonstrated, extending the applicability of this concept to new amplifier architectures. This can also be further extended to include other advanced laser architectures such as the thin-disk

laser and the slab-laser in the future. Besides improving the output power of laser amplifiers, the use of coherent combination for nonlinear compression was also investigated in a proof-of-principle experiment with two solid-core fibers. In this experiment, the self-focusing limit could be overcome.

Finally, for future systems with a large channel count, the compact integration of these channels will play a major role in reducing the footprint and component count and, therefore, the cost. Experimentally, the splitting of one beam into four parallel beams, their subsequent amplification in a multicore fiber with a shared pump cladding and their recombination together with the stabilization of the system was demonstrated in the previously used CPA system. The segmented-mirror-splitter (SMS) design was adapted for the multicore fiber to serve as the splitting and combination element. Even though the fiber had multiple deficiencies, stable operation was successfully shown for up to 176 W of average power. Additionally, the recompression of the pulses to the femtosecond regime and the benefit that four cores provide compared to a single one with respect to the pulse energy was demonstrated.

In summary, coherent combination is a viable path to develop laser systems with performance levels better than what is currently (or even in the future) achievable with a single amplifier system. Due to the increase of the performance parameters with the number of channels, there is no physical reason that sets a fixed limit for the scaling possibilities. Therefore, this concept is an important building block to reach the required parameters even for the most challenging applications in the future, e.g. the realization of high-repetition-rate laser-particle-accelerators [13].

In order to reach this goal, work will have to be done to improve the integration of multiple channels, e.g. multicore fibers with a significant number of cores, also in a 2D-arrangement. The use of host material with a higher thermal conductivity compared to fused-silica, e.g. YAG, might also be beneficial in this context to improve the heat dissipation. Additionally, the required stabilization systems should be further investigated to allow for a compact integration and for the minimization of detrimental side-effects such as intensity fluctuations caused by the applied phase modulations. The application of coherent combination to very high peak power bulk laser systems should also be explored further, while addressing challenges such as the path-length-stabilization at very low repetition rates, allowing for the improvement of peak power and average power for these laser systems. Furthermore, there is the possibility to overcome limitations of nonlinear compression in hollow-core fibers, which will allow to increase the performance of high-repetition-rate few-cycle laser systems. Taking all these promising

future applications into account, the coherent combination technique will certainly be an important building block for next generation laser systems.



# Bibliography

- [1] K. Sugioka and Y. Cheng, “Ultrafast lasers-reliable tools for advanced materials processing,” *Light: Science & Applications* **3**, e149 (2014).
- [2] W. Sibbett, A. A. Lagatsky, and C. T. A. Brown, “The development and application of femtosecond laser systems.” *Optics express* **20**, 6989–7001 (2012).
- [3] Y. Chu, X. Liang, L. Yu, Y. Xu, L. Xu, L. Ma, X. Lu, Y. Liu, Y. Leng, R. Li, and Z. Xu, “High-contrast 20 Petawatt Ti:sapphire laser system,” *Optics Express* **21**, 29231 (2013).
- [4] T. Eidam, S. Hanf, E. Seise, T. V. Andersen, T. Gabler, C. Wirth, T. Schreiber, J. Limpert, and A. Tünnermann, “Femtosecond fiber CPA system emitting 830 W average output power.” *Optics letters* **35**, 94–6 (2010).
- [5] P. Russbueldt, T. Mans, J. Weitenberg, H. D. Hoffmann, and R. Poprawe, “Compact diode-pumped 1.1 kW Yb:YAG Innoslab femtosecond amplifier.” *Optics letters* **35**, 4169–71 (2010).
- [6] C. J. Saraceno, F. Emaury, O. H. Heckl, C. R. E. Baer, M. Hoffmann, C. Schriber, M. Golling, T. Südmeyer, and U. Keller, “275 W average output power from a femtosecond thin disk oscillator operated in a vacuum environment.” *Optics express* **20**, 23535–41 (2012).
- [7] C. Jauregui, J. Limpert, and A. Tünnermann, “High-power fibre lasers,” *Nature Photonics* **7**, 861–867 (2013).
- [8] T. Eidam, C. Wirth, C. Jauregui, F. Stutzki, F. Jansen, H.-J. Otto, O. Schmidt, T. Schreiber, J. Limpert, and A. Tünnermann, “Experimental observations of the threshold-like onset of mode instabilities in high power fiber amplifiers.” *Optics express* **19**, 13218–24 (2011).
- [9] A. V. Smith and J. J. Smith, “Mode instability in high power fiber amplifiers.” *Optics express* **19**, 10180–92 (2011).

- [10] M. Ferray, A. L’Huillier, X. F. Li, L. A. Lompre, G. Mainfray, and C. Manus, “Multiple-harmonic conversion of 1064 nm radiation in rare gases,” *Journal of Physics B: Atomic, Molecular and Optical Physics* **21**, L31 (1988).
- [11] A. McPherson, G. Gibson, H. Jara, U. Johann, T. S. Luk, I. A. McIntyre, K. Boyer, and C. K. Rhodes, “Studies of multiphoton production of vacuum-ultraviolet radiation in the rare gases,” *J. Opt. Soc. Am. B* **4**, 595–601 (1987).
- [12] V. Malka, J. Faure, Y. A. Gauduel, E. Lefebvre, A. Rousse, and K. T. Phuoc, “Principles and applications of compact laser-plasma accelerators,” *Nature Physics* **4**, 447–453 (2008).
- [13] W. Leemans, “White paper of the ICFA-ICUIL joint task force: High power laser technology for accelerators,” *ICFA Beam Dyn. Newslett.* **56**, 10–88 (2011).
- [14] F. Röser, T. Eidam, J. Rothhardt, O. Schmidt, D. N. Schimpf, J. Limpert, and A. Tünnermann, “Millijoule pulse energy high repetition rate femtosecond fiber chirped-pulse amplification system,” *Opt. Lett.* **32**, 3495–3497 (2007).
- [15] T. Eidam, J. Rothhardt, F. Stutzki, F. Jansen, S. Hädrich, H. Carstens, C. Jau-regui, J. Limpert, and A. Tünnermann, “Fiber chirped-pulse amplification system emitting 3.8 GW peak power.” *Optics express* **19**, 255–60 (2011).
- [16] G. Agrawal, *Nonlinear Fiber Optics* (Academic Press, 2007), 3rd ed.
- [17] H. R. Telle, G. Steinmeyer, A. E. Dunlop, J. Stenger, D. H. Sutter, and U. Keller, “Carrier-envelope offset phase control: A novel concept for absolute optical frequency measurement and ultrashort pulse generation,” *Applied Physics B: Lasers and Optics* **69**, 327–332 (1999).
- [18] K. T. Ajoy Ghatak, *Introduction to Fiber Optics* (Cambridge University Press, 1998).
- [19] P. Russell, “Photonic Crystal Fibers,” *Science* **299**, 358–362 (2003).
- [20] W. Koechner, “Thermal Lensing in a Nd:YAG Laser Rod.” *Applied optics* **9**, 2548–53 (1970).
- [21] D. E. Zelmon, D. L. Small, and R. Page, “Refractive-Index Measurements of Undoped Yttrium Aluminum Garnet from 0.4 to 5.0  $\mu\text{m}$ ,” *Applied Optics* **37**, 4933 (1998).
- [22] D. B. Leviton and B. J. Frey, “Temperature-dependent absolute refractive index measurements of synthetic fused silica,” in “SPIE Astronomical Telescopes + In-

- strumentation,” , E. Atad-Ettedgui, J. Antebi, and D. Lemke, eds. (International Society for Optics and Photonics, 2006), pp. 62732K–62732K–11.
- [23] D. Strickland and G. Mourou, “Compression of amplified chirped optical pulses,” *Optics Communications* **56**, 219–221 (1985).
- [24] D. Milam, “Review and Assessment of Measured Values of the Nonlinear Refractive-Index Coefficient of Fused Silica,” *Applied Optics* **37**, 546 (1998).
- [25] D. N. Schimpf, E. Seise, J. Limpert, and A. Tünnermann, “The impact of spectral modulations on the contrast of pulses of nonlinear chirped-pulse amplification systems,” *Optics Express* **16**, 10664 (2008).
- [26] D. Schimpf, E. Seise, J. Limpert, and A. Tünnermann, “Self-phase modulation compensated by positive dispersion in chirped-pulse systems,” *Opt. Express* **17**, 4997–5007 (2009).
- [27] E. Ippen, “Passive mode locking of the cw dye laser,” *Applied Physics Letters* **21**, 348 (1972).
- [28] S. Johnson, M. Ibanescu, M. Skorobogatiy, O. Weisberg, T. Engeness, M. Soljacic, S. Jacobs, J. Joannopoulos, and Y. Fink, “Low-loss asymptotically single-mode propagation in large-core OmniGuide fibers,” *Optics Express* **9**, 748 (2001).
- [29] J. Limpert, F. Stutzki, F. Jansen, H.-J. Otto, T. Eidam, C. Jauregui, and A. Tünnermann, “Yb-doped large-pitch fibres: effective single-mode operation based on higher-order mode delocalisation,” *Light: Science & Applications* **1**, e8 (2012).
- [30] C. J. Koester and E. Snitzer, “Amplification in a Fiber Laser,” *Applied Optics* **3**, 1182 (1964).
- [31] H. M. Pask, R. J. Carman, D. C. Hanna, A. C. Tropper, C. J. Mackechnie, P. R. Barber, and J. M. Dawes, “Ytterbium-doped silica fiber lasers: versatile sources for the 1-1.2  $\mu\text{m}$  region,” *Selected Topics in Quantum Electronics, IEEE Journal of* **1**, 2–13 (1995).
- [32] T. T. Alkeskjold, M. Laurila, L. Scolari, and J. Broeng, “Single-Mode ytterbium-doped Large-Mode-Area photonic bandgap rod fiber amplifier.” *Optics express* **19**, 7398–409 (2011).
- [33] J. R. Armitage, “Three-level fiber laser amplifier: a theoretical model.” *Applied optics* **27**, 4831–6 (1988).

- [34] ISO Standard 11146, “Lasers and laser related equipment: Test methods for laser beam widths, divergence angles and beam propagation ratios,” (2005).
- [35] J. Limpert, F. Roser, D. Schimpf, E. Seise, T. Eidam, S. Hadrich, J. Rothhardt, C. Misas, and A. Tünnermann, “High Repetition Rate Gigawatt Peak Power Fiber Laser Systems: Challenges, Design, and Experiment,” *IEEE Journal of Selected Topics in Quantum Electronics* **15**, 159–169 (2009).
- [36] F. Stutzki, F. Jansen, T. Eidam, A. Steinmetz, C. Jauregui, J. Limpert, and A. Tünnermann, “High average power large-pitch fiber amplifier with robust single-mode operation.” *Optics letters* **36**, 689–91 (2011).
- [37] E. Treacy, “Optical pulse compression with diffraction gratings,” *Quantum Electronics, IEEE Journal of* **5**, 454–458 (1969).
- [38] L. M. Frantz and J. S. Nodvik, “Theory of Pulse Propagation in a Laser Amplifier,” *Journal of Applied Physics* **34**, 2346 (1963).
- [39] S. G. Fermann Martin, Galvanauskas Almantas, *Ultrafast Lasers: Technology and Applications* (2003).
- [40] A. E. Siegman, *Lasers* (University Science Books, 1986).
- [41] G. S. Martin E. Fermann Almantas Galvanauskas, *Ultrafast Lasers* (Marcel Dekker, Inc., 2003).
- [42] R. W. Boyd, *Nonlinear Optics* (Academic Press, Inc., 1992).
- [43] D. N. Schimpf, T. Eidam, E. Seise, S. Hädrich, J. Limpert, and A. Tünnermann, “Circular versus linear polarization in laser-amplifiers with Kerr-nonlinearity.” *Optics express* **17**, 18774–81 (2009).
- [44] D. N. Schimpf, J. Limpert, and A. Tünnermann, “Controlling the influence of SPM in fiber-based chirped-pulse amplification systems by using an actively shaped parabolic spectrum,” *Optics Express* **15**, 16945 (2007).
- [45] A. M. Weiner, D. E. Leaird, J. S. Patel, and J. R. Wullert, “Programmable femtosecond pulse shaping by use of a multielement liquid-crystal phase modulator,” *Optics Letters* **15**, 326 (1990).
- [46] V. V. Lozovoy, I. Pastirk, and M. Dantus, “Multiphoton intrapulse interference .IV. Ultrashort laser pulse spectral phase characterization and compensation,” *Optics Letters* **29**, 775 (2004).
- [47] W. Koechner, *Solid-State Laser Engineering* (Springer, 2006).

- [48] J. H. Campbell and F. Rainer, “Optical glasses for high-peak-power laser applications,” in “Proc. SPIE 1761,” , J. B. Breckinridge and A. J. Marker III, eds. (International Society for Optics and Photonics, 1993), pp. 246–255.
- [49] A. V. Smith and B. T. Do, “Bulk and surface laser damage of silica by picosecond and nanosecond pulses at 1064 nm,” *Applied Optics* **47**, 4812 (2008).
- [50] F. Stutzki, F. Jansen, A. Liem, C. Jauregui, J. Limpert, and A. Tünnermann, “26 mJ, 130 W Q-switched fiber-laser system with near-diffraction-limited beam quality.” *Optics letters* **37**, 1073–5 (2012).
- [51] F. Jansen, F. Stutzki, H.-J. Otto, T. Eidam, A. Liem, C. Jauregui, J. Limpert, and A. Tünnermann, “Thermally induced waveguide changes in active fibers.” *Optics express* **20**, 3997–4008 (2012).
- [52] D. Brown and H. Hoffman, “Thermal, stress, and thermo-optic effects in high average power double-clad silica fiber lasers,” *IEEE Journal of Quantum Electronics* **37**, 207–217 (2001).
- [53] F. Jansen, F. Stutzki, H.-J. Otto, C. Jauregui, J. Limpert, and A. Tünnermann, “High-power thermally guiding index-antiguinding-core fibers.” *Optics letters* **38**, 510–2 (2013).
- [54] J. Malchus, V. Krause, G. Rehmann, M. Leers, A. Koesters, and D. G. Matthews, “A 40kW fiber-coupled diode laser for material processing and pumping applications,” *SPIE Photonics West 2015-LASE: Lasers and Sources* **9348** (2015).
- [55] M. E. Fermann, A. Galvanauskas, and D. Harter, “All-fiber source of 100-nJ sub-picosecond pulses,” *Applied Physics Letters* **64**, 1315 (1994).
- [56] A. Galvanauskas, G. C. Cho, A. Hariharan, M. E. Fermann, and D. Harter, “Generation of high-energy femtosecond pulses in multimode-core Yb-fiber chirped-pulse amplification systems,” *Optics Letters* **26**, 935 (2001).
- [57] L. Shah, Z. Liu, I. Hartl, G. Imeshev, G. C. Cho, and M. E. Fermann, “High energy femtosecond Yb cubicon fiber amplifier,” *Optics Express* **13**, 4717 (2005).
- [58] J. D. Minelly, A. Galvanauskas, M. E. Fermann, D. Harter, J. E. Caplen, Z. J. Chen, and D. N. Payne, “Femtosecond pulse amplification in cladding-pumped fibers,” *Optics Letters* **20**, 1797 (1995).
- [59] J. Limpert, T. Schreiber, T. Clausnitzer, K. Zöllner, H. Fuchs, E. Kley, H. Zellmer, and A. Tünnermann, “High-power femtosecond Yb-doped fiber amplifier,” *Optics Express* **10**, 628 (2002).

- [60] J. Limpert, T. Clausnitzer, A. Liem, T. Schreiber, H.-J. Fuchs, H. Zellmer, E.-B. Kley, and A. Tünnermann, “High-average-power femtosecond fiber chirped-pulse amplification system,” *Optics Letters* **28**, 1984 (2003).
- [61] F. Röser, D. Schimpf, O. Schmidt, B. Ortac, K. Rademaker, J. Limpert, and A. Tünnermann, “90 W average power 100  $\mu$ J energy femtosecond fiber chirped-pulse amplification system,” *Optics Letters* **32**, 2230 (2007).
- [62] F. Röser, J. Rothhard, B. Ortac, A. Liem, O. Schmidt, T. Schreiber, J. Limpert, and A. Tünnermann, “131 W 220 fs fiber laser system,” *Optics Letters* **30**, 2754 (2005).
- [63] T. Eidam, S. Hadrich, F. Roser, E. Seise, T. Gottschall, J. Rothhardt, T. Schreiber, J. Limpert, and A. Tünnermann, “A 325-W-Average-Power Fiber CPA System Delivering Sub-400 fs Pulses,” *IEEE Journal of Selected Topics in Quantum Electronics* **15**, 187–190 (2009).
- [64] D. N. Schimpf, J. Limpert, and A. Tünnermann, “Optimization of high performance ultrafast fiber laser systems to >10 GW peak power,” *Journal of the Optical Society of America B* **27**, 2051 (2010).
- [65] T. Zhang, M. Yonemura, and Y. Kato, “An array-grating compressor for high-power chirped-pulse amplification lasers,” *Optics Communications* **145**, 367–376 (1998).
- [66] H.-J. Otto, F. Stutzki, N. Modsching, C. Jauregui, J. Limpert, and A. Tünnermann, “2 kW average power from a pulsed Yb-doped rod-type fiber amplifier.” *Optics letters* **39**, 6446–9 (2014).
- [67] C. Jauregui, H.-J. Otto, F. Stutzki, F. Jansen, J. Limpert, and A. Tünnermann, “Passive mitigation strategies for mode instabilities in high-power fiber laser systems.” *Optics express* **21**, 19375–86 (2013).
- [68] H.-J. Otto, C. Jauregui, F. Stutzki, F. Jansen, J. Limpert, and A. Tünnermann, “Controlling mode instabilities by dynamic mode excitation with an acousto-optic deflector.” *Optics express* **21**, 17285–98 (2013).
- [69] N. Soleimani, B. Ponting, E. Gebremichael, A. Ribuoat, and G. Maxwell, “Coilable single crystals fibers of doped-YAG for high power laser applications,” in “*SPIE LASE*,” , W. A. Clarkson and R. K. Shori, eds. (International Society for Optics and Photonics, 2014), p. 895903.

- [70] J. E. Ripper, “OPTICAL COUPLING OF ADJACENT STRIPE-GEOMETRY JUNCTION LASERS,” *Applied Physics Letters* **17**, 371 (1970).
- [71] W. B. Veldkamp, J. R. Leger, and G. J. Swanson, “Coherent summation of laser beams using binary phase gratings,” *Optics Letters* **11**, 303 (1986).
- [72] S. J. Augst, T. Y. Fan, and A. Sanchez, “Coherent beam combining and phase noise measurements of ytterbium fiber amplifiers,” *Optics Letters* **29**, 474 (2004).
- [73] E. Seise, A. Klenke, J. Limpert, and A. Tünnermann, “Coherent addition of fiber-amplified ultrashort laser pulses.” *Optics express* **18**, 27827–35 (2010).
- [74] L. Daniault, M. Hanna, L. Lombard, Y. Zaouter, E. Mottay, D. Goular, P. Bourdon, F. Druon, and P. Georges, “Coherent beam combining of two femtosecond fiber chirped-pulse amplifiers.” *Optics letters* **36**, 621–3 (2011).
- [75] T. Fan, “Laser beam combining for high-power, high-radiance sources,” *IEEE Journal of Selected Topics in Quantum Electronics* **11**, 567–577 (2005).
- [76] E. C. Cheung, J. G. Ho, T. S. McComb, and S. Palese, “High density spectral beam combination with spatial chirp precompensation.” *Optics express* **19**, 20984–90 (2011).
- [77] P. Hariharan, *Basics of interferometry* (Academic Press, Inc., 1992).
- [78] F. Guichard, M. Hanna, L. Lombard, Y. Zaouter, C. Hönninger, F. Morin, F. Druon, E. Mottay, and P. Georges, “Two-channel pulse synthesis to overcome gain narrowing in femtosecond fiber amplifiers.” *Optics letters* **38**, 5430–3 (2013).
- [79] G. Krauss, S. Lohss, T. Hanke, A. Sell, S. Eggert, R. Huber, and A. Leitenstorfer, “Synthesis of a single cycle of light with compact erbium-doped fibre technology,” *Nat Photon* **4**, 33–36 (2010).
- [80] C. Manzoni, S.-W. Huang, G. Cirmi, P. Farinello, J. Moses, F. X. Kärtner, and G. Cerullo, “Coherent synthesis of ultra-broadband optical parametric amplifiers.” *Optics letters* **37**, 1880–2 (2012).
- [81] Z. Chen, J. Hou, P. Zhou, X. Wang, X. Xu, Z. Jiang, and Z. Liu, “Mutual injection locking and coherent combining of three individual fiber lasers,” *Optics Communications* **282**, 60–63 (2009).
- [82] S. Zhou, F. W. Wise, and D. G. Ouzounov, “Divided-pulse amplification of ultrashort pulses,” *Optics Letters* **32**, 871 (2007).

- [83] M. Kienel, A. Klenke, T. Eidam, M. Baumgartl, C. Jauregui, J. Limpert, and A. Tünnermann, “Analysis of passively combined divided-pulse amplification as an energy-scaling concept.” *Optics express* **21**, 29031–42 (2013).
- [84] Y. Zaouter, F. Guichard, L. Daniault, M. Hanna, F. Morin, C. Hönninger, E. Motay, F. Druon, and P. Georges, “Femtosecond fiber chirped- and divided-pulse amplification system.” *Optics letters* **38**, 106–8 (2013).
- [85] I. Pupeza, T. Eidam, J. Rauschenberger, B. Bernhardt, A. Ozawa, E. Fill, A. Apolonski, T. Udem, J. Limpert, Z. A. Alahmed, A. M. Azzeer, A. Tünnermann, T. W. Hänsch, and F. Krausz, “Power scaling of a high-repetition-rate enhancement cavity,” *Opt. Lett.* **35**, 2052–2054 (2010).
- [86] S. Breitkopf, T. Eidam, A. Klenke, L. von Grafenstein, H. Carstens, S. Holzberger, E. Fill, T. Schreiber, F. Krausz, A. Tünnermann, I. Pupeza, and J. Limpert, “A concept for multiterawatt fibre lasers based on coherent pulse stacking in passive cavities,” *Light: Science & Applications* **3**, e211 (2014).
- [87] M. Fridman, V. Eckhouse, N. Davidson, and A. A. Friesem, “Simultaneous coherent and spectral addition of fiber lasers,” *Optics Letters* **33**, 648 (2008).
- [88] M. Kienel, M. Müller, A. Klenke, T. Eidam, J. Limpert, and A. Tünnermann, “Multidimensional coherent pulse addition of ultrashort laser pulses.” *Optics letters* **40**, 522–5 (2015).
- [89] J. Bourderionnet, C. Bellanger, J. Primot, and A. Brignon, “Collective coherent phase combining of 64 fibers.” *Optics express* **19**, 17053–8 (2011).
- [90] R. C. JONES, “A New Calculus for the Treatment of Optical Systems,” *Journal of the Optical Society of America* **31**, 488 (1941).
- [91] R. Uberna, A. Bratcher, and B. G. Tiemann, “Coherent Polarization Beam Combination,” *IEEE Journal of Quantum Electronics* **46**, 1191–1196 (2010).
- [92] H. Dammann and K. Görtler, “High-efficiency in-line multiple imaging by means of multiple phase holograms,” *Optics Communications* **3**, 312–315 (1971).
- [93] E. C. Cheung, J. G. Ho, G. D. Goodno, R. R. Rice, J. Rothenberg, P. Thielen, M. Weber, and M. Wickham, “Diffractive-optics-based beam combination of a phase-locked fiber laser array,” *Optics Letters* **33**, 354 (2008).
- [94] P. a. Thielen, J. G. Ho, D. a. Burchman, G. D. Goodno, J. E. Rothenberg, M. G. Wickham, A. Flores, C. a. Lu, B. Pulford, C. Robin, A. D. Sanchez, D. Hult,



- and K. B. Rowland, “Two-dimensional diffractive coherent combining of 15 fiber amplifiers into a 600 W beam.” *Optics letters* **37**, 3741–3 (2012).
- [95] A. Klenke, E. Seise, J. Limpert, and A. Tünnermann, “Basic considerations on coherent combining of ultrashort laser pulses.” *Optics express* **19**, 25379–87 (2011).
- [96] D. Kane and R. Trebino, “Characterization of arbitrary femtosecond pulses using frequency-resolved optical gating,” *IEEE Journal of Quantum Electronics* **29**, 571–579 (1993).
- [97] C. Iaconis and I. Walmsley, “Spectral phase interferometry for direct electric-field reconstruction of ultrashort optical pulses,” *Optics Letters* **23**, 792 (1998).
- [98] O. Shapira, A. F. Abouraddy, J. D. Joannopoulos, and Y. Fink, “Complete Modal Decomposition for Optical Waveguides,” *Physical Review Letters* **94**, 143902 (2005).
- [99] I. H. MALITSON, “Interspecimen Comparison of the Refractive Index of Fused Silica,” *Journal of the Optical Society of America* **55**, 1205 (1965).
- [100] G. D. Goodno, C.-C. Shih, and J. E. Rothenberg, “Perturbative analysis of coherent combining efficiency with mismatched lasers.” *Optics express* **18**, 25403–25414 (2010).
- [101] T. Gustafson, P. Kelly, and R. Fisher, “Subpicosecond pulse generation using the optical Kerr effect,” *IEEE Journal of Quantum Electronics* **5**, 325–325 (1969).
- [102] Y. Zaouter, L. Daniault, M. Hanna, D. N. Papadopoulos, F. Morin, C. Hönniger, F. Druon, E. Mottay, and P. Georges, “Passive coherent combination of two ultrafast rod type fiber chirped pulse amplifiers.” *Optics letters* **37**, 1460–2 (2012).
- [103] T. Hansch and B. Couillaud, “Laser frequency stabilization by polarization spectroscopy of a reflecting reference cavity,” *Optics Communications* **35**, 441–444 (1980).
- [104] T. M. Shay, “Theory of electronically phased coherent beam combination without a reference beam,” *Optics Express* **14**, 12188 (2006).
- [105] M. A. Vorontsov, G. W. Carhart, and J. C. Ricklin, “Adaptive phase-distortion correction based on parallel gradient-descent optimization,” *Optics Letters* **22**, 907 (1997).
- [106] S. B. Weiss, M. E. Weber, and G. D. Goodno, “Group delay locking of coherently combined broadband lasers.” *Optics letters* **37**, 455–7 (2012).

- [107] M. Müller, M. Kienel, A. Klenke, T. Eidam, J. Limpert, and A. Tünnermann, “Phase stabilization of multidimensional amplification architectures for ultrashort pulses,” in “SPIE LASE,” , L. B. Shaw, ed. (International Society for Optics and Photonics, 2015), p. 93441D.
- [108] G. D. Goodno and S. B. Weiss, “Automated co-alignment of coherent fiber laser arrays via active phase-locking,” *Optics Express* **20**, 14945 (2012).
- [109] C. Geng, W. Luo, Y. Tan, H. Liu, J. Mu, and X. Li, “Experimental demonstration of using divergence cost-function in SPGD algorithm for coherent beam combining with tip/tilt control.” *Optics express* **21**, 25045–55 (2013).
- [110] R. W. P. Drever, J. L. Hall, F. V. Kowalski, J. Hough, G. M. Ford, A. J. Munley, and H. Ward, “Laser phase and frequency stabilization using an optical resonator,” *Applied Physics B Photophysics and Laser Chemistry* **31**, 97–105 (1983).
- [111] L. A. Siiman, W.-z. Chang, T. Zhou, and A. Galvanauskas, “Coherent femtosecond pulse combining of multiple parallel chirped pulse fiber amplifiers.” *Optics express* **20**, 18097–116 (2012).
- [112] E. Seise, A. Klenke, S. Breilkopf, J. Limpert, and A. Tünnermann, “88 W 0.5 mJ femtosecond laser pulses from two coherently combined fiber amplifiers.” *Optics letters* **36**, 3858–60 (2011).
- [113] A. Klenke, E. Seise, S. Demmler, J. Rothhardt, S. Breilkopf, J. Limpert, and A. Tünnermann, “Coherently-combined two channel femtosecond fiber CPA system producing 3 mJ pulse energy.” *Optics express* **19**, 24280–5 (2011).
- [114] V. E. Leshchenko, V. A. Vasiliev, N. L. Kvashnin, and E. V. Pestryakov, “Coherent combining of relativistic-intensity femtosecond pulses,” .
- [115] G. Cheriaux, P. Rousseau, F. Salin, J. P. Chambaret, B. Walker, and L. F. Dimmauro, “Aberration-free stretcher design for ultrashort-pulse amplification,” *Optics Letters* **21**, 414 (1996).
- [116] A. Klenke, S. Breilkopf, M. Kienel, T. Gottschall, T. Eidam, S. Hädrich, J. Rothhardt, J. Limpert, and A. Tünnermann, “530 W, 1.3 mJ, four-channel coherently combined femtosecond fiber chirped-pulse amplification system.” *Optics letters* **38**, 2283–5 (2013).
- [117] A. Klenke, S. Hädrich, T. Eidam, J. Rothhardt, M. Kienel, S. Demmler, T. Gottschall, J. Limpert, and A. Tünnermann, “22 GW peak power fiber chirped pulse amplification system.” *Optics letters* **39**, 6875–8 (2014).

- [118] Y. Wang, C.-Q. Xu, and H. Po, “Analysis of Raman and thermal effects in kilowatt fiber lasers,” *Optics Communications* **242**, 487–502 (2004).
- [119] A. Ali, “On laser air breakdown, threshold power and laser generated channel length,” Nrl (1983).
- [120] T. Popmintchev, M.-C. Chen, P. Arpin, M. M. Murnane, and H. C. Kapteyn, “The attosecond nonlinear optics of bright coherent X-ray generation,” *Nature Photonics* **4**, 822–832 (2010).
- [121] S. Hädrich, A. Klenke, A. Hoffmann, T. Eidam, T. Gottschall, J. Rothhardt, J. Limpert, and A. Tünnermann, “Nonlinear compression to sub-30-fs, 0.5 mJ pulses at 135 W of average power.” *Optics letters* **38**, 3866–9 (2013).
- [122] S. Hädrich, A. Klenke, J. Rothhardt, M. Krebs, A. Hoffmann, O. Pronin, V. Pervak, J. Limpert, and A. Tünnermann, “High photon flux table-top coherent extreme-ultraviolet source,” *Nature Photonics* **8**, 779–783 (2014).
- [123] J. Rothhardt, S. Hädrich, A. Klenke, S. Demmler, A. Hoffmann, T. Gottschall, T. Eidam, M. Krebs, J. Limpert, and A. Tünnermann, “53 W average power few-cycle fiber laser system generating soft x rays up to the water window.” *Optics letters* **39**, 5224–7 (2014).
- [124] M. Kienel, M. Müller, S. Demmler, J. Rothhardt, A. Klenke, T. Eidam, J. Limpert, and A. Tünnermann, “Coherent beam combination of Yb:YAG single-crystal rod amplifiers.” *Optics letters* **39**, 3278–81 (2014).
- [125] X. Délen, Y. Zaouter, I. Martial, N. Aubry, J. Didierjean, C. Hönninger, E. Mottay, F. Balembois, and P. Georges, “Yb:YAG single crystal fiber power amplifier for femtosecond sources.” *Optics letters* **38**, 109–11 (2013).
- [126] M. Bradler, P. Baum, and E. Riedle, “Femtosecond continuum generation in bulk laser host materials with sub- $\mu$ J pump pulses,” *Applied Physics B* **97**, 561–574 (2009).
- [127] A. Sennaroglu, *Solid-State Lasers and Applications* (CRC Press, 2007).
- [128] A. Klenke, S. Hädrich, M. Kienel, T. Eidam, J. Limpert, and A. Tünnermann, “Coherent combination of spectrally broadened femtosecond pulses for nonlinear compression.” *Optics letters* **39**, 3520–2 (2014).
- [129] R. Harney and J. Schipper, *Passive and active pulse stacking scheme for pulse shaping* (U.S. patent 4059759, 1977).

- [130] S. Bohman, A. Suda, M. Kaku, M. Nurhuda, T. Kanai, S. Yamaguchi, and K. Midorikawa, “Generation of 5 fs, 0.5 TW pulses focusable to relativistic intensities at 1 kHz,” *Optics Express* **16**, 10684 (2008).
- [131] H. Carstens, N. Lilienfein, S. Holzberger, C. Jocher, T. Eidam, J. Limpert, A. Tünnermann, J. Weitenberg, D. C. Yost, A. Alghamdi, Z. Alahmed, A. Azzeer, A. Apolonski, E. Fill, F. Krausz, and I. Pupeza, “Megawatt-scale average-power ultrashort pulses in an enhancement cavity.” *Optics letters* **39**, 2595–8 (2014).
- [132] S. Matsuo, Y. Sasaki, I. Ishida, K. Takenaga, K. Saitoh, and M. Koshihara, “Recent Progress in Multi core and Few mode Fiber,” in “Optical Fiber Communication Conference/National Fiber Optic Engineers Conference 2013,” (OSA, Washington, D.C., 2013), p. OM3L3.
- [133] J. Lhermite, E. Suran, V. Kermene, F. Louradour, A. Desfarges-Berthelemot, and A. Barthélémy, “Coherent combining of 49 laser beams from a multiple core optical fiber by a spatial light modulator.” *Optics express* **18**, 4783–9 (2010).
- [134] L. P. Ramirez, M. Hanna, G. Bouwmans, H. El Hamzaoui, M. Bouazaoui, D. Labat, K. Delplace, J. Pouysegur, F. Guichard, P. Rigaud, V. Kermène, A. Desfarges-Berthelemot, A. Barthélémy, F. Prévost, L. Lombard, Y. Zaouter, F. Druon, and P. Georges, “Coherent beam combining with an ultrafast multicore Yb-doped fiber amplifier.” *Optics express* **23**, 5406–16 (2015).
- [135] H.-J. Otto, A. Klenke, C. Jauregui, F. Stutzki, J. Limpert, and A. Tünnermann, “Scaling the mode instability threshold with multicore fibers.” *Optics letters* **39**, 2680–3 (2014).
- [136] F. Stutzki, “Performance scaling of Yb- and Tm-based ultrashort-pulse fiber laser systems Thesis by Fabian Stutzki,” Ph.D. thesis (2015).
- [137] F. Jansen, F. Stutzki, H.-J. Otto, M. Baumgartl, C. Jauregui, J. Limpert, and A. Tünnermann, “The influence of index-depressions in core-pumped Yb-doped large pitch fibers.” *Optics express* **18**, 26834–42 (2010).
- [138] A. Galvanauskas, P. Blixt, and J. A. Tellefsen, “Generation of femtosecond optical pulses with nanojoule energy from a diode laser and fiber based system,” *Applied Physics Letters* **63**, 1742 (1993).
- [139] A. Malinowski, A. Piper, J. H. V. Price, K. Furusawa, Y. Jeong, J. Nilsson, and D. J. Richardson, “Ultrashort-pulse Yb<sup>3+</sup>-fiber-based laser and amplifier system producing >25-W average power,” (2004).

# A. Calculation of the maximum stretched pulse duration

In order to get an estimation of the maximum stretched pulse duration that is possible to achieve with a given grating size  $D$  in the compressor, the difference between the travelling time of the shortest and longest wavelength components can be calculated. In figure A.1 the different optical lengths are shown. The distance between the gratings is  $l$  for the center wavelength  $\lambda_0$ . In a double-pass configuration, the maximum propagation length difference between the two spectral components is  $\Delta L = 2(l_{11} + l_{12} - (l_{21} - l_{22}))$ . The first two of these terms can easily be deduced from the figure:

$$\begin{aligned} l_{11} &= \sqrt{\left(\frac{D}{2}\right)^2 + l^2} - 2\left(\frac{D}{2}\right)l \cos(90^\circ + \beta) \\ l_{12} &= \left(\frac{D}{2}\right) \sin(\alpha) \end{aligned} \quad (\text{A.1})$$

By applying the approximation  $l^2 \gg \left(\frac{D}{2}\right)^2$ , these equations can be simplified. Similarly, the difference of the second pair of path lengths can be calculated, resulting in the total

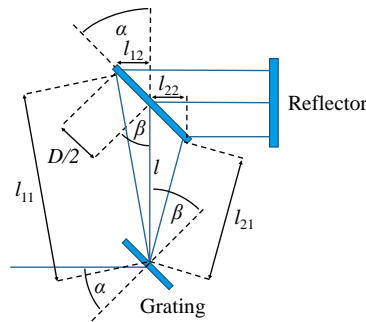


Figure A.1.: Optical paths in a compressor with a grating width  $D$ , an incident angle  $\alpha$ , an angle of refraction  $\beta$  of the center wavelength, which has a propagation length  $L$ .

propagation length difference:

$$\begin{aligned}\Delta L &\approx 2 \left( l + \left( \frac{D}{2} \right) \sin(\beta) + \left( \frac{D}{2} \right) \sin(\alpha) - \left( l - \left( \frac{D}{2} \right) \sin(\beta) - \left( \frac{D}{2} \right) \sin(\alpha) \right) \right) \\ &\approx 2D (\sin(\beta) + \sin(\alpha))\end{aligned}\tag{A.2}$$

By introducing the grating equation for the first diffraction order  $d(\sin(\beta) + \sin(\alpha)) = \lambda_0$ , this result can be simplified to equation 2.20:

$$\tau_{\max} \approx \frac{2D\lambda_0}{dc_0} \approx \frac{4\pi D}{d\omega_0}\tag{A.3}$$

## B. Calculation of the combination efficiency for the multicore fiber

In order to calculate the combination efficiency of the multicore fiber with the SMS element by using the maximum and minimum power behind it, the total power that coherently combines  $P_{\text{comb}}$  and the power that does not combine  $P_{\text{not\_comb}}$  have to be defined. All power values in this section are assumed to be time-averaged which do not take into account the temporal pulse profile, i.e. they are the average power values. In total, the power emitted from the amplifiers is  $P_{\text{total}} = P_{\text{comb}} + P_{\text{not\_comb}}$ . If the system is optimized for the highest combined power, the power  $P_{\text{max}} = P_{\text{comb}} + \frac{1}{N}P_{\text{not\_comb}}$  is measured as the combined output for  $N$  channels. The prefactor  $\frac{1}{N}$  results from the fact that if no interference takes places, then only a fraction  $\frac{1}{N}$  of the power launched by a specific channel arrives at the output of the SMS element, while the rest of the power is reflected at the various segments. If the system is optimized for the minimum combined average power,  $P_{\text{min}} = \frac{1}{N}P_{\text{not\_comb}}$  is measured at the output. In order to calculate the combination efficiency, the following equation can be used, which is based on equation 4.2:

$$\eta_{\text{comb}} = \frac{P_{\text{max}}}{P_{\text{total}}} = \frac{P_{\text{max}}}{P_{\text{comb}} + P_{\text{not\_comb}}} = \frac{P_{\text{max}}}{P_{\text{max}} - \frac{1}{N}P_{\text{not\_comb}} + N \cdot P_{\text{min}}} \quad (\text{B.1})$$

$$= \frac{P_{\text{max}}}{P_{\text{max}} - P_{\text{min}} + N \cdot P_{\text{min}}} = \frac{P_{\text{max}}}{P_{\text{max}} + (N - 1) \cdot P_{\text{min}}} \quad (\text{B.2})$$

Hence, by assuming a four channel system ( $N = 4$ ), this results in equation 6.1.

# Zusammenfassung (Summary)

Ultrakurzpuls-Laser haben sich inzwischen als Werkzeug in verschiedenen Bereichen etabliert. Dabei sind die Anforderungen an die erreichbaren Pulsenergien, Pulsspitzenleistungen und Durchschnittsleistungen immer weiter gestiegen. Die erforderlichen oder gewünschten Parameter wie Pulsenergie, Pulsspitzenleistung und Repetitionsraten sind mit einem einzelnen Lasersystem in vielen Fällen aufgrund von physikalischen Limitierungen nicht erreichbar. Deshalb ist die Parallelisierung, also die Kombination der Ausgangsstrahlen mehrerer Laserverstärker ein Weg diese Limitierungen zu umgehen. In dieser Arbeit wurde die kohärente Kombination ultrakurzer Pulse theoretisch und experimentell beleuchtet. Bei der kohärenten Kombination sind die Pulse der einzelnen Laserverstärker in ihrem spektralen und zeitlichen Pulsprofil möglichst identisch. Abweichungen, z.B. durch unterschiedliche Pfadlängen in den Kanälen oder durch nichtlineare Effekte haben einen negativen Effekt auf die Kombinationseffizienz, was durch einfache analytische Gleichungen beschrieben werden kann. Zusätzlich wurden verschiedene aktive Stabilisierungsmechanismen für die Pfadlängen untersucht, besonders in Hinblick auf die Multikanalfähigkeit. Im experimentellen Teil wurden die gewonnenen Erkenntnisse angewendet um ein 4-Kanal Faser CPA System in 2 verschiedenen Konfigurationen aufzubauen und zu charakterisieren. Dabei konnte zuerst eine komprimierte Durchschnittsleistung von 530 W erreicht werden, wobei die emittierten Pulse eine Energie von jeweils 1.3 mJ und eine Spitzenleistung von 1.8 GW hatten. Die Systemeffizienz, welche ein Maß für die Qualität der Kombination ist, lag hierbei bei 93%. In der zweiten Konfiguration konnte durch Austausch der Fasern und Benutzung eines Streckers/Kompressors mit einer höheren Bandbreite eine Spitzenleistung von 22 GW erreicht werden, was den bisher höchsten Werte für ein faserbasiertes Lasersystem darstellt. In weiteren Versuchen wurde die kohärente Kombination von klassischen Festkörperverstärkern gezeigt, sowie die Anwendung der Kombination für die nichtlineare Pulskompression. Schlußendlich ist es für die Zukunft entscheidend, wie die Anzahl der Verstärkerkanäle erhöht werden kann. Dazu wurde eine Faser mit 4 integrierten Verstärkerkanälen zusammen mit einem kompakten Element für die Strahlaufteilung und -kombination untersucht.



# Danksagung (Acknowledgement)

Zuerst möchte ich Herrn Prof. Tünnermann und Herrn Prof. Limpert danken, die mir ermöglicht haben in den letzten Jahren am Institut für Angewandte Physik in einem exzellenten Umfeld zu forschen und diese Arbeit zu erstellen. Zusätzlich gilt mein Dank dem Helmholtz-Institut Jena für die Unterstützung meiner Arbeit. Daneben danke ich allen Kollegen, die mich sowohl bei den theoretischen Aufgaben als auch bei den Experimenten unterstützt haben und mit denen ich auch Abseits der Physik viel Spaß hatte. Hier sind an erster Stelle die Kombiniierer Marco Kienel, Tino Eidam, Michael Müller und Michal Wojdyr zu nennen. Nicht zu vergessen sind alle weiteren Kollegen, mit denen ich in den letzten Jahren zusammenarbeiten durfte: Cesar Jauregui, Sven Breitkopf, Steffen Hädrich, Stefan Demmler, Hans-Jürgen Otto, Fabian Stutzki, Florian Jansen, Thomas Gottschall, Jan Rothhardt, Reinhold Lehneis, Manuel Krebs, Alexander Steinmetz, Christian Gaida, Martin Baumgartl, Martin Gebhardt, Armin Hoffmann, Christoph Jocher, Evgeny Shestaev, Stefano Wunderlich, Simone Eidam, Getnet Tadesse, Maxim Tschernajew, Robert Klas und natürlich diejenigen, die ich hier vergessen habe zu erwähnen.

Schlußendlich gilt mein Dank meinen Eltern und Geschwistern, die mich über den gesamten Zeitraum meiner Arbeit unterstützt haben.

# Ehrenwörtliche Erklärung

Ich erkläre hiermit ehrenwörtlich, dass ich die vorliegende Arbeit selbständig, ohne unzulässige Hilfe Dritter und ohne Benutzung anderer als der angegebenen Hilfsmittel und Literatur angefertigt habe. Die aus anderen Quellen direkt oder indirekt übernommenen Daten und Konzepte sind unter Angabe der Quelle gekennzeichnet.

Bei der Auswahl und Auswertung folgenden Materials haben mir die nachstehend aufgeführten Personen in der jeweils beschriebenen Weise unentgeltlich geholfen:

- Die Koautoren der entsprechenden Publikationen bei den durchgeführten Experimenten.

Weitere Personen waren an der inhaltlich-materiellen Erstellung der vorliegenden Arbeit nicht beteiligt. Insbesondere habe ich hierfür nicht die entgeltliche Hilfe von Vermittlungs- bzw. Beratungsdiensten (Promotionsberater oder andere Personen) in Anspruch genommen. Niemand hat von mir unmittelbar oder mittelbar geldwerte Leistungen für Arbeiten erhalten, die im Zusammenhang mit dem Inhalt der vorgelegten Dissertation stehen.

Die Arbeit wurde bisher weder im In- noch im Ausland in gleicher oder ähnlicher Form einer anderen Prüfungsbehörde vorgelegt.

Die geltende Promotionsordnung der Physikalisch-Astronomischen Fakultät ist mir bekannt.

Ich versichere ehrenwörtlich, dass ich nach bestem Wissen die reine Wahrheit gesagt und nichts verschwiegen habe.

Jena, den

Arno Klenke